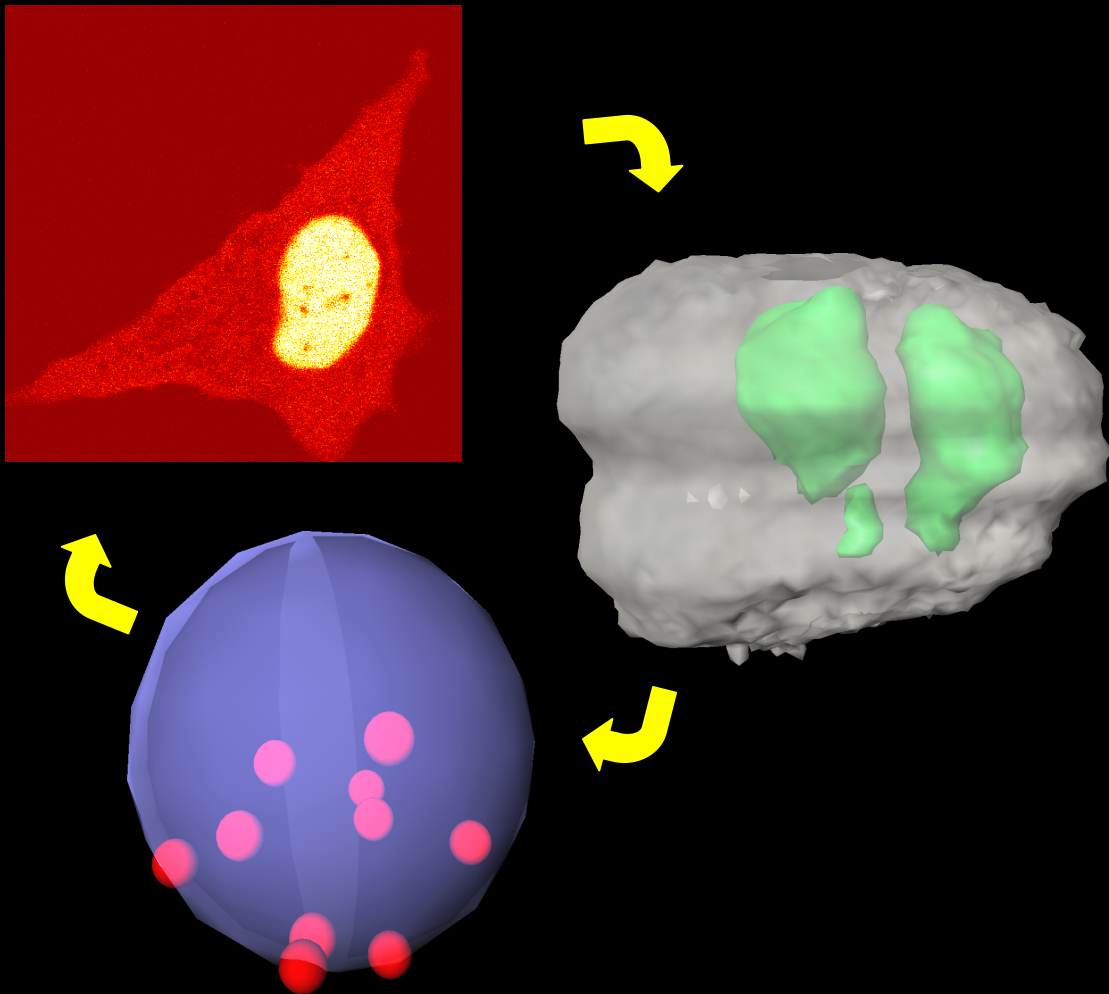


*Modelling Nuclear Body Dynamics  
in Living Cells by  
4-D Microscopy, Image Analysis and  
Simulation*



*Dissertation submitted to  
the Combined Faculties for the Natural Sciences and for Mathematics of  
the Ruperto-Carola University of Heidelberg, Germany  
for the degree of Doctor of Natural Sciences  
by Chaitanya A. Athale*

Dissertation  
submitted to the  
Combined Faculties for the Natural Sciences and for Mathematics  
of the Ruperto-Carola University of Heidelberg, Germany  
for the degree of  
Doctor of Natural Sciences

presented by

M.Sc. Zoology: Chaitanya A. Athale  
born in: Pune, India

Oral Examination:

2003



# **Modelling Nuclear Body Dynamics in Living Cells**

by

4-D Microscopy, Image Analysis and  
Simulation

Referees: Prof. Dr. Werner Herth

P.D. Dr. Harald Herrmann-Lerdon

---

# Publications

Major Parts of this work were published or are in preparation as manuscripts. These papers are as follows:

1. Chaitanya Athale, Morten Christensen, Roland Eils, Fritz Boege, Christian Mielke (2003) Predicting Sub nuclear Distribution Dynamics of Topoisomerase II beta by Kinetic modelling. (manuscript in preparation)
2. Chaitanya Athale, Michaela Reichenzeller, Peter Lichter, Harald Herrmann, Roland Eils (2003) Principles of Mobility of Nuclear Bodies in the Interchromosomal Domain revealed by Nuclear Targeted Vimentin. *Experimental Cell Research* (submitted)
3. Dietmar Volz, Martin Eigel, Chaitanya Athale, Peter Bastian, Harald Herrmann and Roland Eils (2003) Spatial Modeling and Simulation of Diffusion in Nuclei of Living Cells. *Biocomplexity* (submitted).
4. Roland Eils and Chaitanya Athale (2003). Computational Imaging in Cell Biology. *J Cell Biol.* 161(3)
5. Chaitanya Athale, Matthias Gebhard and Roland Eils (2002) Examining Spatio-Temporal Dynamics in Cell Nuclei by Image Processing Methods. In *Science, Technology and Education of Microscopy: An Overview*, vol. I (ed. A. Mendez-Vilas): FORMATEX Microscopy Book Series. (in press)
6. Chaitanya Athale (2002) Software for cell simulation. *Genome Biology* 3, reports2011.
7. Chaitanya Athale (2001) Cell-simulations portal. *Genome Biology* 3, reports2002.
8. Chaitanya Athale (2001) Monte Carlo cell simulations. *Genome Biology* 3, reports2001.

---

# Acknowledgments

I would like to thank Roland Eils for giving me the chance to work on a multi-disciplinary project, providing for an atmosphere of freedom in the iBioS lab and opportunities to interact with international experts from theoretical and experimental fields.

The experimental facilities and know-how in the labs of Harald Herrmann and Peter Lichter have made the difficult task of combining both experimental and theoretical methods easy. I would also like to acknowledge the numerous discussions with Harald Herrmann and his supervision of this work. My thanks go also to Michaela Reichenzeller for the vimentin project, Edeltraud Noffz for a rapid introduction to cell culture, Karsten Richter for patiently satisfying my curiosity about microscopy and Sabine Goerisch for help with live cell microscopy.

I would also like to thank Werner Herth for so warmly accepting the responsibility as my PhD supervisor (“Erstgutachter”).

For a productive collaboration on Topoisomerase I would like to thank Christian Mielke and Morten Christensen who did all the experiments, and were happy to try out some of my ideas.

For help with programming, timely tips on MATLAB and great discussions and fun times in lab and outside, I would like to thank Matthias Gebhard. I acknowledge Daniel Gerlich’s invaluable help with data visualization and for discussions, as well as the cooperation of Christian Conrad in image processing. I would like to acknowledge a productive collaboration with Dietmar Volz and Martin Eigel on the project on spatially resolved diffusion, especially useful discussions on diffusion with Martin. Also I would like to acknowledge the stimulating discussions with Sundararajan and Werner Dubitzky on modelling and for the latter’s help in filling in some of my cultural gaps.

I would also like to acknowledge Jan Ellenberg and his lab for the opportunity to interact with Robert Phair regarding compartmental modelling and Thorsten Klee on spatial diffusion. In particular I would like to acknowledge Thorsten’s help in setting up a spatial diffusion model. For useful comments on the Monte Carlo simulation, I would like to thank David Spector.

I am immensely grateful to Anupam Saraph for fascinating me with all things theoretical biology and the philosophy of science, an interest that has only increased with time.

A big thank you to my friends, all too many to mention, in Heidelberg, Pune and otherwise, especially Durba Sengupta and Luis Garcias-Alles. Without the persistent encouragement and attention of my family, particularly my parents Anil

---

Athale and Gouri Agtey-Athale, sister Ira Athale and uncle Ravindra Athale, none of this would have been possible.

# Contents

<b>1</b>	<b>Abstract</b>	<b>8</b>
<b>2</b>	<b>Introduction</b>	<b>10</b>
2.1	Models for Nuclear Organization during Interphase . . . . .	12
2.1.1	Organization of Chromosomes . . . . .	12
2.1.2	The Interchromatin Space . . . . .	15
2.2	Mobility in the Nucleus . . . . .	17
2.2.1	Chromatin . . . . .	17
2.2.2	Nuclear Bodies . . . . .	17
2.2.3	Nuclear Proteins, RNAs and other small complexes . . . . .	17
2.3	Interchromosomal Mobility of Molecular Probes . . . . .	19
2.3.1	Dextrans . . . . .	19
2.3.2	Nuclear Vimentin . . . . .	19
2.3.3	DNA Topoisomerase . . . . .	20
2.4	Confocal Laser Scanning Microscopy (CLSM) of Live Cells . . . . .	21
2.4.1	Fluorescence . . . . .	22
2.4.2	Confocal Imaging Principle . . . . .	22
2.4.3	Typical Confocal Microscope Setup . . . . .	24
2.5	Green Fluorescent Protein (GFP) . . . . .	25
2.5.1	GFP Structure . . . . .	25
2.5.2	XFP Variants . . . . .	26
2.5.3	Photoinduced Fluorophore Bleaching . . . . .	26
2.5.4	Applications . . . . .	27
2.6	Computational Image Analysis and Quantification . . . . .	27
2.6.1	Filtering and Preprocessing . . . . .	28
2.6.2	Segmentation . . . . .	29
2.6.3	Single Particle Tracking . . . . .	29
2.6.4	Optical Flow . . . . .	29
2.6.5	Registration . . . . .	29
2.6.6	Visualization . . . . .	30



2.6.7	Signal Concentration Estimation . . . . .	31
2.6.8	Quantitative Photobleaching Experiments . . . . .	31
2.7	Modelling Diffusion in Cell Biology . . . . .	38
2.7.1	Molecular Diffusion . . . . .	38
2.7.2	Anomalous Diffusion . . . . .	39
2.7.3	Molecular Binding . . . . .	40
2.7.4	Compartment Models . . . . .	41
2.7.5	Spatial Diffusion with Partial Differential Equations (PDE) .	42
2.7.6	Monte Carlo Simulations . . . . .	43
2.8	Aim of the work . . . . .	44
<b>3</b>	<b>Materials and Methods</b>	<b>45</b>
3.1	Cell Culture . . . . .	46
3.1.1	Cell Types . . . . .	46
3.1.2	Passaging of Cells in Culture . . . . .	46
3.1.3	Transient Transfection of Cells . . . . .	47
3.1.4	DNA . . . . .	47
3.1.5	Methanol Acetone Fixation of Cells . . . . .	48
3.2	Live Cell Microscopy . . . . .	48
3.2.1	Culturing Cells under the Microscope . . . . .	48
3.2.2	ATP Depletion with Na-Azide . . . . .	49
3.3	Confocal Laser Scanning Microscopy . . . . .	49
3.3.1	FRAP . . . . .	51
3.4	Image Processing of Microscopy Data . . . . .	53
3.4.1	Filtering of Images . . . . .	53
3.4.2	Segmentation of Images . . . . .	53
3.4.3	Intensity and Volume Estimation . . . . .	53
3.4.4	3-D and 4-D Visualization . . . . .	54
3.4.5	Single Particle Tracking . . . . .	54
3.5	Monte Carlo Simulation of Particle Diffusion . . . . .	55
3.6	Discrete Diffusion Analysis of Particles . . . . .	55
3.6.1	Velocity . . . . .	55
3.6.2	Mean Square Displacement . . . . .	56
3.6.3	Effective Diffusion . . . . .	57
3.6.4	Anomalous Diffusion . . . . .	58
3.6.5	Statistical Testing of Models . . . . .	59
3.7	Coupled ODE Simulation of Subnuclear Distribution . . . . .	59
3.8	PDE based Continuum Diffusion Simulation . . . . .	60
<b>4</b>	<b>Results</b>	<b>61</b>

4.1	Mobility of VNBs . . . . .	62
4.1.1	VNBs show Unimodal Velocity and Size Distribution . . . .	62
4.1.2	Dynamics of VNBs corresponds to a passive motion model .	64
4.1.3	Effective Viscosity and Diffusion Models . . . . .	64
4.1.4	Rejecting the Critical Diffusion Model . . . . .	66
4.1.5	Anomalous Diffusion of VNBs . . . . .	67
4.1.6	Fusion of Bodies is an Additive Process . . . . .	67
4.2	Monte Carlo Simulation of the Interphase ICD space . . . . .	73
4.2.1	Effect of Channel Obstacles . . . . .	74
4.3	Effect of Chromatin Density on Diffusion of NLS-YFP in the Nucleus	75
4.3.1	FRAP Analysis . . . . .	75
4.3.2	Non-Ideal Recovery . . . . .	77
4.3.3	Simulation of FRAP in 2-D . . . . .	79
4.4	Dynamics of Topoisomerase Localization . . . . .	83
4.4.1	3-D Visualization of TopoIIb Distribution . . . . .	83
4.4.2	Model of TopoIIb Distribution . . . . .	84
4.4.3	Testing the TopoIIb Model . . . . .	87
<b>5</b>	<b>Discussion</b>	<b>89</b>
5.1	Mobility of vimentin nuclear bodies (VNBs) . . . . .	90
5.1.1	ATP Independence of VNB Mobility . . . . .	90
5.1.2	Rejecting the Compaction Model of VNB Fusion . . . . .	90
5.1.3	Size, Velocity and Diffusion Constant . . . . .	91
5.1.4	High Effective Nuclear Viscosity . . . . .	92
5.1.5	Possible Sieving Mechanism of the Nuclear Medium . . . .	92
5.1.6	Anomalous Diffusion in the ICD . . . . .	93
5.2	Simulated Obstacles to Intra-Nuclear Diffusion . . . . .	94
5.3	Spatial Variations in Intra-Nuclear Diffusion . . . . .	94
5.3.1	Analysis of Experimental Data . . . . .	95
5.3.2	Fitting a Diffusion Tensor . . . . .	95
5.3.3	2-D Simulation . . . . .	95
5.4	Topoisomerase Distribution between Nucleus and Nucleoplasm . . .	96
5.4.1	Validation of the Model . . . . .	96
<b>6</b>	<b>Conclusions and Outlook</b>	<b>97</b>
6.1	Nuclear Body Diffusion and Integrity . . . . .	98
6.1.1	Anomalous Diffusion of Nuclear Bodies . . . . .	98
6.1.2	Fusion does not Change VNB Density . . . . .	99
6.1.3	Rules of Nuclear Body Size and Mobility . . . . .	99
6.2	Simulating Nuclear Body Motion and Stability . . . . .	101

---

6.2.1	ICD Channels do not affect VNB Motion . . . . .	101
6.2.2	Formation and Stability . . . . .	101
6.2.3	Energy Dependent Mobility . . . . .	102
6.2.4	Mechanisms of Regulated Mobility . . . . .	102
6.3	Spatial Influences on Nuclear Protein Diffusion . . . . .	102
6.3.1	Chromatin Effects on YFP Mobility . . . . .	103
6.3.2	Spatial Simulations for Discovering Novel Genomic Sites .	103
6.4	Self-Organizing Model of Nuclear Structure- e.g. Topoisomerase .	104
6.4.1	Predictive Model of TopoisomeraseII $\beta$ Distribution . . . . .	104
6.4.2	Evidence for Self-Organization in Nuclear Organization . .	104
6.5	Outlook . . . . .	104
<b>7</b>	<b>Abbreviations</b>	<b>107</b>
	<b>Appendices</b>	<b>109</b>
<b>A</b>	<b>Flow Diagram of Monte Carlo Simulation Program</b>	<b>109</b>
<b>B</b>	<b>Text of the Reports published in Genome Biology</b>	<b>110</b>
B.1	Cell-simulations portal . . . . .	111
B.2	Monte Carlo cell simulations . . . . .	114
B.3	Software for cell simulation . . . . .	117
	<b>References</b>	<b>123</b>

# Chapter 1

## Abstract

The work presented here demonstrates rules of and validates models for nuclear body (NB) dynamics. Simulation tools developed in the course of this work, can be used in future work to generate hypotheses about related aspects of nuclear architecture.

Initially I examined the mobility of vimentin nuclear bodies (VNB) in interphase by single particle tracking and analysis of fluorescence images from 4-D confocal laser scanning microscopy (CLSM). These synthetic nuclear bodies are observed in cells transfected with labelled nuclear targeted *Xenopus laevis* vimentin. Analysis shows that VNBs undergo anomalous diffusion in the nuclei, independent of metabolic energy. Individual bodies display either one of the three modes of diffusion -directed, restricted or simple. The consistency of modes and magnitudes of diffusion constants between VNBs and *bona fide* nuclear bodies points to a generic mechanism that mediates and regulates the mobility of nuclear bodies.

Since the results of diffusion analysis of VNBs did not agree with a simple diffusion model, I tested the alternative interchromosomal domain (ICD) compartment model. The ICD model predicts that in interphase cell nuclei, individual decompacted chromosomes do not intermingle, but are separated by a significant interchromatin space forming a network of channels. These networks could affect the mobility of nuclear bodies. Monte Carlo simulations that predict the effects of channels and other obstructions on NB diffusion were tested, but they could not explain deviation from ideal behaviour. Fitting an empirical model of ‘critical diffusion’ produced similar results. Therefore the ICD model as a purely obstructing network of channels needs modification, to possibly include binding.

To examine the role of chromatin density in intra-nuclear diffusion, I employed multidimensional fluorescence recovery after photobleaching (FRAP) in living cells. The influence of chromatin density on diffusive mobility of the nuclear yellow fluorescent protein (YFP) appears marginal. A 2-D diffusion simulation to better characterize the experiment, provides a tool to produce ‘diffusion maps’ of the nucleus.

The related aspect of nuclear body integrity and dynamics was examined for the distribution of topoisomerase II beta (TopoIIb), which localizes preferentially in the nucleolus. The experimentally observed diffusion and binding dynamics were formulated as a compartment model and fitted to the experiments. The model topology, flux constants and residence times estimates could be validated, providing a predictive model of TopoIIb dynamics

By demonstrating that VNB diffusion is anomalous and consistent with other *bona fide* NBs, I have revealed a mechanism that regulates NB mobility. The diffusion of these bodies deviates however from ideal diffusion, and can be explained by neither the effect of chromatin density on molecular diffusion, nor the different models of NB diffusion. I have shown that binding rather than diffusion appears to determine nuclear body localization and dynamics, as in the case of TopoIIb. Nuclear bodies and nuclear architecture has been recently hypothesized as emerging from simple local interactions. The predictive model for TopoIIb distribution dynamics provides evidence for this. The models presented here, are in keeping with the increasing trend to abstract nuclear dynamics as mathematical models. It is hoped that the work presented here will contribute to the effort of arriving at an integrated model for nuclear bodies and therefore better understanding nuclear architecture.

## Chapter 2

### Introduction

“Slipping off behind was the bulge of the nucleus of the cell, large and thick and growing larger and thicker.”

-Isaac Asimov in *Fantastic Voyage II - Destination Brain*

The aim of this work was to develop and test models for the mobility of nuclear bodies and nuclear proteins in interphase cells. For this I used confocal laser scanning microscopy (CLSM) of fluorescently labelled cells, computational image analysis, mathematical modelling and simulation.

Cell nuclei were discovered by light microscopy around 1755 (1), soon after the initial observations of dead cork cells by Robert Hooke. As the compartment which holds the genomic DNA of the cell, it has drawn increasing attention of investigators. The transformation experiment by Griffiths (1928) showed DNA to be the hereditary material in cells. The solution of its structure by Watson and Crick in 1953 and most recently the first draft of the sequence of the human genome (2, 3) have only added to making DNA in particular and the cell nucleus in general both interesting and accessible to biologists.

One of the issues of interest in the nucleus is the 3-D organization of the genome. The haploid human genome contains about  $3 \times 10^9$  nucleotide pairs, organized as 23 pairs of chromosomes, and thus consists of 46 DNA molecules - each containing from  $50 \times 10^6$  to  $250 \times 10^6$  nucleotide pairs of DNA (4). DNA molecules of this size are 1.7 to 8.5 cm long when uncoiled, and even the slightest mechanical force will break them once the chromosomal proteins have been removed. *In vivo* it is found complexed with proteins and folded in a hierarchical manner forming chromatin. The exact nature of “higher order” structure – beyond the canonical “30-nm” fibre – remains only partially characterized (5).

In dividing cells chromosomes are condensed and have a clearly defined boundary with mitotic chromosomes aligned in a Rabl orientation (6, 4), where the centromeres and telomeres located at opposite poles of the nucleus. Interphase chromosomes, might also carry on with some of the order, and this was shown to possess some form of organization in Chinese hamster cells (7, 6). One model has been put forward, that active genes are located on loops that may be mobile within the nucleus (8). Based on the model that interphase chromosomes are organized into chromosome territories (CT), chromatin gets divided into more accessible chromatin at the surface and less accessible chromatin at the interior of the territory. This differential access depends on the size of the diffusing complex and is thought to be relevant for structures like the RNA polymerase (radius in water = 35 nm (9). The functional, reactive and ordered accessible inter chromosomal space, the inter chromosomal domain (ICD) compartment was proposed based on 3-D fluorescence microscopy of surfaces of CTs found to harbor sites of splicing and transcription (10). Diffusion studies of RNA (11) and microinjected dextrans (12) however indicate that mobility is free in every direction within the nucleus. This has led to the formulation of the alternative model of nuclear organization that does not need an ICD space and for purposes of diffusion is homogeneous.

Mathematical modelling combined with live cell imaging and analysis to explicitly test the alternative models in nuclei has not been attempted. Two possible models that can be formulated in terms of transport kinetics are of an inhomogeneous nucleus or a homogeneous “well mixed” nucleus. Already in the 1800’s it had become clear that nuclei were inhomogeneous when by the early 20<sup>th</sup> century the nucleolus and heterochromatin were discovered and later the nucleolus was accepted as the site of ribosomal RNA synthesis (13). Mathematical modelling approaches have been employed to investigate the role of obstructions in the endoplasmic reticulum and mitochondria using Monte Carlo modelling (14). Another recently applied approach of modelling involved compartment analysis and modelling to examine the appropriate kinetic model of secretory protein traffic in Golgi transport (15). The diffusion of calcium in muscle cells (16) and oocytes (17) has also been simulated considering spatial aspects.

The related question of the stability of sub-nuclear structures also remains under debate. Topoisomerase molecules for instance are a prime example, since they have a dynamic function of unwinding supercoils in genomic DNA and are found bound to chromatin (18). Of these, topoisomerase II (TopoII) accumulates preferentially in the nucleolus – where ribosomal genes are transcribed (reviewed for instance in 19). Understanding the integrity and dynamics of such preferential localization will provide clues about principles governing the organization of nuclear bodies, and by extension the intra chromosomal space and the nucleus itself.

## 2.1 Models for Nuclear Organization during Interphase

The interphase nucleus with de-condensed chromosomes, can be broadly seen as having two clear sub-regions – chromatin and the interchromatin space (20). Both regions have been shown to have varying degrees of organization. The details of this organization are as follows.

### 2.1.1 Organization of Chromosomes

Eukaryotic nuclei contain the genomic DNA of the cell, organized in chromosomes. The double stranded DNA (3.38 Å per bp rise) is organized hierarchically, with the nucleosomes being the smallest organizing unit (Figure 2.1).

Nucleosomes form a cylinder of 11 nm diameter and 6 nm high, and consist of 2 turns of 146 bps DNA around 8 histones (*‘core histones’*), with 54 bps overhanging. These histones are further organized into a continuous string, with a diameter of 10 nm and hence called the *‘10 nm fiber’*, seen sometimes as *‘beads on a string’*. The



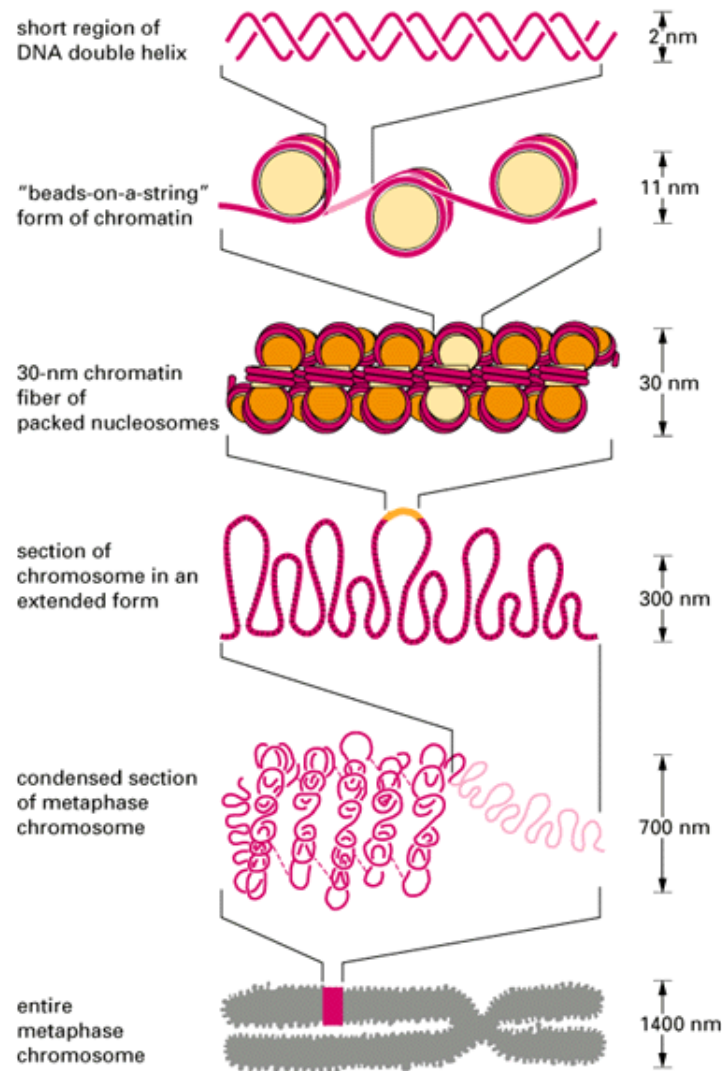


Figure 2.1: The hierarchical organization of chromatin is illustrated in this figure, starting with the DNA strand, through to the nucleosomes ("beads on a string" chromatin), 30 nm chromatin fibre, a looped form of chromatin, a condensed form of chromatin and the metaphase chromosome (from 4).

10 nm fiber is wound solenoid-like into coils of  $\sim 6$  nucleosomes for every turn and 40  $\mu\text{m}$  DNA for every 1  $\mu\text{m}$  of the fiber- '30 nm fiber', held together by the Histone H1. This fiber is the basic constituent of interphase and mitotic chromosomes (Figure 2.1).

The stages of mitosis show an extreme degree of chromosome order (e.g. the metaphase plate organization of the chromosomes), which is not so obvious in interphase nuclei. Already at the the turn of the 19<sup>th</sup> century, Carl Rabl (1895) and Theodori Boveri (1909) postulated a separation of chromosomes into distinct terri-

tories in the interphase, from studies involving light microscopy. Since then, different, sometimes mutually exclusive models of organization of chromatin have been proposed. Some of the important ones in the context of the interchromatin space are as follows.

1. Nuclear Matrix or Scaffold: The extraction of a nuclease-resistant fraction as a nuclear matrix has held out hope for a nuclear equivalent for the cytoskeleton with fibres stretching from the nuclear pores, criss-crossing in the interior of the nucleus. These substructures – nuclear matrices, nucleoids and nuclear scaffolds – are different from one another and studies on them have led to different views of how chromatin is organized (21).
2. Random Distribution of Chromosomes: An alternative view is that no particular order exists in interphase chromosome organization. Centromeres and telomeres can be found distributed throughout the nucleus (22, 23) with some preference for peripheral and perinucleolar positions (23).
3. Size-Based Chromosome Positioning: Other studies led to the concept that a size based purely physical sorting of entire chromosomes, the larger outside, the smaller inside. Some of this has experimental evidence in support, but it appears to depend also on the cell type (24, 25, 26).
4. Differential Packaging of Chromatin: Evidence generally suggests that transcribed chromatin is more sensitive to DNaseI digestion than untranscribed chromatin, indicating differences in accessibility of chromatin (27). This suggests that chromatin is packed differently, depending on whether it is active or not and alludes to an *in vivo* mechanism of gene expression.
5. Replication Timing Dependent Chromatin Positioning: Linking gene expression status with position, independent of the specific chromosome, the model assumes that irrespective of the chromosomes, euchromatin with actively expressed genes is peripheral to the nucleus and heterochromatin with inactive genes toward the center (28, 29).
6. Chromosome Territories: A model that includes aspects of the last two models proposed that the chromosomes were organized in chromosome territories (CT's). According to this model, interphase nuclei are organized with chromosomes restricted to defined territories, as has been shown with fluorescence in situ hybridization (FISH) techniques (30, 31) and replication labeling (32, 33).

There are varying degrees of evidence for each of these models and the issue has not yet been settled, especially if variations between cell types are taken into

account.

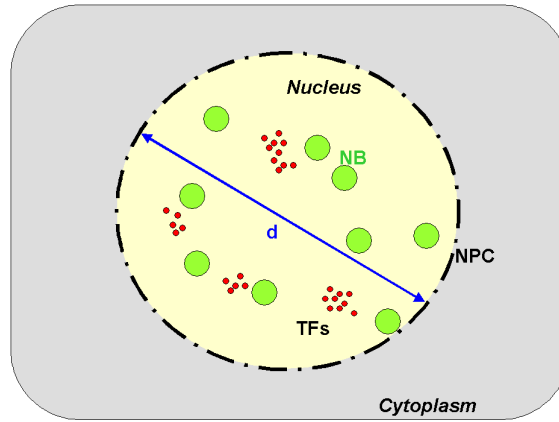


Figure 2.2: A hypothetical generic cell with cytoplasm and inner nucleus surrounded by a nuclear membrane with pores- the nuclear pore complex (NPC). Besides the chromatin, nuclear bodies (NB) and transcription factor (TF) assemblies can be found. The typical diameter ( $d$ ) of a mammalian nucleus = 5-15  $\mu\text{m}$ .

Table 2.1: The time taken for typical molecules of interest to traverse a theoretical circular 2-D mammalian cell nucleus (Figure 2.2) based on the root mean square velocity of diffusion in cells.

<b>Nuclear diameter (<math>d</math>)</b>	10 $\mu\text{m}$
<b>Transcription Factor (TF) diffusion constant (<math>D</math>)</b>	$\approx 0.3\mu\text{m}^2/\text{s}$
<b>Time to Traverse entire nucleus</b>	$\approx 3\text{s}$

### 2.1.2 The Interchromatin Space

An important and related question to the distribution of chromatin in the nucleus is the arrangement of the space between chromosomes and their territories. Related to the model of chromatin organization, the various models describing this space can be classed as follows:

1. Homogeneous Nucleus: According to this model, based on experimental evidence from Diffusion studies with dextrans (12) and labelled uncaged single

RNA molecules (20, the space of the nucleus can be treated as a homogeneous mixture. This implies that the interchromatin space and the chromosome territories, offer the same amount of hindrance to the movement of these molecules.

2. Interchromosomal domain (ICD) compartment: Based on the model of organization of chromatin into chromosome territories (CT) (34), which are assumed to provide hindrance to the mobility of proteins and RNA, the space between the territories is relatively free, with a brush border of looped DNA and RNA that is free or being transcribed at the chromosome territory surface. This ‘domain’ might be conducive for transport between the CTs as well as CTs and the nuclear pores (30, 31, 35). By 3-D fluorescence microscopy, surfaces of chromosome territories were found to harbor sites of splicing and transcription (10), confirmed further by recent studies with FISH of genes in a gene-rich context (36). This has led to the concept that the interchromatin space is functional, reactive and ordered and referred to as the inter chromosomal domain (ICD) compartment (31, 30, 10). The ICD compartment was also observed by immunofluorescence microscopy of the *Drosophila* Tpr (translocated promoter region) homologue (37). The ectopic expression of an NLS-tagged *Xenopus laevis* vimentin was used to mark a clear chromatin excluding ICD in mammalian cells (38). The molecular basis for such a space was alluded to by the description of a regulated, expandable, extra-chromosomal nuclear domain (END) occupied by the EAST protein (enhanced adult sensory threshold) in *Drosophila* nuclei (39).

Neither model has been categorically rejected, and it remains to be seen which model might better describe the organization of the interchromatin space. Work on quantifying the size, shape and dynamics within the nucleus has revealed a quantitative picture, summarized in Figure 2.2 and Table 2.1. Based on work in cells a general framework of discrete and continuous approaches has been developed dealing with transport and diffusion in cells (reviewed in 40).

## 2.2 Mobility in the Nucleus

The mobility of molecules and structures in the nucleus is important since the cornerstones of arguments for the various models of organization the inter chromatin space is the facilitation of transport and mobility. The various structures that have been examined for their mobility are chromatin, nuclear bodies and uncomplexed single molecules.

### 2.2.1 Chromatin

Studies in which the movement of labelled and bleached heterochromatic and euchromatic regions was followed in interphase nuclei of Swiss 3T3 and HeLa, led to the conclusion that interphase chromatin is immobile over distance scales  $\geq 0.4 \mu\text{m}$  (41). However a study done with a GFP-topoisomerase II fusion approach in *Drosophila* with micrometer scale tracking in 3-D found that chromatin undergoes substantial Brownian motion. This movement is confined to a subregion of the nucleus for a segment of chromatin. A highly defined nuclear architecture with enough freedom of motion for processes requiring chromosome motility (42).

### 2.2.2 Nuclear Bodies

It has been only gradually that the space between chromosomes has been recognized through ultrastructural studies as being occupied by various structures (43). These include small nucleolar ribonuclear proteins (RNP) that display a reticular network of distribution (44), nuclear bodies like the Inter Chromatin Granule Compartment (IGC) or speckles, Cajal Bodies and promyelocytic leukemia (PML) bodies (45).

### 2.2.3 Nuclear Proteins, RNAs and other small complexes

For small molecules tracked poly(A) RNA (20) and photobleaching recovery measurements of labelled dextrans of up to 500 kD size (12) as well as transcription factors (46) showed that most parts of the nucleus were accessible to the molecules. Topoisomerases, especially the well studied topoisomerase II has been shown in early work to be a major polypeptide component of chicken mitotic chromosome scaffolds by indirect immunofluorescence and subcellular fractionation experiments in both mitotic chromosomes and interphase nuclei (47, 48). Other work has confirmed that TopoII plays a role in chromosome condensation at mitosis and is located at the core of the chromosomal axis (18). Topo II studied *in vivo* by recording time-lapse, three-dimensional data sets of living *Drosophila melanogaster* embryos injected with Rhodamine-labelled Topo II showed that it is concentrated at specific

localization sites within the interphase nucleus. It was also shown that localization is temporally regulated. During mitosis, the enzyme present in the early prophase chromosome is lost in two stages, following prophase and following anaphase. Overall, 70% of the enzyme leaves the nucleus and diffuses into the cytoplasm. The localization of the enzyme thus correlates with its role in chromosome condensation and segregation. All this would seem to indicate that this protein, formerly regarded as a stable component of the nuclear scaffold might have a more dynamic role (49).

Table 2.2: *Relative sizes of sub-nuclear structures has been measured in the past and this table summarizes some of the values, in order to give an idea of the scales involved.*

Structure	Size Parameter	Extent	Reference
Typical mammalian cell nucleus	Diameter	$\sim 10 \mu m$	4, 50
Chromosome territory	Diameter	400-800 nm	51
Perichromatin Fibrils	Diameter	3-5 nm	52, 50
"	Length	20 nm	"
IGC	Diameter	20 nm	"
"	Length of connecting fibril	3-8 nm	"
Nuclear Dots (ND10) or PML bodies	Diameter	$0.5 \mu m$	45
Cajal bodies (CB)	Diameter	1-10 $\mu m$	53

The challenge is to encapsulate the dynamics and structure of the nucleus and its sub-compartments in models that are quantitative and predictive.

## 2.3 Interchromosomal Mobility of Molecular Probes

The physical structure of cellular compartments and specifically the cytoplasm has been a topic of long-standing interest (for review see 54, 55, 56, 57). The physical approach to the medium as well as the molecular probes, have also begun to be employed in studying the nucleus and its organization. The work done in the past has used different molecular probes to do this. They include both artificial ones like fluorescently labelled dextrans and vimentin, as well as proteins like topoisomerases and RNAs. Some of these approaches are briefly discussed here.

### 2.3.1 Dextrans

The mobility based on size in compartments of cells has been studied using many different probes but the ease of control over size, labeling with fluorescent tags and inert nature in cells has made dextrans a popular tool in mobility measurements. In the nucleus, the mobility of fluorescein isothio-cynate (FITC) labelled dextrans was measured by microphotolysis or fluorescence recovery after photobleaching (FRAP). Cytoplasmic and nucleoplasmic viscosities were derived to be 6.6 and 8.1 cP respectively at 23°, by fitting the Stokes-Einstein relation (58). Further studies have shown that dextrans of up to 580 kD were still mobile inside the cell nuclei. The ‘*fluid-phase*’ viscosity of cytoplasm and nucleus, defined as the viscosity sensed by a small probe that does not interact with cellular components, was determined by time-resolved anisotropy and ratio imaging of a viscosity-sensitive fluorescent probe to be only 1.2-1.4 times greater than the viscosity of water (59). This work has helped clarify the issue of the physical nature of cytoplasmic and nuclear organization. However, the question of the nature of the obstructions that give rise to ‘effective viscosity’, especially when the particle sizes exceed a threshold still remain unanswered.

### 2.3.2 Nuclear Vimentin

Vimentin is a type III intermediate filament protein that strictly localizes in interphase to the cytoplasm, where it forms filamentous arrays. The temperature-sensitive *Xenopus* vimentin formed filaments on shifting cells from 37°C to 28°C, which were ectopically expressing the cDNA. When cDNA tagged with the nuclear localization signal (NLS) was expressed, these filaments were seen in the nucleus (38). Co-transfecting the NLS-vimentin and the GFP-labelled construct at 37°C leads to the accumulation of 10-20 evenly spaced structures termed vimentin nuclear bodies (VNB). At 28°C IFs appear to assemble starting from the VNBs eventually connecting neighbouring bodies. The polymerized structures lay extra-



chromosomally, as seen by chromosomal fluorescent in situ hybridization (FISH) labeling, co-existed with nuclear RNAs, Cajal bodies (CB) and PML bodies, and appeared to mark a reticulate inter chromosomal domain (ICD) compartment (38, 60). The data suggest that channel-like ICD spaces might exist in the nucleus and that the NLS-vimentin might be useful tool for better understanding this space.

### 2.3.3 DNA Topoisomerase

Topoisomerases are nuclear proteins that help a cell overcome the so-called ‘winding problem’ during DNA replication, in which the movement of a replication fork causes further winding of the entire chromosome ahead of the fork. To overcome the winding tension, the chromosome would have to rotate rapidly at the cost of large amounts of metabolic energy. The alternative used during DNA replication involves swiveling the DNA helix by proteins known as DNA topoisomerases (4). The mode of action of topoisomerases is to reversibly add itself covalently to a DNA phosphate, thereby breaking a phosphodiester bond in a DNA strand. Based on the detailed mechanism of cleavage, there are two kinds of topoisomerases:

1. Topoisomerase I causes a single-strand break (or nick), which can allow the two sections of DNA helix on either side of the nick to rotate freely relative to each other, using the tension in the DNA helix to drive this rotation in the direction that relieves the tension. As a result, DNA replication can occur with the rotation of only a short length of helix - the part just ahead of the fork. The analogous problem that arises during DNA transcription is solved in a similar way.
2. Topoisomerase II forms a covalent linkage to both strands of the DNA helix at the same time, making a transient double-strand break in the helix. These enzymes are activated by sites on chromosomes where two double helices cross over each other. When the topoisomerase binds to such a crossing site, it (1) breaks one double helix reversibly to create a DNA ‘gate’ (2) causes the second, nearby double helix to pass through this break, and (3) reseals the break and dissociates from the DNA. The same reaction prevents the severe DNA tangling problems that would otherwise arise during DNA replication.

DNA topoisomerase II was identified as the first major non-histone component of the chromosome scaffold (47, 61) and the interphase nuclear matrix (62). Both structures are assumed to play a major role in nuclear architecture. In contrast to this view, TopoII was shown later in *Xenopus* egg extracts to be easily washed off chromosome preparations and not integrated in the chromosome scaffold as previously assumed (63). In mammals, topoisomerase is expressed as two isoforms-



TopoII  $\alpha$  and  $\beta$ , which have similar primary structure and almost identical catalytic properties *in vitro* (64). TopoII  $\alpha$  localization has been shown to be mainly in the central axis of mitotic chromosomes. TopoII  $\beta$  has been shown in live microscopy studies to change its localization from a concentration in the nucleolus in interphase to the cytoplasm at the time of division (49). Thus, an integration of these varied findings, with fresh experiments in live cell microscopy studies, might hold promise for better understanding the localization of such a protein and eventually lead to a more integrated view of the molecular basis of inter chromosomal space.

## 2.4 Confocal Laser Scanning Microscopy (CLSM) of Live Cells

Dynamic processes are at the very basis of cellular function microscopy has had a crucial role in uncovering it in cells. Cellular structures have been studied in fixed and living specimens by various microscopic techniques including phase contrast, differential interference contrast (DIC) and confocal microscopy. In fluorescence microscopy, a cell is stained with a dye and the dye is illuminated with filtered light at the absorbing wavelength; the light emitted from the dye is viewed through a filter that allows only the emitted wavelength to be seen. The dye glows brightly against a dark background because only the emitted wavelength is allowed to reach the eyepieces or camera port of the microscope. Most microscopes are designed using epi-illumination. In epi-illumination excitation, light goes through the objective lens and illuminates the object. Light emitted from the specimen is collected by the same objective lens.

Fluorescence imaging today is performed overwhelmingly with digital imaging systems. The readily available systems are:

1. Laser scanning microscopes (LSM), which scan the sample point-by-point with a focused light from a laser source and detect emitted fluorescence with a photomultiplier tube (PMT).
2. Wide-field microscopes (WFM) illuminate the whole sample simultaneously and record the emitted fluorescence as an image with a charge-coupled device camera (CCD) (65).

In comparison, WFM requires collection of a full 3-D image and subsequent computer processing, but allows imaging weakly fluorescent structures. Scanning microscopy provides a single 2-D image with significantly reduced blur with only minimal processing (frame averaging, etc.), but low sensitivity to weakly fluores-

cent structures. (see 66 for a recent comparison). Which system is eventually chosen depends on the nature of the sample.

These microscopy methods are limited by their spatial resolving power (approximately  $0.25\text{ }\mu\text{m}$  in the image plane and  $0.5\text{ }\mu\text{m}$  along the optical axis) due to the diffraction limit of light. Attempts to break these limits include multifocal multiphoton (67), stimulated emission (68), 4Pi (69), standing wave excitation (70) and I5M/structured illumination (71).

### 2.4.1 Fluorescence

Fluorescence microscopy is used to detect structures, molecules or proteins within the cell. Fluorescent molecules absorb light at one wavelength and emit light at another, longer wavelength. When fluorescent molecules absorb a specific absorption wavelength for an electron in a given orbital, the electron rises to a higher energy level (the excited) state. Electrons in this state are unstable and will return to the ground state, releasing energy in the form of light and heat. This emission of energy is fluorescence. Because some energy is lost as heat, the emitted light contains less energy and therefore is a longer wavelength than the absorbed (or excitation) light.

Sometimes the fluorescent molecule itself is a direct stain or probe for specific structures. In other situations the fluorescent dye is bound to another non-fluorescent probe that recognizes specific structures. For example, the fluorescence molecule, Rhodamine may be conjugated to phalloidin, which binds the filamentous actin. One important method to identify specific proteins is to couple fluorescent dyes to antibodies that bind very specifically to macromolecules in the cell.

Fluorescent dyes such as fluorescein and Rhodamine (4) have been employed for long to tag and observe structures. The technique to introduce them into cells however mostly involves microinjection (72). The advent of recombinant fluorescent protein technology best symbolized by the Green Fluorescent Protein (GFP) (73). This has become easily the most powerful (due to its ease of usage) method in live cell fluorescence probe preparation and the tagging the protein of interest is done by recombinant DNA techniques.

### 2.4.2 Confocal Imaging Principle

The confocal microscope was invented by Marvin Minsky in 1955 for imaging neuron samples, but the concept was developed later and became widespread (74). The confocal principle can be explained as follows and is also represented in Figure 2.3. Assuming we are given a pair of lenses inside a microscope, that focus light from a sample (S) from the focal point of one lens to that of the other at point P. This is represented by the solid rays of light in the figure. The dotted rays of light represent

light from another point in the sample, which is not at the focal point of the lens, but which nonetheless get imaged by the lenses of the microscope (where the bold and dotted rays are at the same wavelength). The image of the point of origin of the bold rays is not at the same location as the image of the dotted rays.

Let us assume we want to just look at the bold point, that is, the point directly at the focus of the lens. If we put a screen with a pinhole at the other side of the lens system, at the image of the bold point, then all of the light from the original bold point will pass through this pinhole. However, most of the light from the dotted point is still out of focus at this screen, and gets blocked by the pinhole.

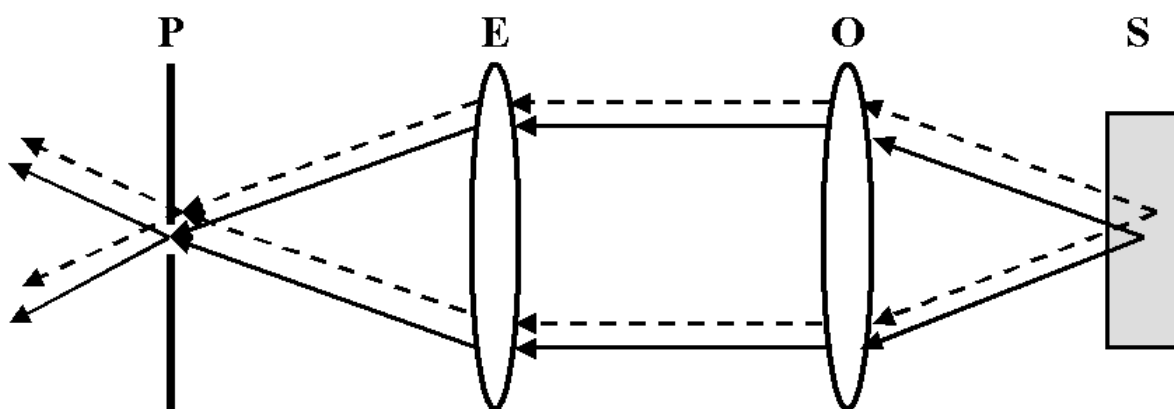


Figure 2.3: The principle of confocal microscopy is illustrated in the figure here. The two rays are rays from two different focal points and the two lenses being the objective (O) and eyepieces (E). The role of the pinhole (P) is to block out all light except that at the focal point (solid lines), and the extent of this is determined by the pinhole diameter. The dotted lines represent out of focus light (adapted from 75).

This solves one of the problems of regular fluorescence microscopy. Normally, the sample is completely illuminated by the excitation light, so all the tagged molecules

of the sample undergo fluorescence at the same time. Of course, the highest intensity of the excitation light is at the focal point of the lens, but nonetheless, the other parts of the sample do get some of this light and they do fluoresce. This contributes to a background haze in the resulting image. Adding a pinhole-screen combination solves this problem. Because the focal point of the objective lens of the microscope forms an image where the pinhole is, these two points are known as “conjugate points” (or alternatively, the sample plane and the pinhole-screen are conjugate planes). The pinhole is conjugate to the focal point of the lens, thus it is a confocal pinhole (75).

### 2.4.3 Typical Confocal Microscope Setup

A typical confocal microscope set-up is described in Figure 2.4. This particular style of fluorescence microscopy is known as epi-fluorescence, and uses the microscope objective to illuminate the sample (rather than illuminating the sample from the other side, which would be trans-fluorescence).

A laser is used to provide the excitation light (in order to get very high intensities). The laser light (blue) reflects off a dichroic mirror. From there, the laser hits two mirrors which are mounted on motors; these mirrors scan the laser across the sample. The dye in the sample fluoresces, and the emitted light (green) gets descanned by the same mirrors that are used to scan the excitation light (blue) from the laser. The emitted light passes through the dichroic and is focused onto the pinhole. The light that passes through the pinhole is measured by a detector, i.e. a photomultiplier tube.

The dichroic mirror (or “dichromatic mirror”) distinguishes between excitation and emission wavelengths. This mirror reflects light shorter than a certain wavelength, and passes light longer than that wavelength. Thus only the emitted light from the fluorescent dye is detected, rather than seeing scattered light (used for excitation) (Figure 2.4).

The image created by one focal point is not the complete image of the sample – rather, at any given instant, only one point of the sample is observed. The detector is attached to a computer which builds up the image, one pixel at a time. In practice, approximately 0.5 seconds might be required for a 512x512 pixel image (Leica TCS SP2). The limitation is in the scanning mirrors. Some confocal microscopes use a special Acoustic Optical Deflector (AOD) in place of one of the mirrors, in order to speed up the scanning, using high-frequency sound waves in a special crystal to create a diffraction grating, which deflects the laser light. By varying the frequency of the sound wave, the AOD changes the angle of the diffracted light, helping scan the sample quickly.

The thickness of the optical section scanned can be varied by selecting a different diameter ( $d$ ) of the confocal pinhole. This diameter is typically expressed in Airy Units (AU) and defined by Equation 2.1.

$$1AU = 1.22 \frac{\lambda}{NA} \quad (2.1)$$

where  $\lambda$  is the excitation wavelength in vacuum and NA is the Numerical Aperture of the objective lens used. The NA is in turn described as follows.

$$NA = n \cdot \sin \alpha \quad (2.2)$$

where  $\alpha$  is the half angle of the collected rays from the object point. In practice a compromise is typically exercised between depth discrimination, signal intensity and resolution. This topic is dealt with in great detail in the book by Pawley (75). As a consequence, a recommendation for practical cases is to use  $d = 1$  AU for the above reasons.

## 2.5 Green Fluorescent Protein (GFP)

The fluorescence of GFP inside the jellyfish *Aequoria victoria*, where it was discovered is due to the transfer of excitation energy from a Calcium activated protein *Aequorin* to the GFP, which emits light with the maximum intensity at 504 nm. The function of such *in vivo* fluorescence in the jellyfish is however not understood (76).

The cloning of the full length cDNA of GFP (77), the ability to express and excite fluorescence in other organisms without co-factors (73) and the continued fluorescence of GFP after fusing it to other proteins (78) established the protein as the leading endogenous protein marker for many years to come. Combining the tagging of proteins with other techniques, modifying the conditions under which fluorescence is observed as well as changing emission wavelengths has made the GFP (and XFP for all spectral variants) to a tool for non-invasive and *in vivo* measurements of complex interaction and biochemical studies.

### 2.5.1 GFP Structure

The GFP has a molecular weight of 27 kD and is a polypeptide made up of 238 amino acids. The crystal structure of the molecule (79, 80) forms what is often referred to as a ‘lantern-shape’. It consists of a barrel of diameter 2.4 nm and height 4.2 nm, built by 11  $\beta$  sheets. A single  $\alpha$  helix is located inside the barrel, with the fluorophore in the middle. The  $\alpha$  helix also closes the two ends of the barrel. The Fluorophore consists of a cyclised tripeptide of Serine, Tyrosine and Glycine, at amino acid (aa) positions 65, 66 and 67.

Table 2.3: The time for irreversible bleaching of various fluorescent proteins and their comparative Molar Extinction Coefficients ( $\epsilon$ ), i.e. the ability to absorb light passing through unit length of a substance at molar concentration, are listed here (modified from 82).

Fluorescent Protein	Molar Extinction ( $\epsilon$ ) ( $M^{-1}cm^{-1}$ )	Bleaching time (relative)
EBFP	31,000	3
ECFP	26,000	85
EGFP	55,000	100
EYFP	84,000	35
dsRed	72,500	145

### 2.5.2 XFP Variants

Variants of the basic GFP protein are now commercially available with different fluorescence maxima (for excitation and emission), allowing multiple probes to be labelled (Figure 2.5). These are also collectively referred to as XFP ('X' Fluorescent Protein). These have also been optimized for emission intensity to allow better signal to noise ratio and therefore in their designation as 'enhanced'. Currently Blue, Cyan, Green and Yellow Fluorescent Proteins are available commercially. In addition to these, a protein called DsRed (81) from *Discoma striata* has also been discovered. Some useful photophysical characteristics like bleaching times and excitation and emission maxima are included in Table 2.3, adapted from earlier work of 82.

### 2.5.3 Photoinduced Fluorophore Bleaching

Fluorescent molecules have a limit to the number of quanta of light they can emit. In the case of a single GFP molecule, it is  $10^5$  photons (83). This effect leads to an exponential loss of intensity in the labelled molecule (84), with the exact profile dependent on the intensity of the excitation. The precise mechanism behind photobleaching is not understood, but it has been shown that it is an irreversible process which modifies the fluorophore such that no more fluorescence can be observed (85). Additionally GFP appears to cause only limited damage to the cellular environment as compared to conventional fluorescent dyes that tend to release free radicals. The reason might lie in the fact that the fluorophore of GFP is protected from the surroundings by the  $\beta$  barrel (86).

### 2.5.4 Applications

The GFP and related fluorescence protein technology presents a universal reporter tool that makes a myriad of physical, fluorescence-based measurements possible. One of the more prominent methods include Fluorescence Resonance Energy Transfer (FRET), where protein-protein interactions are measured by tagging the interacting proteins with different fluorescent protein variants. The emission wavelength of the donor and absorption wavelength of the acceptor molecules needs to overlap, and the two proteins need to be in close proximity to each other. The simplest measure of FRET is whether emission is detected, done conveniently with a confocal microscope with the appropriate detection filters. Additionally the donor molecule also displays a decay channel, the average life-time which is reduced in the case of resonant transfer. Thus, FRET can also be measured based on the life-time of the donor fluorescence. The latter effect is termed fluorescence lifetime imaging (FLIM). The efficiency of energy transfer  $E$  at a distance  $r$  between the donor and acceptor is given by (87):

$$E(r) = \frac{R_0^6}{R_0^6 + r^6} \quad (2.3)$$

where  $R_0$  is the distance at which efficiency is half maximum, typically 2 nm to 6 nm. The FLIM effect of fluorescence decay has also been used on its own, for instance on four variants of GFP, each of which showed distinct lifetimes, even when cotransfected *in vivo* and after excited with the same wavelength of light (88).

GFP and its variants have also been modified such that their fluorescence intensity depends on the pH of their surroundings (89), something already accomplished with small molecules (90). Another class of Fluorescent protein tags has been modified as a Calcium sensor, using the FRET effect and is called the ‘cameleon’ (91). Donor and acceptor are covalently bound by a linker that brings the two parts together in response to binding to  $Ca^{2+}$ .

All this work demonstrates the kinds of biochemical and biophysical measurements that GFP based technologies have made possible for studies in living cells.

## 2.6 Computational Image Analysis and Quantification

Some of the classic studies in the area of quantitative microscopy, have been conducted well before the advent of video or digital microscopy. A good example is from 1946 – a measure of correction for erroneous counting of cell nuclei in 3-D



sections of fixed cells—the Abercrombie correction (92). It is given by the simple formula-

$$P = A \cdot \frac{M}{L + M} \quad (2.4)$$

where  $P$  is the average number of nuclear points per section,  $A$  is the crude count of number of nuclei seen in the section,  $M$  is the thickness ( $\mu\text{m}$ ) of the section, and  $L$  the average length ( $\mu\text{m}$ ) of the nuclei. While this and the modified measure by Williams (93) were based on data obtained by manual inspection and intervention, with the advent of fluorescence microscopy, many studies also involved quantitative imaging of living cells either using video or CCD cameras (e.g. 94, 95, 96). In the early years of live cell microscopy, methods for segmentation and tracking of cells (97, 98) were rapidly developed and adapted from other areas.

The output of such digital microscopy methods is typically a set of digital images. A typical 3-D plus time series (4-D) dataset for a single time step and spatial dimension of  $512 \times 512 \times 15$  has a size of approximately 4 Mega Byte. Considering hundred time steps and simultaneous measurement in three channels results in a data size of approximately 1,2 Giga Byte. The size and amount of images makes it almost impossible to analyze this data manually. Therefore there is a need for software-based solutions (99).

Nowadays, techniques for fully automated analysis and time-space visualization of time series from living cells involve either segmentation and tracking of individual structures, or continuous motion estimation (for an overview see Figure 2.6).

### 2.6.1 Filtering and Preprocessing

On inspection of the image from microscopy, it becomes apparent that along with the signal, there is also noise that has become part of the image. In an image where signal and noise can be distinguished, the ratio of the variance of the signal image ( $s_S$ ) to the noise image ( $s_N$ ) is called the signal to noise ratio (SNR). Filtering is a method that can change the image by making it smoother and improve the SNR.

Filtering of images can be used to suppress either the high frequencies in the image, i.e. smoothing the image, or the low frequencies, i.e. enhancing or detecting edges in the image. In its actual implementation, filtering can be applied either to the frequency or in the spatial domain.

Noise is random background seen in real signals and is not part of the ideal signal. It may be caused by a wide range of sources, e.g. variations in the detector sensitivity (CCD or PMT), environmental variations (cellular debris in the image-stage culture medium), the discrete nature of radiation, or transmission or quantization errors. If the noise is Gaussian in nature, i.e. with a normal distribu-



tion, it can be reduced using a spatial filter like the mean and median filters and Gaussian Smoothing.

### 2.6.2 Segmentation

The segmentation process is necessary to separate the objects from background. There is no standard segmentation algorithm available, which gives reliable results on arbitrary images. Typically used is a low-level threshold method or in case of sharp edge information, an edge based operator like the canny filter can be applied to extract the object border pixel. When using the edge based method, potentially disconnected edges need to be connected and fragments to be eliminated (101). This method is however very sensitive to noise.

### 2.6.3 Single Particle Tracking

For tracking a large number of small particles that move individually and independently from each other, *single particle tracking* approaches are most appropriate (102). The basic principle of single particle tracking is to find for each object in a given time frame its corresponding object in the next frame. The correspondence is based on object features, nearest neighbor information or other inter-object relationships. Object features can be dynamic criteria such as displacement and acceleration of an object as well as area/volume or mean gray value of the object. A reliable tracking approach involves fuzzy logic-based analysis of the tracking parameters (101).

### 2.6.4 Optical Flow

For the determination of a more complex movement, two independent approaches have been initially developed that were recently merged. *Optical flow* (103) methods estimate the local motion directly from local gray value changes in image sequences. Optical flow has been defined as the motion flow (i.e. the motion vector field) that is derived from two consecutive images in a time series (104). If optical flow is continuous, corresponding objects in subsequent images should be similar.

### 2.6.5 Registration

Image registration (105, 106) aims at identifying and allocating certain objects in the real world as they appear in an internal computer model. The main application of image registration in cell biology is the automated correction of rotational and translational movements over time (rigid transformation). This allows the identification

of local dynamics, in particular when the movement is a result of the superposition of two or more independent dynamics. Registration also helps to identify global movements when local changes are artifacts and should be neglected. Image registration enables a computer to “register” (apprehend and allocate) certain objects in the real world as they appear in an internal computer model. At first, only rigid transformations have been used to superimpose the images. Nowadays, research is focused on the integration of local deformations.

A parametric image registration algorithm specifies the parameters of a transformation in a way that physically corresponding points at two consecutive time steps are brought together as close as possible. Such algorithms have been broadly studied in medical imaging and cell biology (107, 108). While one class of algorithms operates on previously extracted surface points (105), other algorithms register the images directly based on the gray-value changes. Non-rigid deformations, i.e. transformations others than rotation and translation, present an active body of research in computer vision. Non-rigid approaches differ with respect to the underlying motion model (109, 106). Most commonly, a cost or error function is defined and an optimization method is chosen that iteratively adjusts the parameters until an optimum has been achieved. Other approaches extract specific features, e.g. correspondence between points, which serve as a basis for directly calculating the model parameters (110, 111).

### 2.6.6 Visualization

3-D images have been typically represented as stereoscopic pairs or as anaglyphs by pixel shift method (112). Displaying time series as movies is still a widely used method for visual interpretation. For fast moving objects such as trafficking vesicles imaged with high time-resolution, time-lapse movies are very informative. However, for much slower nuclear processes or for processes with mixed kinetics that need to be observed over a longer period of time, the total number of time points for imaging are limited due to the photo toxicity of the light exposure during *in vivo* observation (113). Therefore, an interpolation between consecutive time steps is required to reconstruct intermediate time steps. As a “side effect”, additional information about the continuous development of the observed processes between the imaged time steps (subpixel resolution in time) is achieved and quantitative information can be derived (see below). While early studies have explored 4-D datasets by simply browsing through an image gallery and by highlighting interactively selected structures (114), a better interpretation of 4-D imaging data is achieved by computer graphics. Two commonly used rendering algorithms for displaying 3-D structures are volume rendering and surface rendering (115, Figure 2.6). Volume

rendering is a technique for visualizing complex 3-D data sets without explicit definition of surface geometry. Volume visualization is achieved in three steps: classification, shading, and projection (e.g. 116). This method is limited to pure visualization and does not deliver quantitative information. In addition, the high anisotropy typical for live cell imaging with low z-resolution limits the quality of this visualization technique. These limitations are overcome by surface rendering techniques, where the object surface is represented by polygons. The polygonal surface is displayed by projecting all the polygons onto a plane that is perpendicular to a selected viewing direction. The user can examine the displayed structure by changing the viewing direction interactively. The most commonly used method to triangulate the 3-D surface is the Marching Cube algorithm (117). The 3-D structure is defined by a threshold value throughout the data set, constructing an isosurface. To obtain the neighborhood of the vertex points at different time-steps, a distance functional finds the optimal connection by minimizing the sum of all Euclidean distances of all permutations. The drawback of this method is that the surface of many biological structures cannot be defined using a single intensity value, resulting in loss of relevant information.

### **2.6.7 Signal Concentration Estimation**

A great advantage of the combination of segmentation and surface reconstruction is the immediate access to quantitative information that corresponds to visual data (118, 119, 120). These approaches were designed to deal particularly with the high degree of anisotropy typical for 4-D live cell recordings and to directly estimate quantitative parameters. E.g., the grey values in the segmented area of corresponding images can be measured to determine the amount and concentration of fluorescently labelled proteins in the segmented cellular compartments. Measuring concentration changes by fluorescence recovery after photobleaching (FRAP) and fluorescence loss in photobleaching (FLIP) give direct access to kinetic parameters such as the diffusion coefficient of molecules (121, 122, 123) or exchange rates of molecules between different compartments (15).

### **2.6.8 Quantitative Photobleaching Experiments**

The fluorescence recovery after photobleaching (FRAP) or fluorescence photobleaching recovery (FPR) experiment involves irreversibly photobleaching in a small area of the cell by a high-power focused laser beam. The diffusion of fluorescence signal from the surroundings leads to a recovery of fluorescence, which is recorded with low laser power, the same used before the bleaching. FRAP provides information of the mobility of the molecule being bleached, in the compartment it is localized.

FRAP experiments started in the 1970's using probes like fluorescein covalently bound to proteins and lipids (121, 122).

For spot photobleaching in two dimensions (as in lipid membranes), computational methods have been reported to deduce fluorophore diffusion coefficient ( $D$ ) from bleach spot profile and fluorescence recovery curve shape,  $F(t)$  (121, 124, 125, 126, 127). However, it is often invalid to apply exact theories to determine  $D$  because of a non-ideal laser beam profile, fluorophore diffusion during the bleach time, and other complexities such as non-cylindrical beam  $z$ -profile in three-dimensional aqueous compartments.

The application of Acousto Optic Modulators (AOM) to vary the intensity of the laser beam with a scanning microscope gives rise to scanning microphotolysis in which the laser intensity can be completely turned on or off, thus allowing a region of desired geometry to be scanned and bleached (128).

Figures 2.7a-d demonstrate the photobleaching technique graphically. In figure 2.7a region A is the region to be bleached, and B is the remaining area showing the signal, in this case in the nucleus. Figure 2.7e shows evolution of the normalized intensity over time, before and after photobleaching. The vertical arrow indicates the time at which signal was bleached. A variation of the FRAP, fluorescence loss in photobleaching (FLIP) involves repeatedly bleaching the same area at a constant time interval. This method qualitatively tests the immobility of a signal between different compartments and can be quantitatively evaluated for deriving off rates ( $k_{off}$ ). Two parameters are typically derived from FRAP experiments: the mobile fraction of molecules and the mobility, related to the characteristic diffusion time,  $\tau_D$ . The mobile fraction can be determined by comparing the fluorescence in the bleached region after full recovery ( $F_\infty$ ) with the fluorescence just before ( $F_i$ ) and after ( $F_0$ ) bleaching. The mobile fraction  $R$  is defined as (85):

$$R = \frac{F_\infty - F_0}{F_i - F_0} \quad (2.5)$$

In cases where diffusion is the underlying mechanism responsible for mobility, an effective diffusion constant ( $D_{eff}$ ) can be calculated. This is related to the characteristic diffusion  $\tau_D$  by the 2-D diffusion equation described in 121:

$$\tau_D = \frac{\omega^2 \cdot \gamma}{4 \cdot D} \quad (2.6)$$

where  $\omega$  is the radius of the focused beam and  $\gamma$  is the correction factor for the amount of bleaching.

The Diffusion constant obtained thus is correctly only a  $D_{eff}$ , effective diffusion constant, and a lower limit. This lower limit is useful if a comparison is made with some standard, like the diffusion in water, like work on mitochondrion targeted

GFP which showed diffusion not to be significantly different from diffusion of the same GFP variant in water (129), indicating that the mitochondrial matrix does not significantly hinder diffusion (130).

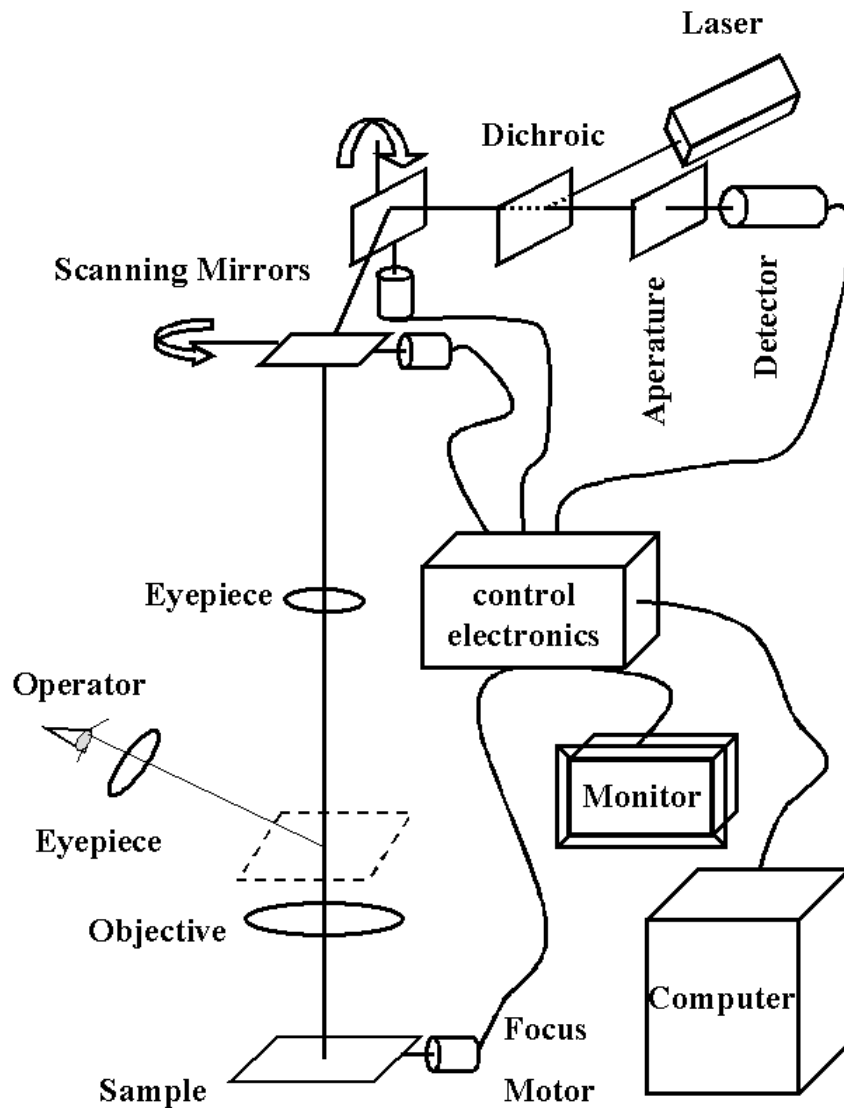


Figure 2.4: A typical confocal microscope set-up is schematically illustrated here. Here the laser fires light the exact position of which is controlled by mirrors that control X,Y and Z directions. These mirrors are moved by motors controlled by the electronics that coordinates the steering of the laser, the position of the sample, the laser, detector and monitor to display the output. The optics are based on the principle described in the previous figure with the incident light passing through the objective and eyepiece, also controllable, illuminating the sample and the emitted light being captured either through the eyepiece with the observer, or by the detector. The computer runs programs to coordinate control of the electronics and storing and processing the output (adapted from 75).

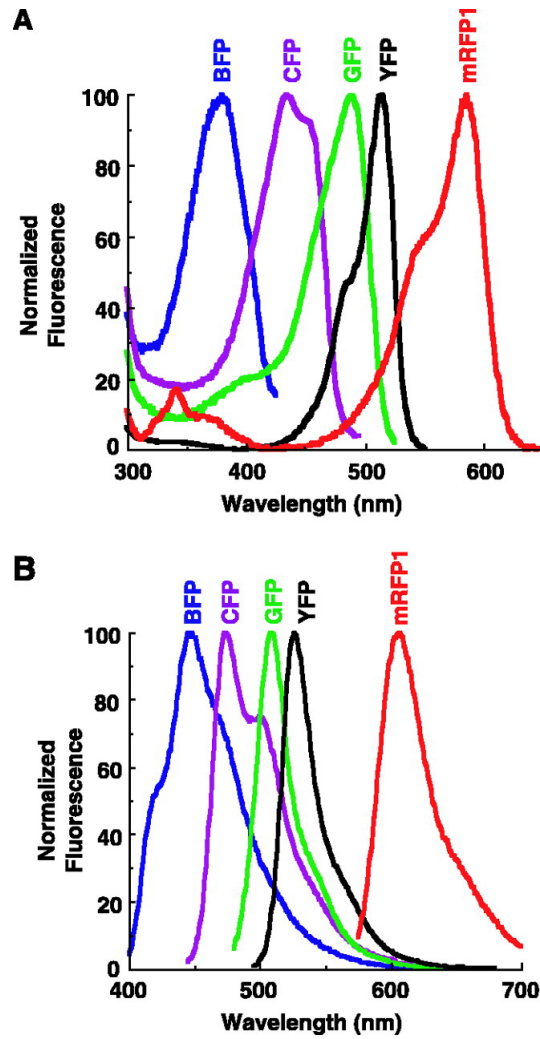


Figure 2.5: The excitation (A) and emission (B) spectra of the commercially available fluorescent proteins are mapped here (from the website of Clontech, USA). The process of selection of markers, especially when using multiple fluorescence labels, is an optimization between the separability of the emission peaks, the availability of the lasers and the phototoxicity to the cell.

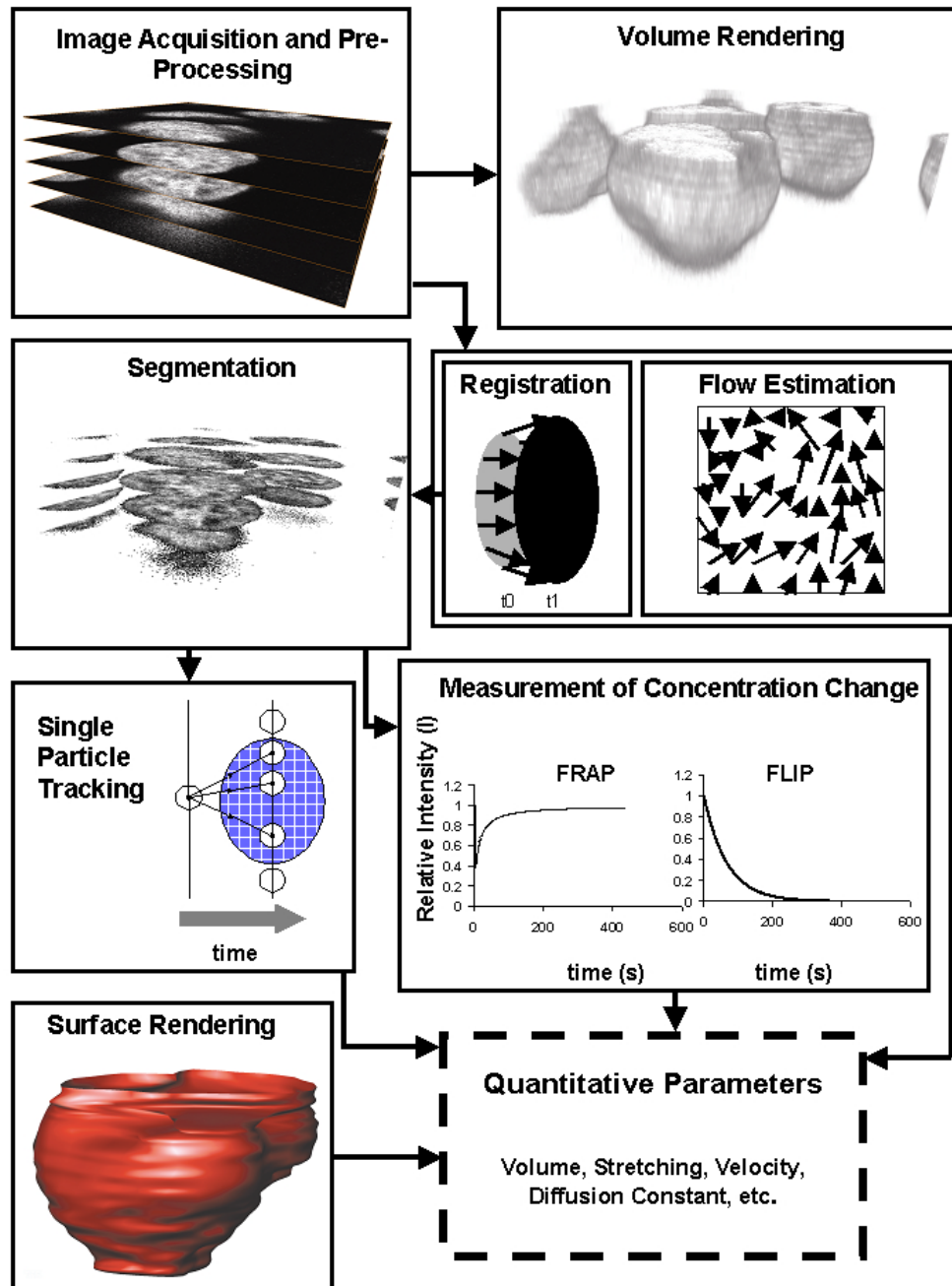


Figure 2.6: The typical workflow in image processing of multidimensional dynamic data from microscopy. The Box to the upper left shows the kind of typical 3-D image stacks that are obtained, here from confocal laser scanning optical sections. This can be immediately rendered with standard volume rendering algorithms, giving a clear idea of the spatial organization of the signal, in this case topoisomerase II  $\beta$  signal in the cell nucleus. The steps toward more discrete quantification typically goes over segmentation. Often a step of image registration is necessary to compensate for shifts in the data in 3-D or in time (100).



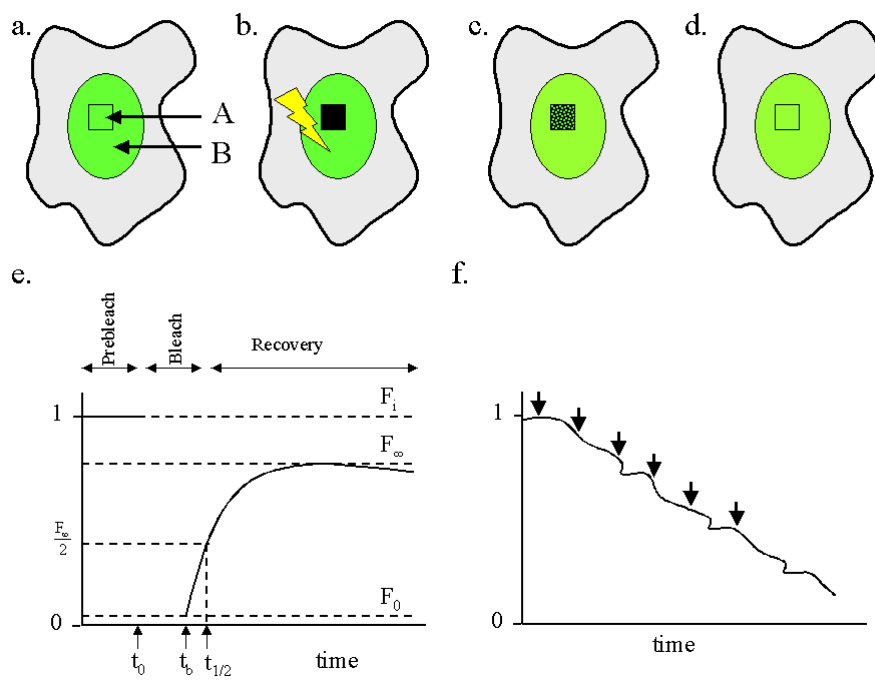


Figure 2.7: The principle of the FRAP experiment: a) The fluorescence of a cell before bleaching, b) immediately after bleaching and c) 10 min after bleaching. The figure d) schematically shows the changes in the relative intensity (y-axis) over time (X-axis) (modified from 85).

## 2.7 Modelling Diffusion in Cell Biology

The role of modelling in cell biology is two-fold. On the one hand in systems that are well characterized, there is a need to predict the state of a system, or some specific parameters in a certain condition. This commonly referred to as the Forward Problem. On the other hand is the Inverse Problem, where the state of a system is to be deduced from a set of measurements of it (131). The methods introduced here deal with both approaches. Typically the generic representation of the problem is made clear from the following equation which describes the task:

$$d = F(m) + \varepsilon \quad (2.7)$$

where  $d$  is the data,  $F(m)$  is the forward mapping operator and  $\varepsilon$  is the sum of all errors associated with data acquisition and pre-processing. Hence the forward problem is to find aspects of  $F$  and the inverse problem to find  $m$ . Since the work presented here deals with diffusion and mobility, I will introduce some of the methods used in cell biology, including diffusion and binding models, compartment models, finite difference spatial models and Monte Carlo simulations. What I do not touch upon, but has also been used in such studies in cell biology are cellular automata.

The fact that biology is wet and dynamic with cell, organelles and molecules constantly moving, raises many interesting questions. The mobility of most ligand molecules in solution is based on Brownian motion, and the average net flux from one region of space to another depends on both the mobility of the molecules and the 3-D concentration gradient between the two regions. In the following text some of the physical and mathematical models used to better understand these process are introduced.

### 2.7.1 Molecular Diffusion

Diffusion is the process by which matter is transported from one part of the system to another as a result of random molecular motions (132). The mathematical theory of diffusion in an isotropic (equal in all directions) medium is based on the hypothesis that the rate of transfer of a substance through unit area of a section is proportional to the concentration gradient measured normal to the section, i.e.

$$F = -D \frac{\partial C}{\partial x} \quad (2.8)$$

where  $F$  is the rate of transfer per unit area of section,  $C$  is the concentration of the diffusing substance,  $x$  the space coordinate measured normal to the section and

$D$  is called the diffusion coefficient. This is also referred to as Fick's First Law of Diffusion, formulated by Fick (1855) analogous to the equation of heat conduction.

The movement of particles in diffusion is due to thermal energy. Einstein showed in 1905 that a particle, irrespective of its size, up to sizes seen in light microscopes, at absolute temperature  $T$ , has kinetic energy associated with its movement, on an average  $kT/2$  along each axis ( $k$  is Boltzmann's Constant). Thus a particle of mass  $m$  and velocity  $v_x$  along the  $x$ -axis has a kinetic energy of  $\frac{mv_x^2}{2}$  (40). This quantity fluctuates but on an average:

$$\left\langle \frac{mv_x^2}{2} \right\rangle = \frac{k_B T}{2} \quad (2.9)$$

The mean square velocity from this is:

$$\langle v_x^2 \rangle = \frac{k_B T}{m} \quad (2.10)$$

and the root-mean square velocity is:

$$\langle v_x^2 \rangle^{1/2} = \left( \frac{k_B T}{m} \right)^{1/2} \quad (2.11)$$

At a microscopic scale, of a single molecule or particle consisting of many molecules, or even for a single bacterium, the net displacement by diffusion is then proportional to the square root of the mass.

## 2.7.2 Anomalous Diffusion

Solute diffusion is described as 'normal' or 'simple' in a homogeneous medium such as a liquid solvent, in which case solute transport is described adequately by a single diffusion coefficient. There are many environments and situations in which solute diffusion cannot be described in terms of a single diffusion coefficient. One example is anomalous diffusion.

The diffusion of a solute is said to be anomalous if the mean-squared displacement ( $\langle d^2 \rangle$ ) varies with time in a nonlinear manner. In such systems the diffusion coefficient is not constant, but time- and/or space-dependent. Saxton has addressed several potential mechanisms of anomalous diffusion that are relevant to solute transport in cell membranes involving binding and collisional interactions with mobile and immobile obstacles (133, 134, 135, 136, 137, 138). Another example of nonsimple diffusion is the presence of two or more diffusing species, each of which is described by a single diffusion coefficient. Without prior knowledge of the presence of multiple diffusing species, as is the case in cellular environments where heterogeneous binding can occur, the data can be wrongly interpreted as anomalous

diffusion. Recently, anomalous diffusion of fluorophores in planar membranes and polymer networks has been found (139, 140).

Photobleaching data in cell membrane and aqueous compartments have generally been analyzed in terms of a single diffusing component with or without an immobile fraction. In one study the possibility of two distinct diffusing species was considered (141). The potential pitfalls in the assumption of simple diffusion and the significance of long tail kinetics in diffusive phenomena have been recognized (142), and recent papers have begun to consider how to interpret photobleaching data in systems with complex or anomalous diffusion (139, 143, 14).

Work on the analysis of fluorophore diffusion by continuous distributions of diffusion coefficients showed that FRAP data,  $F(t)$ , can be resolved in terms of a continuous distribution of diffusion coefficients,  $(D)$ . An effective regression method to recover  $(D)$  from  $F(t)$  was developed, validated, and applied to experimental photobleaching measurements on defined fluorophore mixtures.  $(D)$  curve shape was then related to specific models of anomalous diffusion, and experimental examples are presented of anomalous subdiffusion and superdiffusion. An independent method to analyze  $F(t)$  for anomalous diffusive processes in terms of time-dependent diffusion coefficients,  $D(t)$ , was also developed and validated experimentally. The results indicate that determination of  $(D)$  and  $D(t)$  from photobleaching data provides a systematic approach to identify and quantify simple and anomalous diffusive phenomena. 144

### 2.7.3 Molecular Binding

One of the most important factors that often causes deviation from normal diffusion in biological systems at the molecular level is binding. In typical chemical notation, this is described as:



where  $L$  is the ligand,  $R$  is the receptor (or binding partner) and  $LR$  is the complex between ligand and receptor. Typically a simple way to treat this mathematically is to use mass action kinetics whereby the velocity of the reaction ( $v$ ) is given by:

$$v = k_{off} \cdot [LR] - k_{on} \cdot [L][R] \quad (2.13)$$

where  $k_{off}$  is the rate of the reverse reaction and  $k_{on}$  the rate of forward reaction in equation 2.12 and the bracketed quantities are the concentrations of the respective species, also described in equation 2.12.

Collision theory has shown that at the molecular level, the off-rate ( $k_{off}$ ) presupposes different things:

$$k_{off} \propto \text{steric req.} \times \text{encounter rate} \times \text{minimal energy req.} \quad (2.14)$$

where (req. = requirement). There exists detailed theory in physical chemistry for these kind of reactions and this is well treated elsewhere (145).

### 2.7.4 Compartment Models

A compartmental system has been defined elegantly by Jacquez (146) as being made up of a finite number of macroscopic subunits called compartments, each of which consists of *homogeneous and well mixed* material. Interaction between the compartments is modeled as an exchange of material from one compartment to the other. Flows might also come from the outside into one or many compartments (inflows) or material might flow out (outflows). The basic rule that holds is *mass conservation*. The system is inflow closed if there is no inflow in the system, and outflow closed if outflow is lacking. If the system is both inflow- and outflow-closed, it is referred to as a *closed system*. Compartmental systems can be linear or non-linear and are a special subset of non-negative systems. The mathematical theory dealing with the behaviour of such systems is called compartmental analysis.

The physical sciences and biology have been making use of compartmental analysis, partly because of its robust utility. In biology it has been used in diverse fields such as epidemiology, ecology, evolutionary biology, pharmacokinetics, metabolism and carcinogenesis.

Linear compartmental systems, both deterministic and stochastic, are very well understood and much work has been done and continues to be done in qualitative nonlinear compartmental systems. The area however that still needs attention are deterministic and stochastic nonlinear compartmental systems as well as the interesting inverse problem, dealing with system identification and parameter estimation.

Some of the commonly used terms in compartmental modelling are-

1. Space: Space or volume refers to a physical volume. For example the extracellular volume of a cell can be referred to as a space. The contents of a space may or may not be well-mixed and homogeneous, e.g. the nuclear, cytoplasmic or mitochondrial space.
2. Compartment: A compartment is defined as an amount of material that acts kinetically like a distinct homogeneous amount of the material. It is different from a physical volume or space, even if (as in some cases) the amount of material in such a volume may be a compartment too.

3. **Transfer Coefficient:** The arrow in a typical representation of compartmental systems (3.4) representing the transfer of material into and out of a compartment, is labelled as a transfer coefficient. The product of transfer coefficient and the amount in the compartment of origin gives the rate of transfer of material.
4. **Pool:** the term pool is used to designate an amount of some material that may consist of one or more compartments and may be distributed in more than one space. A pool may behave kinetically as one or many compartments, e.g. The entire intracellular pool of some molecule, whether it is bound or free, or sequestered in the nucleus.
5. **Steady State:** A system is in a steady state when all the state variables, such as compartment sizes, become constant, e.g. An open system with constant inflows and outflows may be in steady state and yet not be at chemical equilibrium.
6. **Turnover Rate and Turnover Time:** At steady state, the rate at which a compound enters or leaves a compartment is the turnover rate for the compartment or set of compartments. It has the units mass/time. The mass of the compartment/s divided by the turnover rate is the turnover time.

This has been used widely in physiology of whole organisms, but only recently been demonstrated to be useful in modelling protein secretion pathways by distinguishing between two alternative models of transport (15).

### **2.7.5 Spatial Diffusion with Partial Differential Equations (PDE)**

Diffusion of ligand molecules in solution is based on Brownian motion, and the average net flux from one region of space to another depends on both the mobility of the molecules and the 3-D concentration gradient between the two regions. One approach to computing the 3-D gradient is to subdivide space into small volume elements (voxels, typically cube-shaped), assume well-mixed conditions within each voxel, and then use 1D flux equations (partial differential equations, PDEs) to compute the average net changes across the interfaces between adjacent voxels. If the granularity of the spatial and temporal subdivisions is sufficiently fine, a numerical simulation will give the correct average behavior of the system. Additional PDEs can then be added to describe the average rates of chemical reactions within each voxel, and a simulation of space- and time-dependent diffusion and chemical reaction is obtained. Such approaches are very common in engineering and physics, but have only slowly begun to be used in cell biology. By the general balance law,

the rate of change of particles in a region B where particles are diffusing through, equals the net creation rate of particles in B plus the net rate at which particles flow into B across its boundaries. This is expressed as (147):

$$\frac{\partial C(x,t)}{\partial t} = Q(x,t) - \left( \frac{\partial J(x,t)}{\partial x} \right) \quad (2.15)$$

where  $Q(x,t)$  is the net creation rate,  $J(x,t)$  is the flux density or current (negative for a net flow in the direction of increasing  $x$ ) and  $C(x,t)$  is the particle density or particle concentration at point  $x$  and time  $t$ .

If  $Q = 0$ , combining equation 2.8 and equation 2.15, we get:

$$\frac{\partial C}{\partial t} = \frac{\partial}{\partial x} \left[ D(C) \frac{\partial C}{\partial x} \right] \quad (2.16)$$

Typically however concentration variations do not cause noticeable deviations in  $D$ , and then the diffusion equation takes the form

$$\frac{\partial C}{\partial t} = D \frac{\partial^2 C}{\partial x^2} \quad (2.17)$$

and in 3-D this becomes:

$$\frac{\partial C}{\partial t} = D \left[ \frac{\partial^2 C}{\partial x^2} + \frac{\partial^2 C}{\partial y^2} + \frac{\partial^2 C}{\partial z^2} \right] \quad (2.18)$$

These otherwise simple equations have proved useful in a variety of situations (132). One prominent example has been in the simulation of the fertilization wave of Calcium diffusion in *Xenopus laevis* eggs (17). This work numerically solved the model for gating by  $Ca^{2+}$  and showed bistability in the physiological state of the mature egg and tested the reasons for the shape of the fertilization wave. This method shows promise for further use as spatially resolved measurements become easier in cell biology.

## 2.7.6 Monte Carlo Simulations

The PDE approach to diffusion for simple spatial configurations can be extremely efficient, but for complex (i.e. realistic) structures the spatial subdivisions become correspondingly complex to plan and implement, and the number of voxels can grow to be very large. In any case, the simulation output provides no direct information about stochastic variability arising from finite numbers of participating molecules, which in biological systems is often of interest and can convey useful information. A completely different approach to the simulation of 3-D diffusion is to directly approximate the Brownian movements of the individual ligand molecules. In this case, random numbers are used to pick different possible directions and distances of motion during each time-step. Collisions with arbitrarily oriented surfaces

can be detected and handled appropriately, making voxels totally unnecessary. Similarly, collisions with potential binding sites can be detected and handled without voxels, using only random numbers together with a computed binding probability to make each decision. Since all possible events are considered on a molecule-by-molecule basis, the simulation results include realistic stochastic noise based on the spatial arrangement and number of participating molecules. The reliance on random numbers to make decisions is reminiscent of throwing dice, and the term “Monte Carlo” to describe this class of simulation was originally coined by Ulam and Von Neumann in the days of the Manhattan Project (148). These methods have been used to investigate the effectiveness of aggregation of membrane proteins in 2-D membranes, and at least qualitatively the aggregation of gel-phase lipid during lateral phase separation (149). Using Monte Carlo simulations, a study has been conducted to examine anomalous diffusion due to binding (138). The influence of architecture on diffusion in mitochondria and the endoplasmic reticulum (14) also used these methods and its findings support the paradigm that organellar barriers must be quite severe to seriously impede solute diffusion.

## **2.8 Aim of the work**

Although different models exist for the dynamics of nuclear bodies in the interchromatin space, at the time of beginning this project, they had not been explicitly tested with integrated mathematical modelling and nuclear body mobility studies. The work presented in the following chapters aims to formulate models of nuclear body dynamics relating to their mobility and stability. These models are tested by a comparison between on the one hand experiments involving 4-D live cell microscopy, FRAP of inert and biologically active molecules and image analysis, and on the other hand simulations by discrete and continuous methods. Through an iterated comparison of experiment and simulation, an attempt is made to arrive at a better understanding of nuclear bodies, and in turn the organization of the interchromatin space.



# Chapter 3

## Materials and Methods

“...we do not demarcate scientific theories from pseudoscientific ones, but rather scientific methods from non-scientific methods.”

-Imre Lakatos in *Science and Pseudoscience*

This work was conducted using methods drawn from experimental cell biology, microscopy, image processing and modelling of diffusion and transport. This wide range of methods is necessary in order to approach the problem in a manner consistent with the stated aims of systems biology of focusing on the arrangement of the parts that connect them into a whole, as expressed by von Bertalanffy (150) and restated recently by Kitano (151).

## 3.1 Cell Culture

### 3.1.1 Cell Types

An adrenal cortex carcinoma-derived cell line lacking endogenous vimentin, SW13 (152) was used for studies in which NLS-vimentin was expressed ectopically. The cell-line SW13 clone 14 used in initial experiments expresses a genomic copy of the *Xenopus*-NLS-vimentin (38). This was transiently transfected with a copy of GFP-*Xenopus*-NLS-vimentin (60) and later a stable cell line was used which expresses both N-terminal GFP tagged and untagged *Xenopus*-NLS-vimentin (M. Reichenzeller, manuscript in preparation).

A normal rat kidney (NRK) fibroblast cell line with a stably transfected Histone2B (H2B) CFP (153) was used for labeling the chromatin. This cell was a generous gift of Jan Ellenberg and Daniel Gerlich (Cell Biophysics Laboratory, EMBL, Heidelberg).

### 3.1.2 Passaging of Cells in Culture

Materials:

1. DMEM: Dulbecco's Modified Eagle Medium with Earl's salts and Phenol Red
2. DMEM w/o Phenol Red: DMEM without the indicator Phenol Red
3. DMEM/FCS/PenStrep: DMEM with 10% (v/v) Fetal Calf Serum (FCS), Seromed, Berlin), 20 mM Glutamine and 100  $\mu\text{g}/\mu\text{l}$  Pennicillin and Steptomycin (Invitrogen, Karlsruhe).
4. PBS/EDTA: 0.5 mM EDTA in PBS
5. Trypsin-solution: 0.25% (w/v) porcine Trypsin (BD, Heidelberg) in PBS/EDTA

Methods:

The cell cultures used SW13 and NRK (normal rat kidney) were cultured at 37°C in

a moist atmosphere with 50%  $CO_2$  in DMEM/FCS/PenStep in 35 mm Petri Plates (Becton-Dickinson, Heidelberg). The MCF-7 and 3T3 cells that were also cultured, were kept under similar conditions, except for the PenStrep which was excluded. The cultures were maintained in the logarithmic phase of growth by splitting the culture every three to four days, as soon as they appeared confluent under the dissection microscope. The cells were split by the following method- The old medium was removed and the confluent cell-layer washed with 3 ml of PBS/EDTA solution. Subsequently, approximately 300  $\mu$ l Trypsin solution was pipetted on the cell-layer, ensuring that it formed a thin film over all the cells. These cells were then placed in the incubator at 37°C and 5%  $CO_2$  for approximately 5 min or till they detached from the bottom of the Petri Plate or coverslip, as the case might be. These cells were then removed from the incubator, resuspended in 5 ml fresh DMEM/FCS/PenStrep and added in the required dilution to the new Petri dish. If the cells were for fixation and observation, they were plated in a Petri Plate with an autoclaved coverslip of a diameter of 12 mm placed at its bottom. For studies involving live cell imaging, the cells were plated on coverslips with a diameter of 35 mm in 60 mm cell culture plates.

### 3.1.3 Transient Transfection of Cells

Transfection is the introduction of foreign DNA in the eukaryotic cell. The method used was one using a commercial lipid based Fugene6 (Roche Diagnostics, Mannheim, Germany) reagent. The cells were plated at such a dilution that at the start point of transfection, they were 50-80% confluent. For every transfection with cells in 35 mm (60 mm) culture plates, 97 (242.5)  $\mu$ l DMEM was placed in a 1.5 ml Eppendorf tube. To this 3  $\mu$ l (7.5  $\mu$ l) of the transfection reagent (Fugene-6) was pipetted and mixed. In a separate but identical tube, 2  $\mu$ g (5  $\mu$ g) DNA was added. The medium and transfection agent mixture was added drop-wise and incubated at room temperature for 15 to 30 minutes. After this the complete transfection solution was added drop by drop to the cells that were to be transfected. The bracketed quantities refer to those for a 60 mm culture plate.

### 3.1.4 DNA

A plasmid pEYFP-C1-NLS (154) construct was used for transfection and fluorescence recovery after photobleaching (FRAP) studies. This plasmid is based on the vector pEYFP-C1 (BD Biosciences Clontech, USA), which has the coding sequence of Enhanced Yellow Fluorescence Protein (EYFP), flanked upstream by a Kozak consensus translation initiation site to increase the translational efficiency of the EYFP mRNA. The Multiple Cloning Site (MCS) in pEYFP-C1 is between the

EYFP coding sequence and the stop codon. Genes cloned into the MCS will be expressed as fusions to the C-terminus of EYFP. The vector contains an SV40 origin for replication and a neomycin resistance (Neor) gene for selection (using G418) in eukaryotic cells. A bacterial promoter (P) upstream of Neor expresses kanamycin resistance in *E. coli*. The vector backbone also provides a pUC19 origin of replication for propagation in *E. coli* and an f1 origin for single-stranded DNA production. The recombinant EYFP vector can be transfected into mammalian cells using any standard transfection method. If required, stable transformants can be selected using G418. The NLS was derived by cloning the SV-40 NLS (amino acid sequence: APPKKRKRVG) into the BspEI- and EcoRI recognition sites. This plasmid was prepared and kindly gifted by Michaela Reichenzeller

### 3.1.5 Methanol Acetone Fixation of Cells

The coverslips were removed from the culture dishes and washed immediately in a bath containing PBS with 2 mM  $MgCl_2$ , preheated to 37°C (or the temperature at which the cells had been growing). After this they were fixed in a bath containing cold (-20°C) Methanol ( $CH_3OH$ ) for 5 mins. As a final step they were permeabilized with cold Acetone for less than 30 s. In the absence of any other detection method, these coverslips were dried on a sheet of 3mm Whatman paper (with the cells facing up). The cells were then mounted with a drop of FluoromountG on a clean glass slide.

## 3.2 Live Cell Microscopy

This is the method used for gathering data for analysing the dynamics of *in vivo* processes.

### 3.2.1 Culturing Cells under the Microscope

1. DMEM w/o Phenol red (Invitrogen, Karlsruhe, Germany)/FCS/PenStrep
2. Perfusion Open and Closed Cultivation chamber (POC-Chamber-System, Helmut Sauer Laborbedarf, Reutlingen, Germany)
3. Heated  $CO_2$  Chamber with Gas and Temperature Regulator (Tempcontrol 37-2 digital, CTI-Controller 3700, PeCon GmbH, Erbach, Germany)

Cells for live observation under the microscope were grown on 35 mm coverslips in Petri plates as described in section 3.1.2, transfected if necessary and the

next day observed under the microscope. The transfer from incubator to the microscope was done in a styropor box to prevent heat loss. The coverslip was transferred onto the POC chamber for closed observation, and locked in place sequentially with a silicon gasket and lastly a plastic-ring and a metal screw ring which was screwed tight with a mounting key. The adherent cells were then washed with 2 ml and later immersed in 3 ml of warmed DMEM/FCS/PenStrep w/o Phenol red. On top of all this an optically transparent glass-cover was placed, to minimize evaporation of the medium.

The cells were maintained under standard conditions of 37°C temperature with a heated microscope stage and a moist, 5%  $CO_2$  containing atmosphere. Both conditions can be independently varied.

The cells in the POC chamber were placed in a harness in the heated microscope stage, surrounded by the incubation chamber. The lid of the incubation chamber was then closed, in order to maintain a constant level of the  $CO_2$ . The  $CO_2$  level and temperature in the incubation chamber were monitored by sensors and the display of the gas and temperature regulators respectively. Water was introduced by hand in the side-chambers of the incubation chamber.

### 3.2.2 ATP Depletion with Na-Azide

To test the effect of inhibition of ATP synthesis is a method typically employed to test energy dependence of processes. Azide inhibits the production of ATP by oxidative phosphorylation, whereas 2-deoxyglucose inhibits ATP production by glycolysis. The medium was exchanged for an Azide/Deoxyglucose solution (PBS with 10 mM  $NaN_3$ , 50 mM Deoxyglucose, 1 mM  $MgCl_2$ , 0.5 mM  $CaCl_2$ ) (155, 156, 157) and the cells incubated for 30 min. Subsequently the medium was washed, removed and replaced by normal culture medium.

## 3.3 Confocal Laser Scanning Microscopy

A confocal laser-scanning microscope, Leica LSM SP2 (Leica Microsystems, Germany), was used for 3-D, 4-D and multichannel imaging of cell dynamics. All confocal images were acquired on a Leica TCS SP2 Microscope (Leica Microsystems, Germany). The microscope is equipped with the lines of laser light described in Table 3.1.

Fluorescence microscopy was used for all the work described here. The wavelengths were selected specific to the excitation and absorption wavelengths of the fluorophore used. Table 3.2 lists the fluorophores. In experiments described in Section 3.3.1 YFP and CFP were used in tandem.

Table 3.1: *The lasers, their nominal power and wavelengths available with the Leica TCS SP2 Confocal Laser Scanning Microscope.*

Type of Laser	Laser Power	Wavelengths
Cadmium-Ion Laser	2 mW	433 nm
Argon-Ion Laser	65 mW	458, 478, 488, 514 nm
Helium-Neon Laser (green)	1.2 mW	543 nm
Helium-Neon Laser (red)	10 mW	633 nm

Table 3.2: *The fluorochromes used in the work described here have their optimal excitation and absorption wavelengths. This was adjusted with the available wavelengths of light with the microscope. In the case of CFP and YFP since they were imaged in the same cell, they needed to be well separated. ECFP has 2 excitation and emission maxima.*

Fluorochrome	Excitation Max.(nm)	Emission Max. (nm)
EGFP	490	509
EYFP	513	527
ECFP	433	475
“	453	501

The images of NLS-GFP-vimentin were obtained in fluorescence mode using an Oil-Immersion Plano-Apochromatic 100x/1.41-objective lens. To optimize the efficiency of light collection, for some experiments were done with the 63x-objective. The resolution obtained in the x-y directions was typically 200 nm and in the z-direction 300 nm. GFP excitation was done by using an Argon-Ion laser and a reflection short pass filter (RSP) RSP500. Detection of emission was done between 505 and 540 nm.

In the case of experiments with NLS-YFP and H2B-CFP the excitation wavelengths used were 514 nm and 458 nm respectively and 451-561 nm for detection, with a double dichroic (DD) DD458/514 filter used to separate the excitation wavelengths. The DD458/514 allows the passage of 458 and 514 nm  $\pm$  3 nm wavelengths.

During imaging the detection minimum was set with the lens shut and adjusting the the Photomultiplier tubes (PMT) and the maximum such that the complete dynamic range of the PMT could be exploited. These settings combined with a low laser intensity, were optimized to minimize photodamage and maximize the signal (113).

### 3.3.1 FRAP

Fluorescence recovery after photobleaching (FRAP) experiments are performed typically to determine the extent to which molecules are mobile and quantify that mobility with a simple diffusion constant ( $D$ ) or more complex models. To bleach a fluorophore, the same laser was used that was being used for imaging. In FRAP experiments with NLS-YFP, the cell was imaged in 2D over time where the signal was a diffusing NLS-YFP protein localized in the nucleus. After focusing on the region of interest, one image each was acquired with the exact settings (zoom, laser intensity, time span, image size and frequency) as the pre-bleach, bleach and postbleach images. This was recorded as a macro in the the microscope software package accompanying the Leica microscope (Leica Microsystems, Germany). The settings included 10 *pre-bleach* images in a mode identical to that used later, except in the number of frames to be acquired. If no background material was in the focal area/volume, an image of it was acquired for subsequent normalization. Depending on the region to be bleached two kinds of experiments can be defined

1. Spot Bleach: To bleach a spot, the "zoom-in" function of the microscope was used to focus on a smaller area of the cell and the same zoomed out area was imaged in pre- and post-bleach images.
2. Entire Image Field Bleach: Here the entire area under observation was bleached by simply changing the laser intensity as compared to the pre- and post-bleach (imaging) parts of the protocol. Typically this was done with rectangular images, 512 x 32 or 512 x 64 pixels in size..

The bleaching was repeated typically 5-10 times, varying for the fluorescent marker so that the intensity of the signal in the bleached area was not measurable any more. Immediately after this, 100 images were acquired with the highest possible time frequency given the other settings. For the experiments with NLS-YFP in SW13 cells these were  $\delta t = 77$  ms with an image size of 512 x 32 pixels, laser frequency 1000 lines/second, no averaging, bidirectional scanning, time to acquire each image = 16 ms. The bidirectional scanning needed to be set in phase, and this was done by reducing the resolution of the image and maintaining the cell or nuclear boundary in the field of view, and adjusting the x-shift to make the outline continuous. To optimize the time for post-bleach images, once fluorescence intensity was observed to have reached a plateau, the time resolution was reduced to 1-5 s, and *post-bleach* images acquired for another 100-200 frames, to test whether any further recovery might be observed.

Typically the data are collected as sum image intensities and averaged over the area (see Section 3.4). These values are then plotted as relative intensity ( $I_{rel}$ ) in the bleach region. For experiments where only a region of the cell was bleached:

$$I_{rel} = \frac{T_0 \cdot I_t}{T_t \cdot I_0} \quad (3.1)$$

where  $I_t$  is the average intensity in the region of interest (ROI) at time  $t$ ,  $I_0$  is the average intensity in the ROI before the bleach,  $T_t$  is the total cellular intensity at time  $t$  and  $T_0$  is the total cellular intensity before the bleach.

For experiments where the whole field of imaging was bleached and the ROI is the whole image and  $I_{rel}$  is (158):

$$I_t = \frac{F_t - F_0}{F_\infty - F_0} \quad (3.2)$$

where  $I_t$  is the relative normalized intensity,  $F_t$  is fluorescence intensity at time  $t$ ,  $F_0$  the intensity immediately after the bleach pulse and  $F_\infty$  is the intensity at the final time point. This sets the initial post-bleach intensity (at  $t = 0$  s) to zero and  $F_\infty$  the final intensity. The data is plotted as normalized intensity values against time. In order to compare two experiments, with a single parameter, half times are calculated. Regression analysis is performed by calculating the least squares fit using the standard first order logarithmic equation:

$$y = c \ln x + b \quad (3.3)$$

where  $c$  is the slope,  $b$  is the  $y$  intercept and  $\ln x$  is the natural logarithm function of the time and  $y$  is the fully normalized intensity at a given time. As a result of the normalization of the intensities, the  $t_{1/2}$  value can be readily observed from the graph as the time at which the normalized intensity reaches 0.5 arbitrary units.  $t_{1/2}$  was calculated using the following equation when  $y = 0.5 \cdot F_\infty$ :

$$x = e^{((0.5-b)/c)}. \quad (3.4)$$

Another parameter extracted is the mobile fraction  $R$  is defined as (85):

$$R = \frac{F_\infty - F_0}{F_i - F_0} \quad (3.5)$$

where  $F_\infty$  is the fluorescence in the bleached region after full recovery,  $F_0$  Fluorescence just after bleaching and  $F_i$  Fluorescence before bleaching. If the fluorescence of the bleached region after bleaching reaches a plateau that is lower than that before bleaching ( $I_\infty < I_0$ , in a relative intensity plot over time, then it can be assumed that a fraction of the protein is immobile. The term ‘immobile fraction’ is invoked only in connection with the time scale.



## 3.4 Image Processing of Microscopy Data

The images obtained from the microscopy were saved usually as gray value image series with a typical naming convention as follows:

*date\_z[position in z-stack]\_t[position in time series].tif*

For examination purposes these images were also displayed in false colour by attaching a look up table (LUT) in one of the software packages like LSM 5 Image Browser (Carl Zeiss GmbH, Jena, Germany).

### 3.4.1 Filtering of Images

The noise reduction of the images was performed with filters, selected on the criterion of how close the final result was as compared to the expectation. The most frequently used filters were the Gaussian, Mean and Median Filters as implemented in TillVisTrac (Till Photonics, Germany) and Adobe Photoshop (Adobe Systems Inc., USA).

Useful for local filtering of noise is the Anisotropic Diffusion Filter (AID) (159, 101), since it tends to preserve edge information while reducing noise.

### 3.4.2 Segmentation of Images

Segmentation was performed in different parts of the work using the algorithm that best met the needs. Most robust was Manual Thresholding. Sometimes, when the edges were clear, Automatic Thresholding based on a histogram was used. The manual threshold was set interactively. The selection of the parameter was done based on the criterion, that it was robust to small changes in a region. As has been documented on many occasions, automated methods in image detection remain inferior to human inspection. However two commonly used methods were implemented in MATLAB (Appendix using the mean, and median value of the gray values of an image).

### 3.4.3 Intensity and Volume Estimation

Once the images were segmented, the outline of the objects in 3-D were used to sum the intensity of the object in the original gray-value images. Similarly the method of Voxel counting (or Pixel counting for areas in 2-D) 160 was used to calculate volumes of objects. The code for a simple voxel counting algorithm in MATLAB6 is attached in the Appendix A.

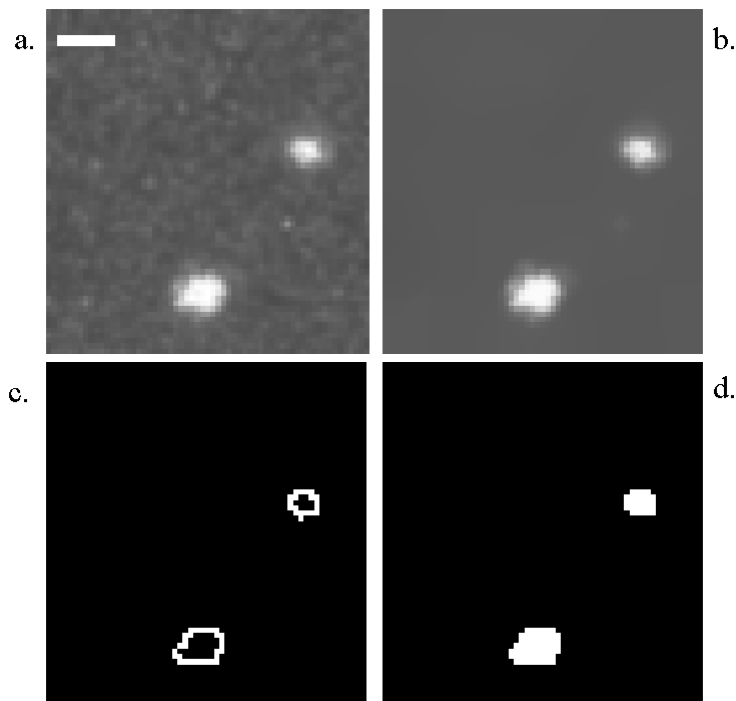


Figure 3.1: The images of fluorescent protein in discrete foci in a subsection of a cell image can be typically treated in the following sequence- a. A gray value image with maximum contrast, b. After anisotropic diffusion filtering, c. Segmentation with edge detection, d. The binary image with two segmented objects. The scale bar is  $1\ \mu\text{m}$ .

### 3.4.4 3-D and 4-D Visualization

The trajectories generated in the tracking process can be evaluated by visualization and quantification. One visualization approach used from the software package TillVisTrac (Till Photonics, Munich, Germany) is based on cubic B-splines. Another method used was generation of iso-surface reconstructions, mainly for visualization of the data. This method was used as implemented in the software package Amira v 2.3 (TGS Inc., USA)

### 3.4.5 Single Particle Tracking

Particle Tracking was used as implemented in the software package TillVisTrac (101). The tracking process output was a trajectory file with the Cartesian coordinates of the centre of mass of the tracked object, the area and total intensity of each object in 2-D and its velocity from one time frame to another. The evaluation process output was a diffusion constant and a surface rendering of the data-set.

### 3.5 Monte Carlo Simulation of Particle Diffusion

The Monte Carlo simulation was written in C with Open Inventor libraries for visualization in 3D over time. The algorithm used is the standard Ermak-McCammon algorithm (161). The model uses the volume exclusion of chromosome territories to create the inter chromosomal domain (ICD) space. In this space the hypothesized mechanisms of diffusion with energy dependent slowing were tested. The algorithm is illustrated schematically in Appendix B.

The displacement of a particle is given by:

$$r(t + \Delta t) = r(t) + \frac{D \cdot F \cdot \Delta t}{kT} + R \quad (3.6)$$

where  $D$  is the translational diffusion constant of the particle,  $F$  is the force acting on the particle, and  $R$  is random displacement added in to mimic the effects of collisions with solvent molecules. The translational diffusion constant is given by the Stokes-Einstein Relation:

$$D = \frac{k_B \cdot T}{6 \cdot \eta \cdot a} \quad (3.7)$$

where  $\eta$  is the solvent viscosity,  $a$  the radius of particle. The random displacement has the property that

$$\langle R \rangle = 0 \quad (3.8)$$

$$\langle R \cdot R \rangle = 6 \cdot \pi \cdot D \quad (3.9)$$

$$(3.10)$$

### 3.6 Discrete Diffusion Analysis of Particles

The analysis of diffusion processes both experimental and simulated was performed to understand whether the process of single particle diffusion might be influenced by other factors, and then design experiments to further test this. Some of the parameters that were measured were:

#### 3.6.1 Velocity

The velocity of motion of a particle was measured as the rate of change in the Euclidean distance between subsequent positions over time:

$$v = \frac{\sqrt{(x_t - x_{t-1})^2 + (y_t - y_{t-1})^2 + (z_t - z_{t-1})^2}}{\Delta t} \quad (3.11)$$

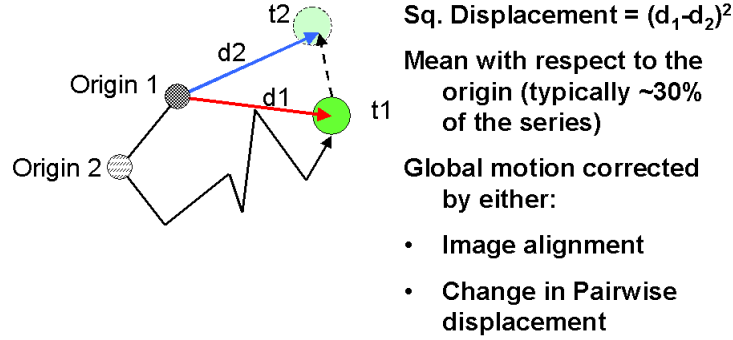


Figure 3.2: The typical data that is input into calculation of the mean square displacement is shown here. The expression typically relates to the relative movement away from the start position, represented as origin 1 or origin 2. The average of the square of the displacements at time  $t_1$  and  $t_2$  increases linearly in a diffusive process without boundaries. To correct for movement of the cell in which this is taking place, the change in pairwise distance also gives the same result. An alternative is to correct the data for global motion.

where the centre of mass of the particle at its initial position, say  $P_{t-1}$  is  $(x_{t-1}, y_{t-1}, z_{t-1})$  and the subsequent positions is  $P_t$  with coordinates  $(x_t, y_t, z_t)$  in the time interval  $\Delta t = 1$ .

### 3.6.2 Mean Square Displacement

The MSD is calculated as demonstrated in Figure 3.2 where the displacement from a chosen origin is the final measure. For a particle in motion it is given by:

$$\langle d^2 \rangle = \langle [d(t) - d(t + \Delta t)]^2 \rangle \quad (3.12)$$

where  $d(t)$  is the Euclidean distance travelled and  $\Delta t$  is the time interval between measurements. To correct for global motion of the object being measured, here a living cell, typically pairwise distance and its change was measured:

$$d(t) = \sqrt{(x_a - x_b)^2 + (y_a - y_b)^2 + (z_a - z_b)^2} \quad (3.13)$$

where  $(x_a, y_a, z_a)$  and  $(x_b, y_b, z_b)$  are the coordinates of the centre of masses of two particles, measured at the same time,  $t$ .

### 3.6.3 Effective Diffusion

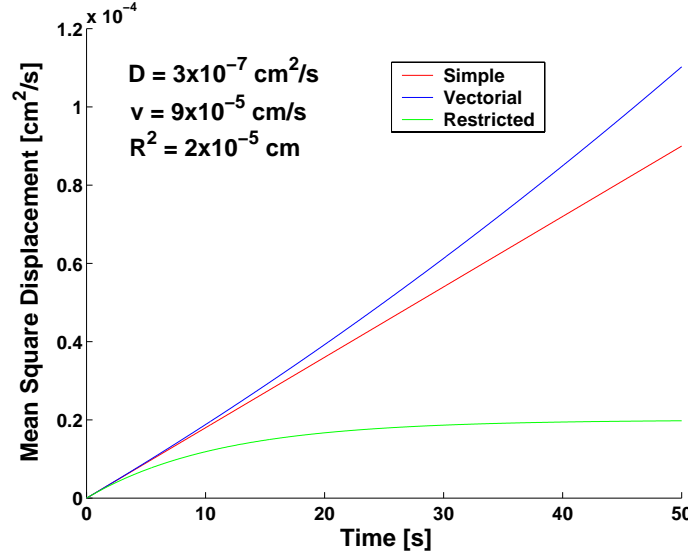


Figure 3.3: The three typical modes of diffusion simple (red), vectorial (blue) and restricted (green) which are analyzed for in data of diffusion of single particles after single particle tracking and simulation.

When plotting the experimental measured msd versus the time interval, three different forms of effective diffusion can be distinguished, the simple (red), vectorial (blue) and restricted (green) diffusion, as shown in Figure 3.3. The detailed expressions for these regimes of motion are given below (108).

1. Diffusion For a pair of particles undergoing free diffusion in three dimensions, it can be shown that the MSD  $\langle \Delta d^2 \rangle$  plotted against  $\Delta t$  shows a linear increase (102). For a given time interval the MSD is defined by:

$$\langle \Delta d^2 \rangle = 6 \cdot D \cdot t \quad (3.14)$$

where  $D$  is the diffusion constant and  $t$  the time.

2. Diffusion with Vecotorial Flow If diffusion has an additional component of directed flow then the MSD expression is modified to:

$$\langle \Delta d^2 \rangle = 6 \cdot D \cdot t + v^2 \cdot \Delta t^2 \quad (3.15)$$

where  $v$  is the flow velocity.

3. Diffusion with Obstruction In the case that the diffusion is taking place in a restricted environment, then this expression for MSD changes and if the movement is observed for long enough it takes the form:

$$\lim_{\Delta t \rightarrow \infty} \langle \Delta d^2 \rangle = R^2 \quad (3.16)$$

where  $R$  is the radius of restriction, assuming a spherical restriction.

On the other hand, when the Diffusion constant is known by experimental evaluation it is possible to estimate the viscosity of the underlying aqueous phase of the nucleus. For a spherical approximation and constant temperature, the viscosity can be calculated by the Stokes-Einstein relation:

$$D = \frac{k_B \cdot T}{f} \quad (3.17)$$

where  $k_B$  is the Boltzmann constant,  $T$  the absolute temperature in Kelvin and  $f$  the frictional coefficient. The frictional coefficient ( $f$ ) is related to the size of the moving object and medium as follows:

$$f = 6 \cdot \pi \cdot \eta \cdot a \quad (3.18)$$

where  $\eta$  is the effective viscosity of the medium and  $a$  is the hydrodynamic radius of the particle. The hydrodynamic radius is the longest radius of the particle, and is considered as an upper limit for non-spherical particles. For the 2-D case, the expression in Equation 3.18 changes to  $4 \cdot \pi \cdot \eta \cdot a$ .

### 3.6.4 Anomalous Diffusion

The MSD of a particle undergoing ideal diffusion is proportional to  $\Delta t$ . If obstruction to motion or binding becomes involved then the linear relationship is disrupted, resulting in anomalous diffusion. The MSD becomes proportional to a fractional power of less than one:

$$MSD \sim \frac{2}{d_w} \quad (3.19)$$

where  $d_w$  is the anomalous diffusion exponent. Values in the range  $d_w > 2$  are indicative of anomalous diffusion (59). For free diffusion, plotting  $MSD/Dt$  against  $Dt$  on a log-log-scale would result in a line parallel to the X-axis. For anomalous diffusion, a straight line with a negative slope of  $(2/d_w - 1)$  is obtained. According to theory, short time intervals in such plots generate negative slopes, and in the long time intervals the effects of short-term binding are averaged and the plots change to a horizontal line (138). The position of the transition from anomalous to normal diffusion, the crossover time ( $t_{cr}$ ), is a measure of the number of obstacles and the affinity of binding sites. With a decrease in number or in affinity of binding sites, a decrease occurs in  $d_w$  and  $t_{cr}$ , since the probability of interaction decreases.

### 3.6.5 Statistical Testing of Models

To compare the fits between data and different models of diffusion, I used a statistical F-max test for hypothesis testing. The critical value of the F-statistics was calculated at  $P = 0.05$  and the appropriate degrees of freedom based on the data and comparison with the standard tables (162).

## 3.7 Coupled ODE Simulation of Subnuclear Distribution

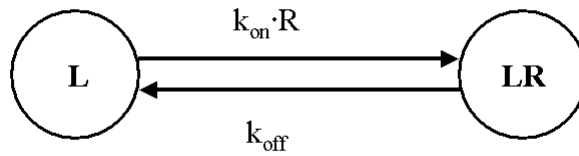


Figure 3.4: A compartment for a simple binding model where  $L$  is the free Ligand in the reaction volume,  $R$  are free receptors and  $LR$  are receptor bound ligands.  $k_{on}$  is the rate of association and  $k_{off}$  the rate of dissociation.

I used the method of compartment analysis and modelling (146) to represent the exchange of the nuclear protein TopoIIb between the nucleolus and the nucleoplasm using the software package SAAM II v1.2 (SAAM Institute, University of Washington). The system under observation is split into multiple subsystems (compartments). All molecules in a compartment are assumed to kinetically identical. It is assumed that there is instant mixing when material flows into or out of the compartment ('well-mixed'). The number of molecules in a compartment can be characterized fully by the number of molecules in it. Flows between compartments are represented by positive flux rates, which could be constant or change with time. The Mass Balance of a compartment is the result of addition of all inflows and outflows. For example in the case of the model in Figure 3.4 the change in ligand mass  $\Delta L$  in a time interval  $\Delta t$  given by:

$$\Delta L = k_{off} \cdot LR \cdot \Delta t - k_{on} \cdot R \cdot L \cdot \Delta t \quad (3.20)$$

A model structure was constructed based on the available knowledge of subnuclear distribution of Topoisomerase II $\beta$  and some what if questions asked to predict different testable scenarios.

### 3.8 PDE based Continuum Diffusion Simulation

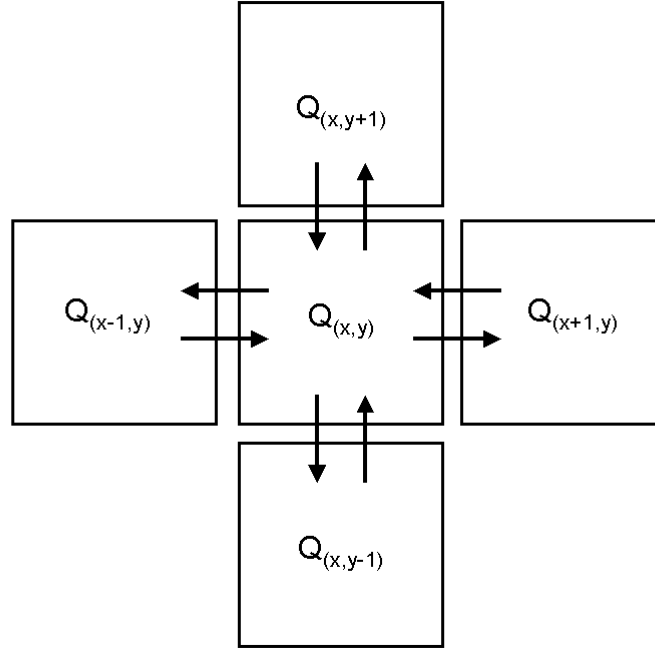


Figure 3.5: The discretization in space of the flows from one region into another is graphically displayed here.  $Q_{(x,y)}$  is the cell of interest and the four 2-D neighbors show flows into and out of this cell. this is the basis of the 2-D diffusion simulation.

Finite Difference Method implemented in the Differential Equation solver Berkeley Madonna 8.0.1 (Macey and Oster, University of California, Berkeley) and visualized using MATLAB (Mathworks Inc., USA). An initial approach looked at diffusion in 1-D with respect to the bleach area. The discretization over the single spatial dimension was done by dividing the space into equally sized compartments and effectively treating them as a series of compartments with connectivity depending on position on the X-axis. The 2-D model discretizes the entire nuclear space as defined by the signal intensity into regular squares. Initialization is done with the first postbleach image, so in effect the bleaching step is not simulated. The model assumes effective diffusion and the flux rate ( $k_{diff}$ ) to and from each compartment is compared to the chromatin densities. The comparison is then made between a single flux rate for every compartment, or multiple flux rates.



# Chapter 4

## Results

“Certainly. If I achieved results with an undescribed program, they would be worth nothing. Who could confirm my results, lacking an equivalent computer program?”

-Isaac Asimov in *Fantastic Voyage II - Destination Brain*

Various approaches have been used in this work to probe the architecture of inter chromatin space in the nucleus. An initial approach was to analyse the motion of discrete vimentin nuclear accumulation, ‘Vimentin Nuclear Bodies’ (VNBs). Based on the findings of heterogeneity in motion, I programmed a Monte Carlo diffusion simulation that allowed me to examine the exact of the deviations from ideal behaviour of the VNBs. Based on the findings I designed and carried out experiments to study the effect of chromatin density on diffusion in the nucleus. The experimental analysis and simulation in 1-D and 2-D provides insights into the extent to which chromatin density affects mobility in the nucleus. I then proceeded to investigate how nuclear bodies maintain their structure, and are yet dynamic to respond to changes in the nucleus, considering Topoisomerase II $\beta$  as a model system. I visualized fluorescence images of the distribution of the molecule in 3-D between the nucleoplasm and nucleolus under varied situations and using a compartment model predicted its distribution kinetics in cell division.

## **4.1 Mobility of VNBs**

Xenopus GFP-NLS-vimentin was imaged in vivo in cell nuclei of SW13 cells by three-dimensional time-lapse confocal laser-scanning microscopy by Michaela Reichenzeller, as part of a collaboration. The distribution of the molecule at 37°C is dot-like and discrete, as been reported earlier (38). I visualized this distribution in 3-D for a single time point using iso-surface rendering (Figure 4.1), giving a qualitative idea of the morphology of the dots. Visual inspection indicates that the dots are slightly elongated in the Z-direction and that the distribution in the Z-direction is restricted as compared to the X- and Y-directions. This is presumed to be a property of the SW13 cells and the culture method of using a flat, 2-D culture plate (see Section 3.2.1).

### **4.1.1 VNBs show Unimodal Velocity and Size Distribution**

GFP-tagged vimentin forms discrete bodies, VNBs. Live microscopy of these bodies shows that they move constantly. The most obvious assumption about this motion is that it is due to random thermal noise and dependent on the temperature. To examine this, I analysed 2-D maximum intensity projections of the images (Figure 4.2a).

The typical movement is illustrated for two neighbouring VNBs (Figure 4.2b). The movement of the particles appears on visual inspection to be a random walk. To test this visually derived assumption more rigorously, I segmented and tracked the bodies and projected the centre of masses of the selected bodies in a 2D projection

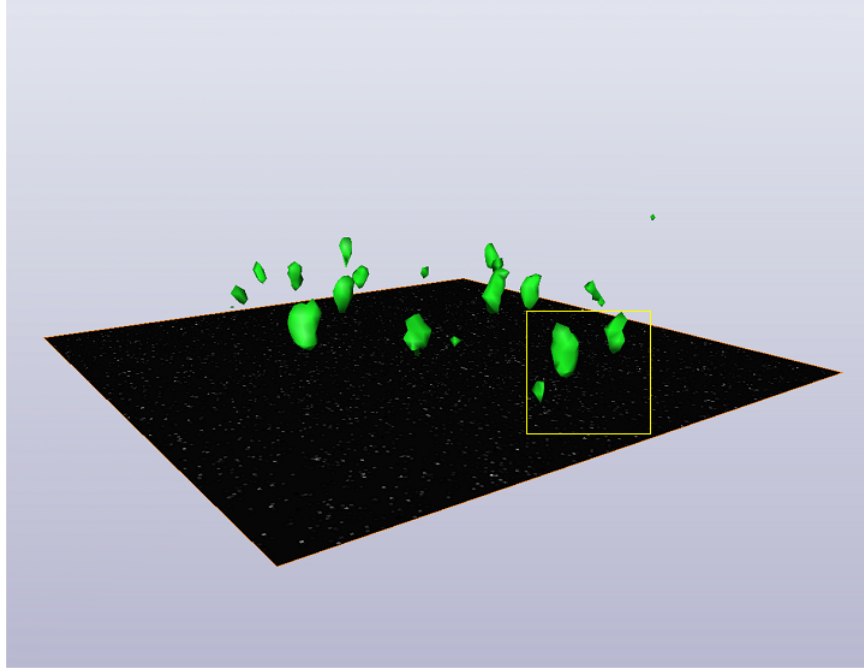


Figure 4.1: *The 3-d reconstruction of a typical data-set shows the vimentin particles distributed over the area of the nucleus with little visible variation in their z-position, and in a shape akin to cylinders, slightly elongated in the vertical direction.*

over time (Fig 4.2c). This plot still appears to show the characteristic jumps in apparently random directions, indicating that the neighbouring particles move by a random walk. But it could be as well interpreted to be thermal motion within some form of restricting boundary. With the plot of changes in inter-particle distances and velocity for each particle (Fig 4.2c) it shows random fluctuations.

To quantitatively test whether the particles are undergoing free diffusion or whether they are restricted to a corral, I analysed the motion of VNBs in 11 cell nuclei by measuring the frequency distribution of velocities (Figure 4.3a) and radii (Fig 4.2b). Velocities of the particles varies from  $0.015$  to  $0.06 \mu\text{m/s}$  with a single mode ( $\sim 0.025 \mu\text{m/s}$ ) (Fig 4.3a). This distribution is similar to the distribution of radii (Figure 4.3b) with a mode  $\sim 0.3 \mu\text{m}$  (mean  $\sim 0.3 \mu\text{m}$ ). The pair-wise diffusion constant was estimated to be between  $1.5 \times 10^{-4}$  and  $45 \times 10^{-4} \mu^2/\text{s}$  with a mean of  $8 \times 10^{-4} \mu^2/\text{s}$  (Figure 4.3c).

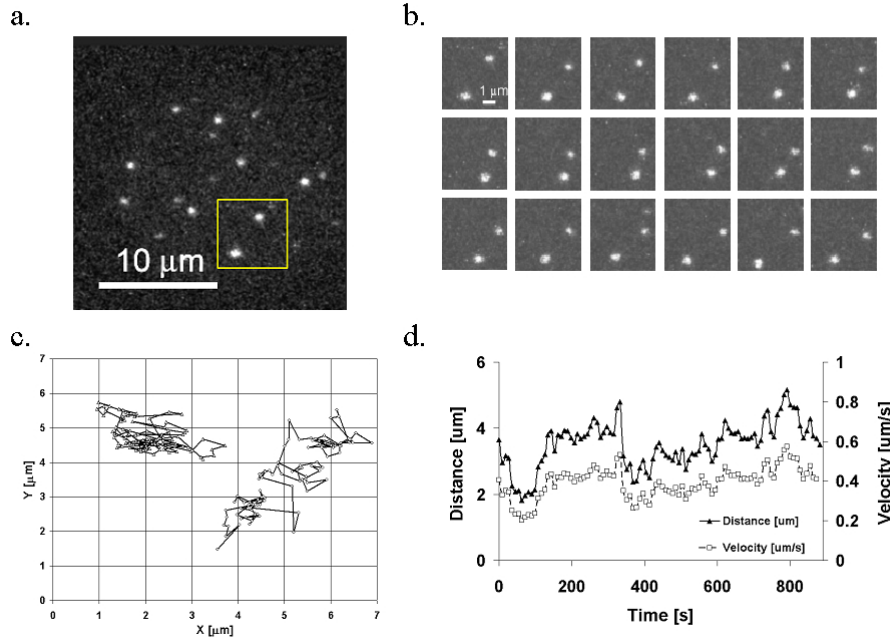


Figure 4.2: In interphase nuclei of SW13 cells, GFP-NLS vimentin accumulations were observed to be considerably mobile. A 2-D maximum intensity projection of one sample nucleus is shown as a grey value confocal microscopy image with contrast enhancement, showing the typical appearance of 20 VNBs as discrete spots in the nucleus (a). The two selected VNBs boxed in (a) appear to move randomly (b). Tracking the centres of mass of the two particles projected in 2-D illustrates the random nature of the motion of the selected VNBs. The plot suggests that their movement is random (c). The distance between the two particles and the velocities plotted over time to quantitatively describe their motion (d) do not indicate any obvious pattern.

### 4.1.2 Dynamics of VNBs corresponds to a passive motion model

The question whether metabolic energy influences VNB mobility was approached by depletion of ATP with Na-Azide. No significant change in velocity was observed, indicating that metabolic energy does not influence VNB mobility (Fig 4.3d). The variance between velocities under the different conditions is well within the standard deviation, indicating that the dynamics of VNBs can be well explained by a passive motion model.

### 4.1.3 Effective Viscosity and Diffusion Models

Ideally diffusion in a liquid is described by the Stoke-Einstein's relation. According to it, given a constant viscosity, the diffusion coefficient is determined by the particle size (Equations 3.17 and 3.18). When different effective nuclear viscosities were fit

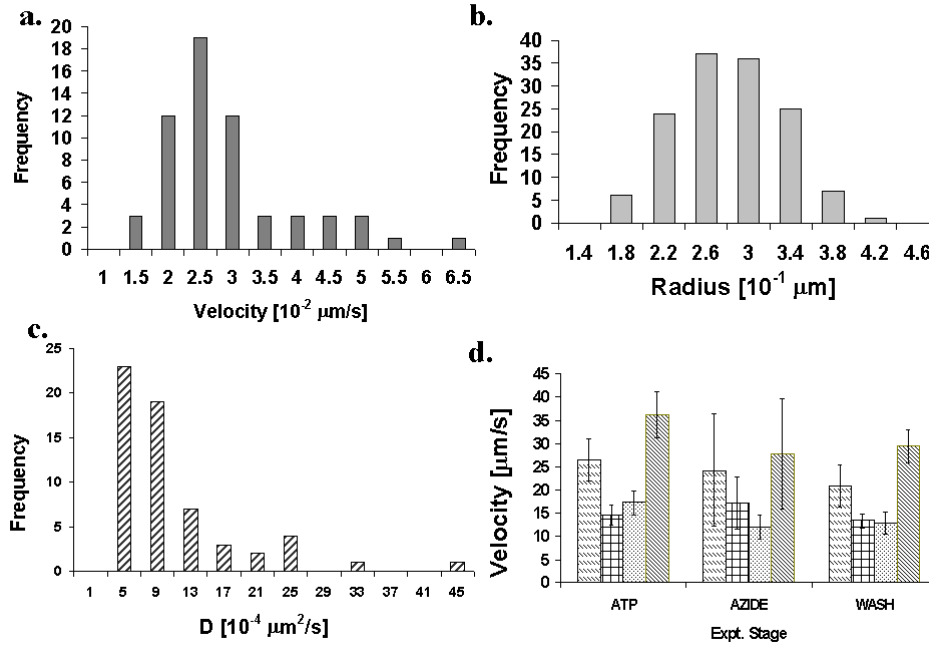


Figure 4.3: Frequency distributions of various motility related parameters of VNBs like the velocity (a) and the radius (b) of particles are unimodal. The distribution of pair-wise diffusion constants is also unimodal, but shifted to the left (c). Metabolic energy depletion does not result in any significant change of mobility when comparing average velocities of VNBs in four cells, before (ATP) and after Sodium Azide treatment (azide) and after washing (wash). Different patterns indicate data from individual cells.

to the increasing size of the bodies it became apparent that different viscosities appeared to be appropriate for different regions of the profile, as seen in the plot of the frequency distribution of  $D$  with changing particle radii as compared to the theoretical curves (Figure 4.4). A value of  $\eta = 9\text{Poise}$  appeared to fit well with the higher end of radii while an order of magnitude higher  $\eta = 31$  appeared to fit the initial range of the data. When I plotted all the values of  $D$  against radius of particles, the profile and searched for the best global fit to Stoke-Einstein's (SE) relation (blue) by adjusting the effective viscosity  $\eta$  (Equation 3.17 and Figure 4.5). The effective nuclear viscosity was estimated as  $\eta = 17\text{Poise}$  (Figure 4.3d). This value is in the same order of magnitude as the previously established value for effective nuclear viscosity (163, 164).

The increase in variance with increasing particle size is orders of magnitude higher than expected from a systematic error. To account for the error an empirical model of so-called critical diffusion was tested, where particles of a critical size diffuse faster than predicted by the Stoke-Einstein model. The model adapted from the Stokes Einstein model (Equations 3.17 and 3.18) was modified as follows:

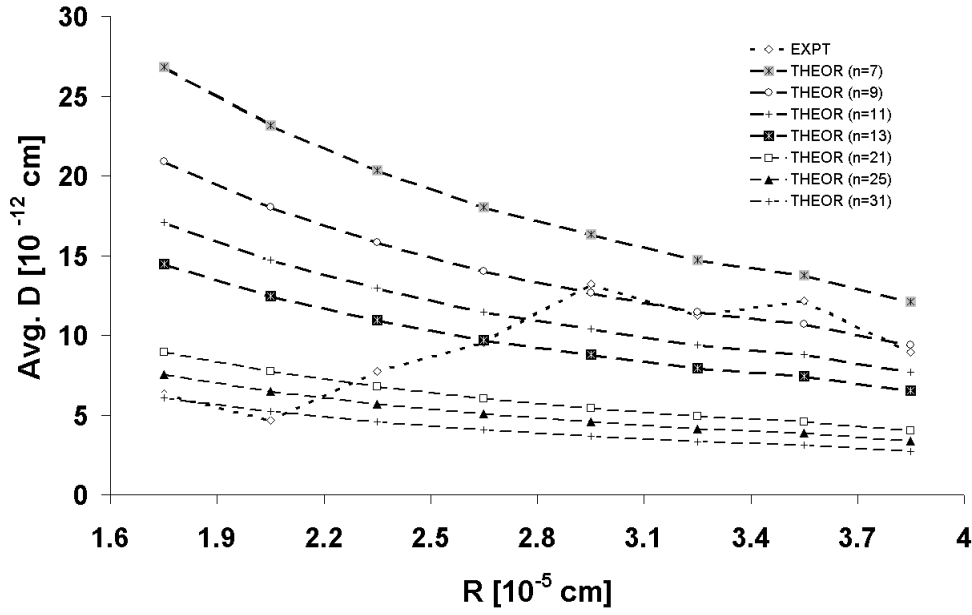


Figure 4.4: The comparison of  $D$  values obtained with changing VNB sizes was compared to profiles obtained for different values of the effective viscosity ( $\eta$ ) using the Stokes-Einstein relation. It would appear that the low viscosity values of  $\eta = 9$  Poise fit well with the right half of the data and an order of magnitude higher values of  $\eta = 31$  would agree better with the initial half of the data. This might indicate that different sizes of particles might ‘sense’ obstacles differently.

$$D = \frac{k_B T}{f} + \exp\left[\frac{-(a-\mu)^2}{\sigma^2 2\pi}\right] \quad (4.1)$$

where  $\mu$  is the critical radius and  $\sigma$  the standard deviation. This extra Gaussian terms signifies a possible size specific sieving, relating to the channel-like network model of the interchromosomal domain (ICD) compartment.

#### 4.1.4 Rejecting the Critical Diffusion Model

The critical diffusion (red) and the SE model (blue) (Figure 4.5) were compared to the data with an F-max test to compare the variances between data and the two models. Although the critical diffusion model reduces the variance to data, the difference is not significant ( $P=0.05$ ) to the SE model. It cannot be excluded that the observed difference is due to the randomness of VNB movement.

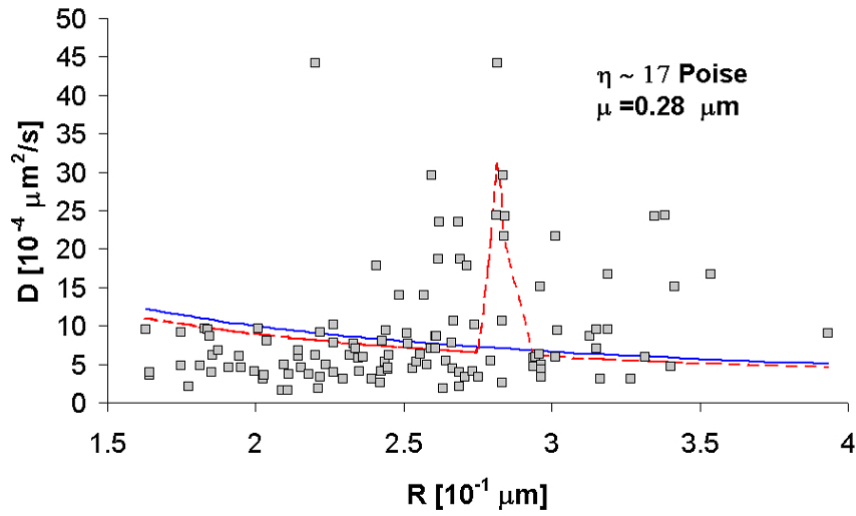
### 4.1.5 Anomalous Diffusion of VNBs

The model of motion for VNBs in the nucleus appears to be a form of diffusion with a high effective viscosity. However on examining the MSD of individual pairs of particle, I observed at least three different regimes of diffusion. Some particles undergo free diffusion with diffusion constants of  $1.75 \times 10^{-4} \mu\text{m}^2/\text{s}$  (Figure 4.6a), a second class of VNBs shows restricted motion with a restriction radius of 0.54  $\mu\text{m}$  (Fig 4.6b), and a third class of VNBs even undergoes vectorial diffusion with an additional velocity of  $2.8 \times 10^{-3} \mu\text{m}/\text{s}$  (Figure 4.6c). When estimating the average of all mean square displacements of all VNBs in all cells, the log-log plot of  $\text{MSD}/\text{Dt}$  against  $\text{Dt}$  showed a negative slope for small  $\text{Dt}$ 's and a curve parallel to the x-axis for larger  $\text{Dt}$ 's, similar to the theoretical graph according to the Stokes-Einstein model of free diffusion (Figure 4.6d). The anomalous diffusion exponent ( $\alpha$ ) was fitted to the linear part and found to be 2.47. This value is a function of the obstacle concentration. The value is in the same range as that found for Cajal Bodies (165) indicating that VNBs encounter similar hindrances to their movement as Cajal bodies.

### 4.1.6 Fusion of Bodies is an Additive Process

As the particles move they also occasionally fuse to form larger particles. These fusion events were examined in 3-D visual reconstructions over time (Figure 4.7a), since understanding this might shed light on the nature of the environment of the VNBs, the interchromosomal space. For ten particles, considered pair wise ( $n = 5$ ) from different cells, volume and intensity measurements show that the fused body has an average volume corresponding to the sum of the volumes of the individual bodies before fusion (Figure 4.7b). The same additive effect was seen for fluorescence intensities, implying that the mass of the protein in the post-fusion body is the sum of the pre-fusion bodies. That this effect is reproducible is demonstrated in Figure 4.8).

a.



b.

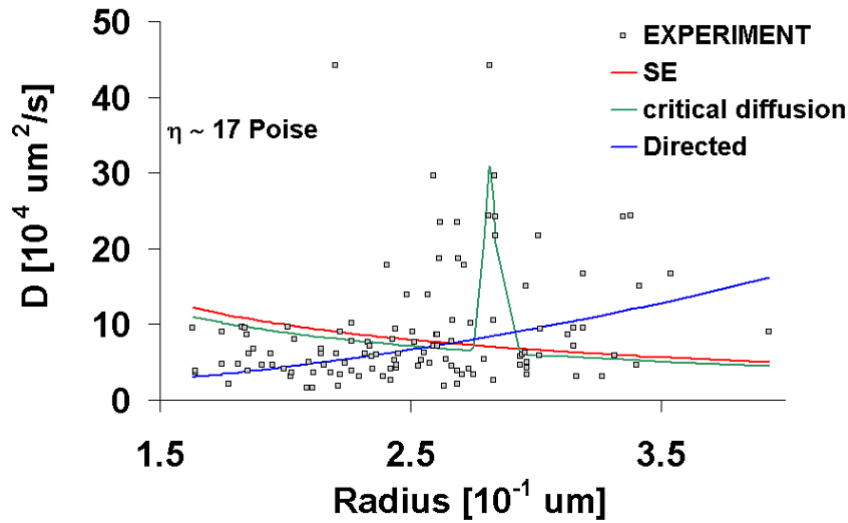


Figure 4.5: The average diffusion constant ( $D$ ) was measured with respect to the radii ( $R$ ) of VNBs. a. These estimates were compared to the predicted values from the Stokes Einstein (SE) model and a SE-critical diffusion model including an additional Gaussian term with a critical radius ( $m$ ). The viscosity parameter obtained from the model fit is  $\eta=17$  Poise, indicating a very high density of obstacles and a critical radius of  $\mu=0.28$  mm. b. Alternatively in addition to the SE and SE-critical diffusion model a model of directed diffusion was also fitted with no significant improvement in the fit.



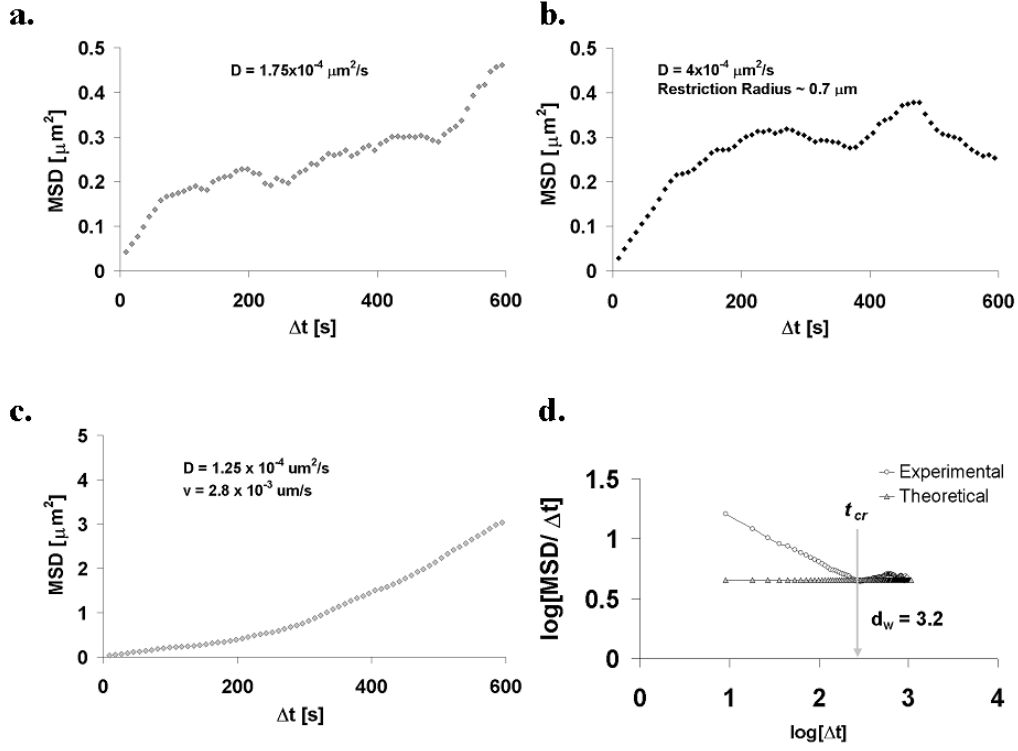


Figure 4.6: The pair-wise mean square displacement (MSD) of VNBs show three different modes of diffusion- simple linear diffusion ( $D = 1.75 \times 10^{-4} \mu\text{m}^2/\text{s}$ ) (a), restricted diffusion ( $D = 4 \times 10^{-4} \mu\text{m}^2/\text{s}$  and restriction radius =  $0.7 \mu\text{m}$ ) (b) and diffusion ( $D = 1.25 \times 10^{-4} \mu\text{m}^2/\text{s}$ ) with directed flow (velocity =  $2.8 \times 10^{-3} \mu\text{m}/\text{s}$ ) (c). The log-log plot of  $\text{MSD}/Dt$  against  $Dt$  shows the anomalous nature of the diffusive process. In the initial stage the slope of the curve is negative in experimental measurements in contrast to the linear profile using a theoretical diffusion constant for a particle of average size and  $\eta=0.01$  (viscosity). (d). Over longer time periods the experimental values also show a horizontal profile. The anomaly exponent ( $d_w$ ) (see methods) from the descending segment of the curve relates to the extent of anomaly in the movement.  $t_{cr}$  is the crossover time when the motion changes from anomalous to normal diffusion.

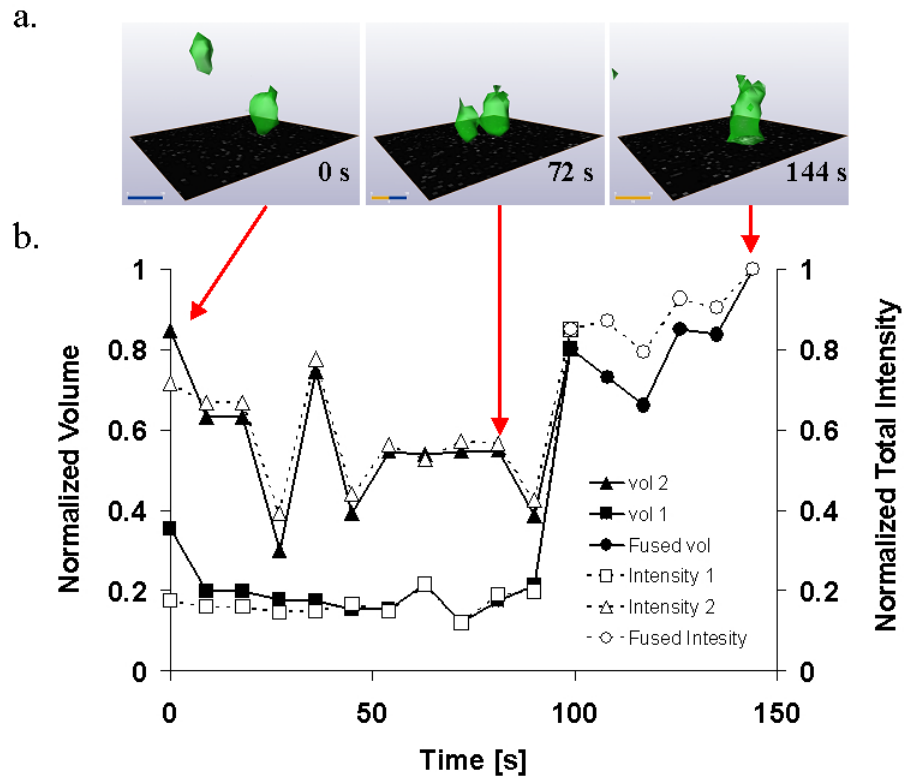


Figure 4.7: A 4-D time series reconstruction of a fusion event of VNBs shows snapshots at 0s, 72s and 144s (a). The volume curves show that total volume is conserved after fusion since the volume of the newly formed VNB averaged over time before fusion is the sum of the average volumes for the bodies that participate in fusion (b). The arrows indicate the corresponding time points for the visualizations. Volume and total intensity were normalized with respect to the maximum value.

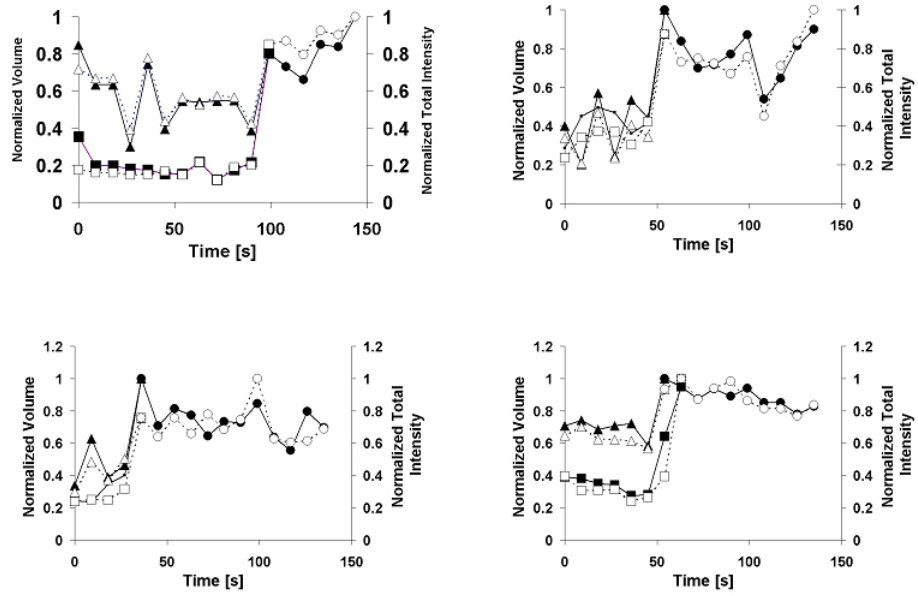


Figure 4.8: The volume and intensity plots of fusion event of VNBs show average values for both after fusion to be the arithmetic sum of the average before fusion. Volume and total intensity were normalized with respect to the maximum value for all four data sets, obtained from different cell nuclei.

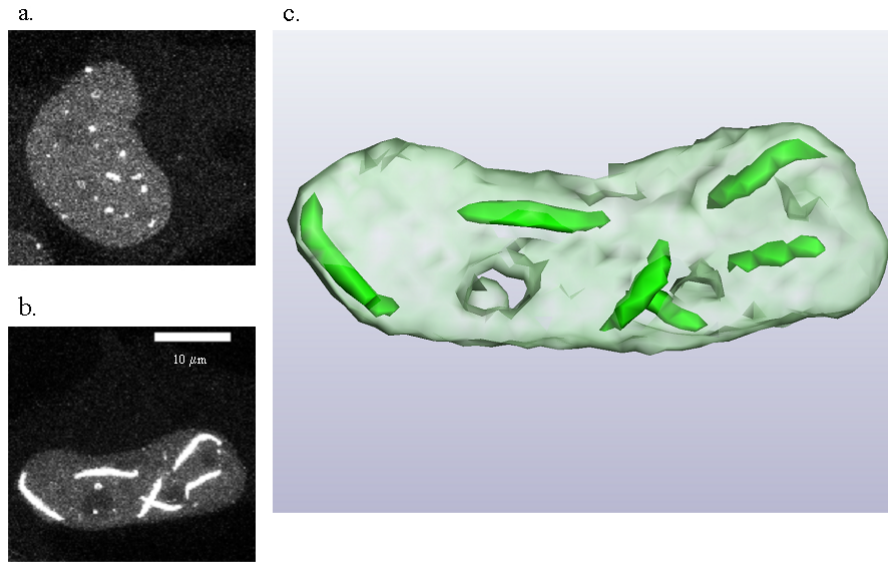


Figure 4.9: The *Xenopus* derived temperature sensitive GFP-tagged NLS-vimentin co-transfected with untagged NLS-vimentin has been shown to form discrete ‘dot-like’ structures at 37°C (a) and when shifted to the permissive temperature of 28°C elongate to form filaments (b). These filaments appear to be restricted in space and can be visualized in 3-D (c) to form discrete tube-like structures.

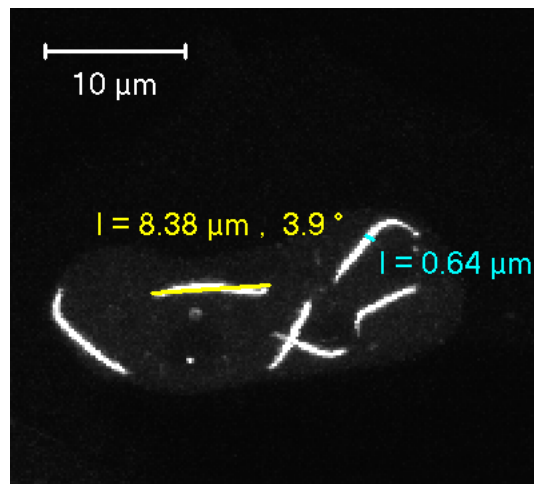


Figure 4.10: The sizes of the potential channels inside the cell nucleus were inferred from measurements made on the microscopy images of polymerized vimentin. The length and width of these fibres as measured are shown and these parameters were used for determining the size of a restricting channel.

## 4.2 Monte Carlo Simulation of the Interphase ICD space

In order to better understand the mobility and the anomalies that turned up in the diffusional behaviour of the VNBs, I formulated a model of the diffusion of particles in such a tube like network and simulated its diffusion based on the Ermak and McCammon algorithm as described in the methods section (3.5). The polymerization of GFP-NLS-vimentin (Figure 4.9) was used as a basis for simulating the channel like network, especially in order to derive the channel diameter (Figure 4.10). In the simulation, the nucleus is represented as a rigid sphere and the nuclear bodies as idealized spheres. Their movement is governed by random diffusion, dependent on thermal energy and viscosity of the medium. I tested the effect of various restrictions on the movement of these bodies and attempted to explain the ‘critical-diffusion’ as described in Section 4.1.

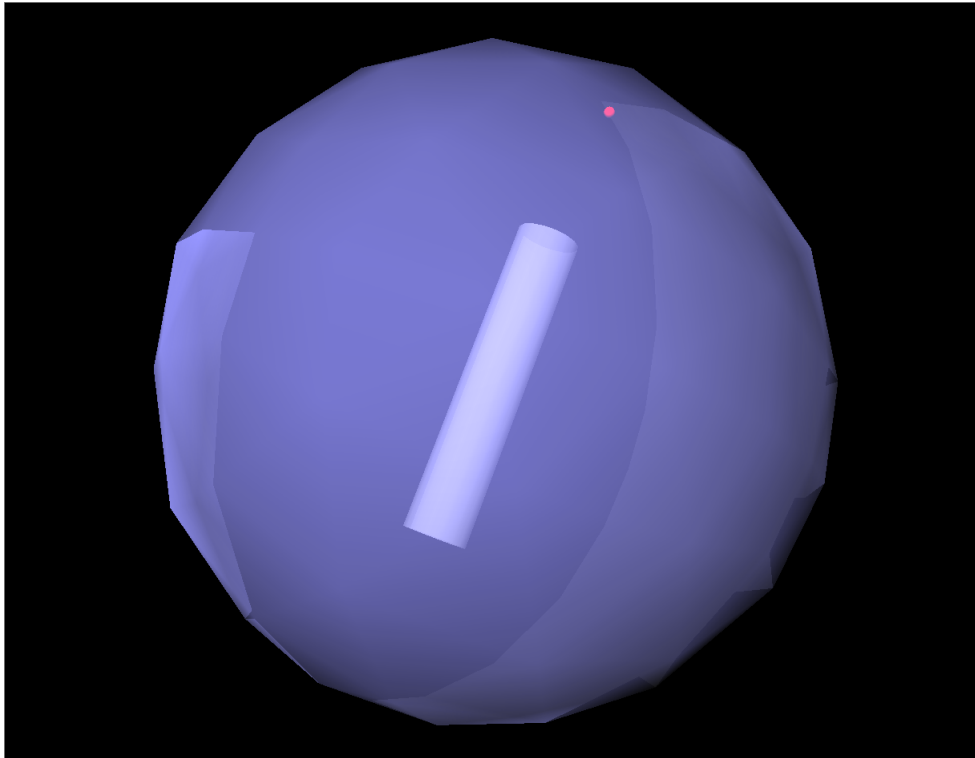


Figure 4.11: *The diffusion of particles of the average size of the vimentin bodies was simulated in a Monte Carlo diffusion simulation. The outer sphere in the figure represents the theoretical cell boundary. The cylinder represents one channel like structure. The red sphere is the diffusing particle. The cell boundary as well as the channel provide obstructions to the mobility of the particle.*

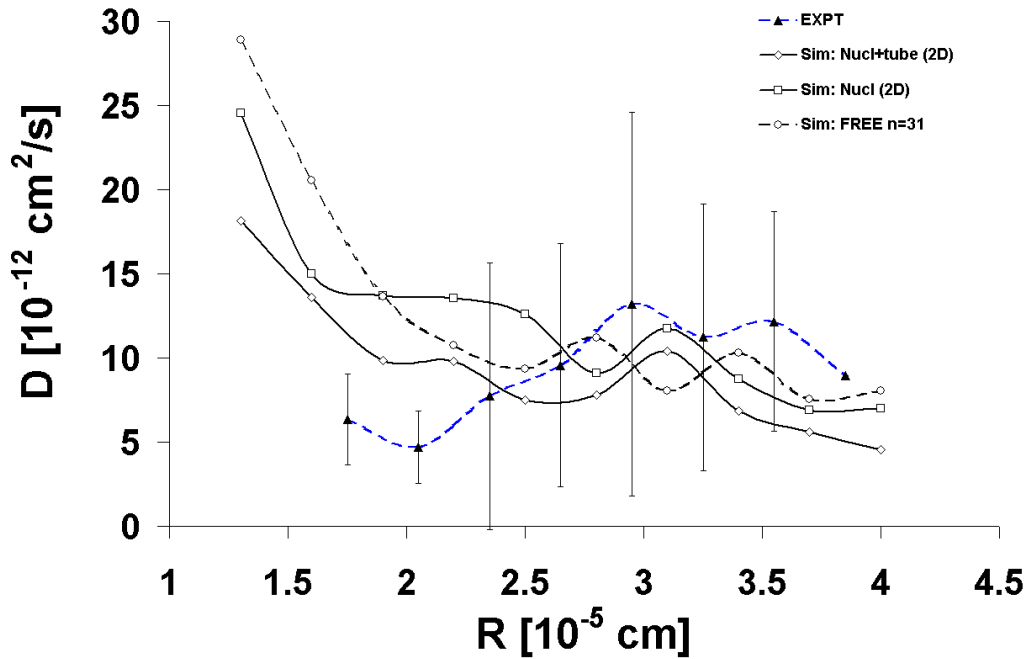


Figure 4.12: Particles of different sizes in the range measured were simulated to diffuse under three different regimes- free, restricted to a tube, and restricted to a cylinder. All three were restricted to a sphere, of the typical radius of a mamalian cell as seen in Figure 4.11. The data obtained by analysing the simulation was then compared to the experimentally observed change in diffusion constants with particle radius to see if the variability seen in a certain range might be explained by the nature of obstruction.

#### 4.2.1 Effect of Channel Obstacles

As an initial approach to understanding the deviation of the experimental data of VNB diffusion from the Stokes-Einstein model of diffusion, I imposed simple geometric restrictions on the mobility of the bodies. The channel like structure observed in by experiments with polymerizing *Xenopus* nuclear vimentin motivated the choice of a cylinder as an obstruction (Figure 4.9). Since the effective nuclear viscosity is the sum of fluid phase viscosity and slowed diffusion due to collision with and restriction by obstacles, I assumed that an obstacle might actually explain some of the behaviour in the plots of  $D$  against radius (Figure 4.4). Sizes of the particles were iterated over the same range as in the experimentally measured data, with free diffusion, diffusion within a hypothetical nucleus and with a nucleus with a single channel (Figure 4.11). The parameters for the dimensions of the channel of radius and length were similar to the sizes of vimentin filaments measured experimentally (Figure 4.10). The diffusion constant was averaged over simulation runs of  $10^4$  time steps. The plot shows that for all three kinds of motion, the variation

in diffusion constant with the three scenarios is makes them indistinguishable from one another 4.12.

### 4.3 Effect of Chromatin Density on Diffusion of NLS-YFP in the Nucleus

Another aspect of the results from the studies with vimentin mobility is the issue of anomalous diffusion. I attempted to concentrate my attention on restricted diffusion and unravel its causes. As a first attempt to this, I conducted FRAP experiments with an NLS-YFP construct as described in the methods. I performed the mobility studies in SW13 cells.

#### 4.3.1 FRAP Analysis

In the model of diffusion assumed, the density of chromatin would affect the mobility of the molecules. So I performed FRAP measurements with the NLS-YFP probe in NRK cells stably expressing a marker for chromatin, a histone 2B fused to CFP. The regions of bleaching were selected in different parts of the nucleus, typically 3-4 different regions. The result of this is shown in Figure 4.13. The cells imaged c4 (a), c5 (b) and c6 (c) show rapid recovery of signal with recovery achieved within 10 s. What is also noticeable is that the recovery is not complete, i.e. the signal does not return to the initial value or even close to it.

I examined the results of this in a two step approach. As an initial step, I quantified the mobility in terms of half time ( $t_{1/2}$ ), i.e. the time taken from the bleach pulse for the recovery to reach half its post-bleach maximum. This quantification shows that the  $t_{1/2}$  has a mean value ( $n = 11$ ) of 4.1 s. Diffusion appears to be rapid. The mean  $t_{1/2}$  however has a standard deviation of 5.8 which is very large. I then examined the individual  $t_{1/2}$  values in order to test the assumption that the differences in actual values were due to chromatin densities. The plot (Figure 4.14) suggests a linear relationship between chromatin density and the mobility of the NLS-YFP.

A closer look at this revealed that the relationship is linear in cases such as shown in Figure 4.15. Here for a given cell its different sub-regions appear to show a linear distribution of  $t_{1/2}$  times as compared to chromatin density (normalized to the maximum value). In the case of cell 5 this is very strong (with the regression coefficient  $R^2=0.99$ ) and in the case of cell 6 the case is very weak.

One of the most prominent effects observed in nls-YFP recovery (Figure 4.13) is that a large proportion of the signal shows no recovery at all. This can also be

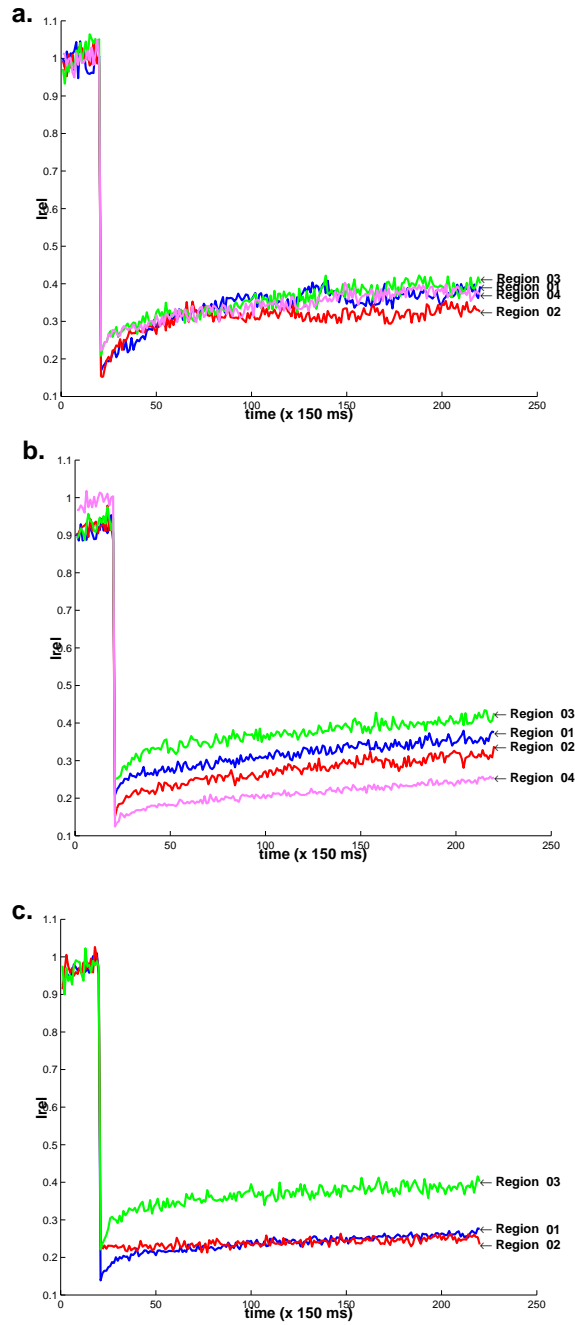


Figure 4.13: The normalized intensity of the regions after FRAP. a, b and c are three different cells (c4, c5, c6) used in the experiment and the different regions are the regions in which bleaching was conducted.

quantified and shows that the mean mobile fraction ( $R$ ) of the NLS-YFP in these cells is only 0.176 (Table 4.1), i.e. 82% of the molecules remain bound.

Thus  $\approx 17.6\%$  of the molecules are mobile. The cause of this mobility has been hinted to by observations of the YFP coating the chromosomes in division.



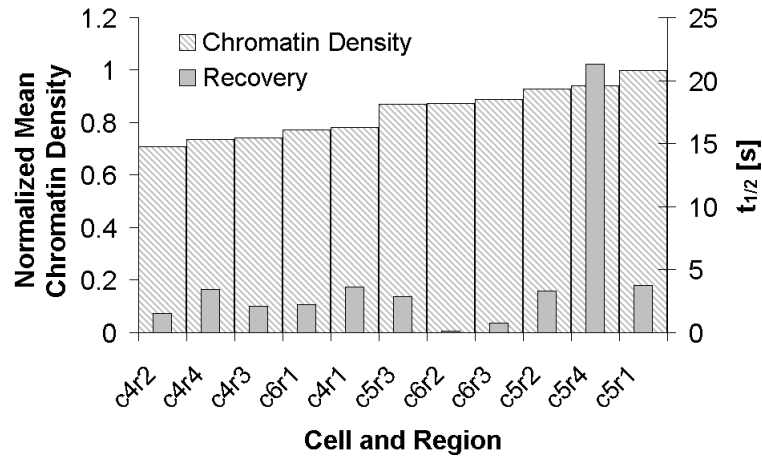


Figure 4.14: The bar chart shows the  $t_{1/2}$  of FRAP experiments in different regions of cells, superimposed on the corresponding chromatin density arranged in ascending order. The chromatin density is expressed as intensity per pixel normalized with the maximum value. The associated  $t_{1/2}$  is plotted at the same spot.

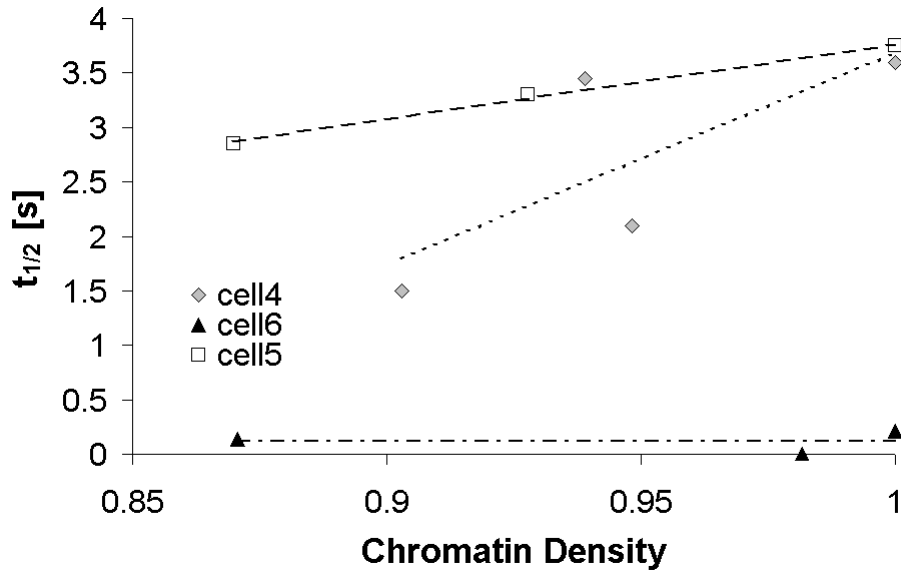


Figure 4.15: The otherwise high scatter of  $t_{1/2}$  values with chromatin density might be explained by the fact that the relative state of chromatin regions in a given cell. For cell 4 the distribution shows a linear fit to  $y = 19.525x - 15.839$  ( $R^2 = 0.5785$ ), for cell 5 to  $y = 6.8929x - 3.1281$  ( $R^2 = 0.9959$ ), and cell 6 to  $y = -0.0385x + 0.1544$  ( $R^2 = 0.0006$ ).

### 4.3.2 Non-Ideal Recovery

A typical quantification of a FRAP experiment is extracting a diffusion constant. The method utilized to quantify a FRAP experiment is to fit the recovery profile in the bleached region to the solution to the diffusion equation, assuming that the

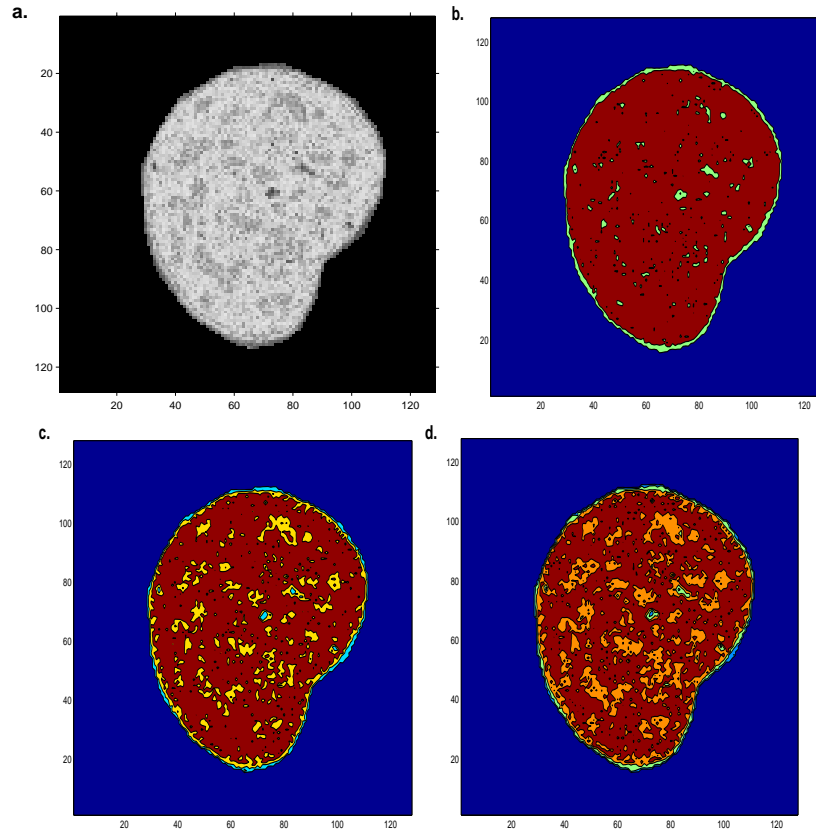


Figure 4.16: The nuclear chromatin has been visualized in the cells in which YFP mobility was measured. Here one such cell is displayed as (a) a grey value image, and sequentially contours were detected (b-d) in which 2, 3 and 4 different iso-intensities were extracted and their borders joined. These images give a picture of an inhomogeneous distribution of chromatin and a possible reason for inhomogeneous diffusion.

Table 4.1: The extent of mobility of a molecular species in a FRAP experiment can be expressed as the mobile fraction. Here mean mobile and immobile fractions of the NLS-YFP diffusion in the nucleus averaged over three cells and 3-4 sub-regions each ( $n=11$ ). The data shows the molecule to be highly immobile and the data to have .

	Mean	Standard Deviation	Percent
<b>Mobile Fraction</b>	0.176	0.066	17.6%
<b>Immobile Fraction</b>	0.823	0.066	82.4%
<b>after <math>\sim 30</math> s</b>			

bleaching is sharp, and the profile of recovery is Gaussian in space. Also it assumed that the boundary of the medium is infinite (121). To confirm that my experimental data be treated similarly, I analysed the intensity profile of the signal in the bleached region immediately after bleaching, along both X- and Y-axes (Figure 4.17). In

neither direction did the analysis suggest that a Gaussian profile is what is being observed.

### 4.3.3 Simulation of FRAP in 2-D

In order to overcome the issue of being unable to fit the classical homogeneous continuum solution to the Diffusion of the YFP, I considered simulating the diffusion to obtain a fit to the data. What is also apparent from visual inspection of the bleach data is that although the bleach area is spatially restricted, diffusion is obviously so rapid that any attempt to restrict the influence of distant regions on the diffusion in the selected region of interest (ROI) will lead to artefacts. I therefore performed a simulation which is initialized with the pre-bleach image intensities (Figure 4.18a). The model adopted is one of effective diffusion where the mobility is due to diffusion and dependent on the D value- particle size, temperature and viscosity.

The approach to the simulation was to divide the cell into sub-compartments and set the flows dependent on spatial neighbourhood, i.e. flows from one cell are possible into and from a maximum of 4 other cells (Figure 3.5). The result of the simulation is shown in Figure 4.19 where the experimental data (the symbols) is compared to the simulated result. The only optimization done was to fit the flow rate. It would appear that a single flux due to diffusion ( $k_{diff}$ ) value can approximate the diffusion of a small molecule like YFP. Furthermore, the power of the simulation is that it can allow spatially resolved access to data in any of the sub-compartments, as shown in (Figure 6.2).

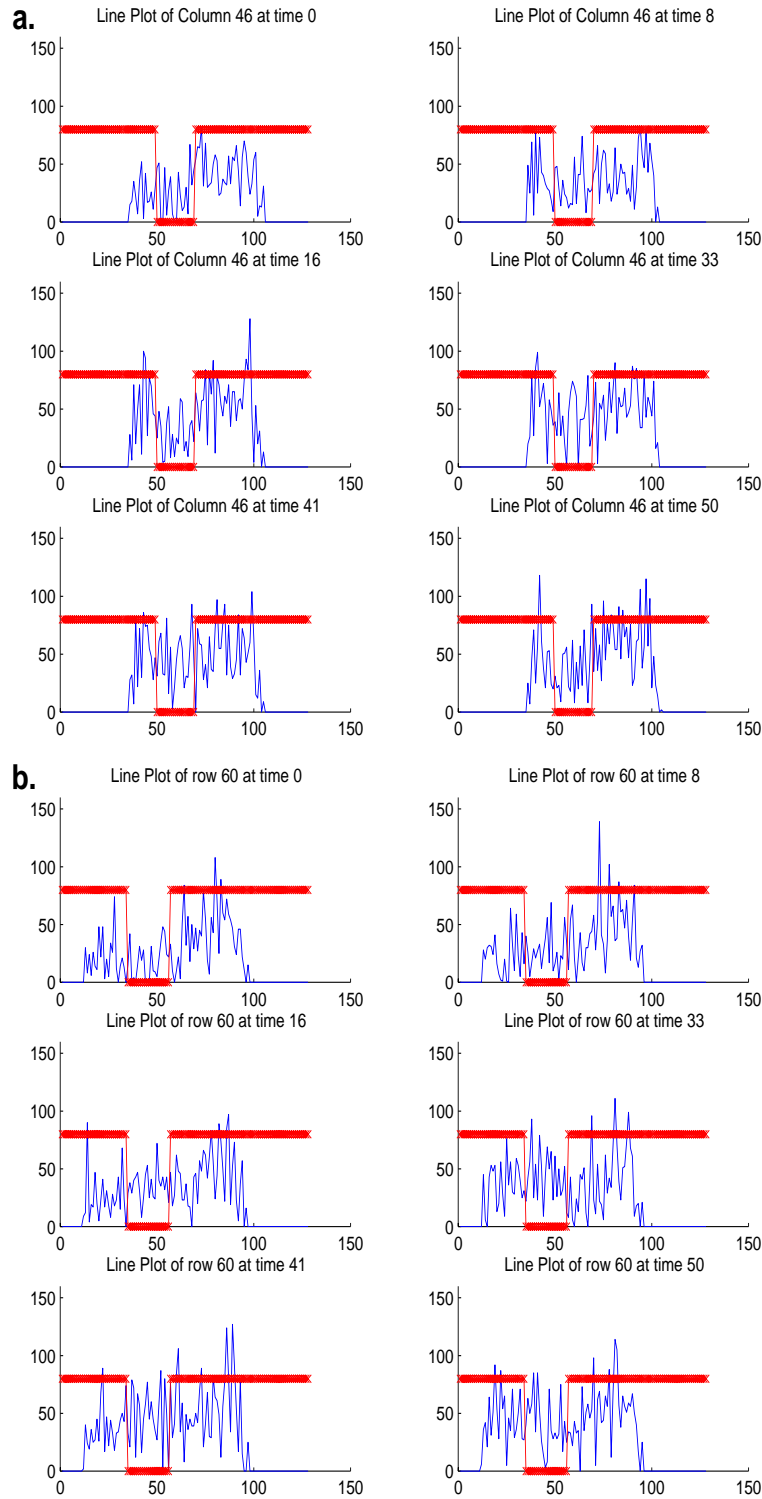


Figure 4.17: The line scan in X- and Y-directions of tow data sets at 6 time points in the postbleach phase is displayed here. The red line indicates the 1-D outline of the bleach area—the drop in the middle is the bleach region. The blue line indicates the signal intensity. As seen here, it is very difficult to imagine a Gaussian function to fit this data. a. The profile for vertical sections through the cell and b. for horizontal profiles.

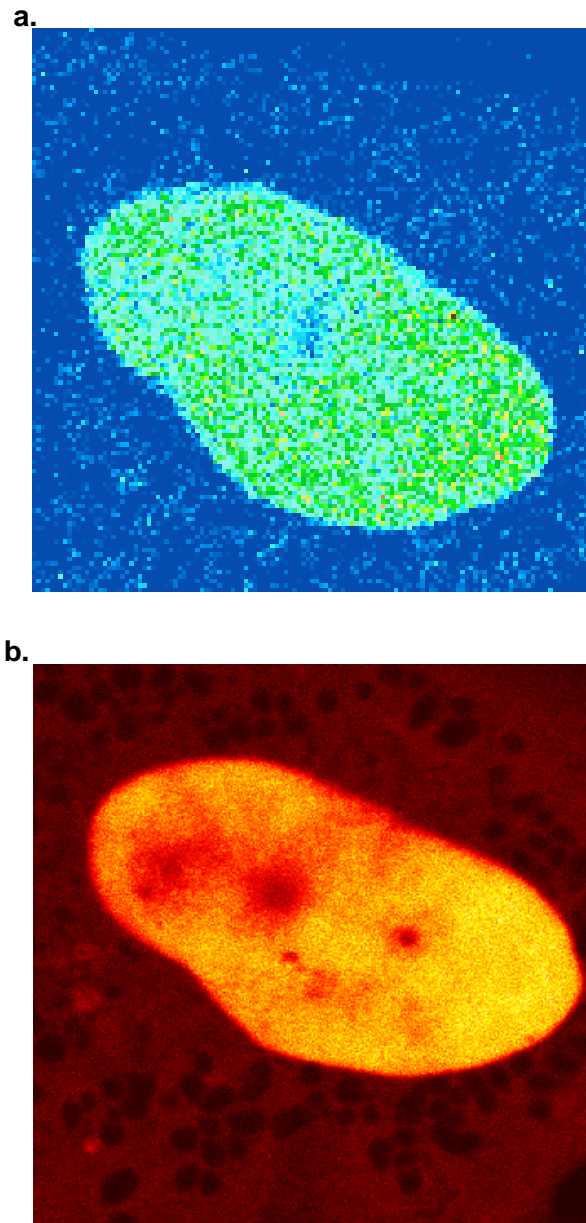


Figure 4.18: *The intensity image before bleaching of NLY-YFP distribution in one of the measured cells (cell 4) is shown (a). This distribution appears uniform. The image of H2B-YFP distribution (b) shows the inhomogeneous distribution of the molecule, which we have considered to be a marker for chromatin density.*

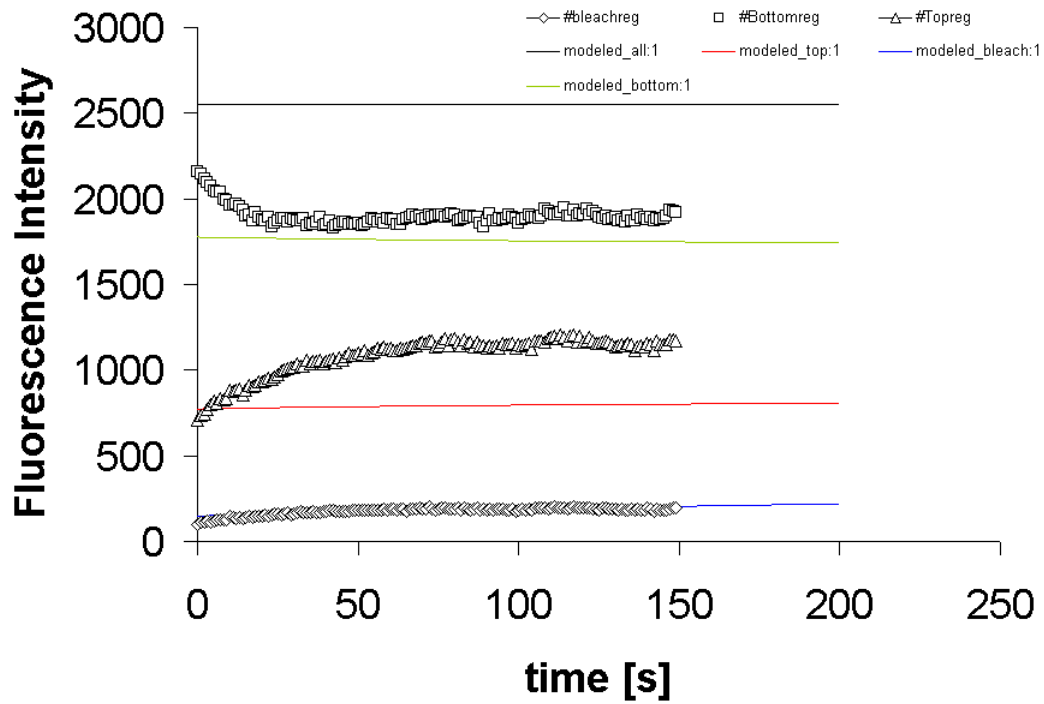


Figure 4.19: The result of a 2D simulation of diffusion is compared to experimental data. continuous lines are the simulated profiles of intensity (black = total, green = bottom cell region, red = top region and blue= bleach region), based on a single optimized  $k_{diff}$ , the flux due to diffusion. The experimental data is displayed as symbols (squares = bottom region, triangles = top region and diamonds = bleach region).

## 4.4 Dynamics of Topoisomerase Localization

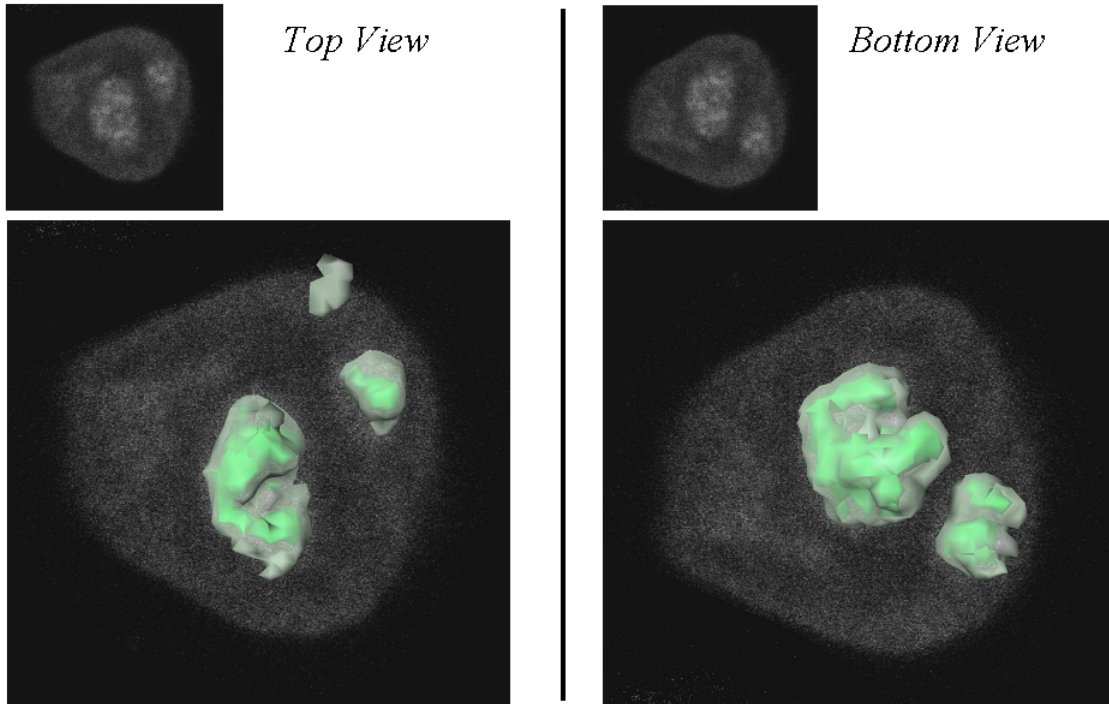


Figure 4.20: The 3-D distribution of the GFP-labelled topoisomerase II alpha (TopoIIa) is examined here in isosurface reconstructions of the protein distribution, superimposed on the original grey value images. The top and bottom views show the concentric distribution of intense signal (dark green) and weaker signal intensity surrounding it (grey), probably the differences between the central dense fibrillary centre (DFC) and peripheral regions of the nucleolus.

Experiments done recently with GFP-tagged Topoisomerase II (TopoII) in mammalian cells have shown it to be mobile and possess two components, bound and mobile (166), contrary to earlier ideas. The molecule also has been long known to be drug sensitive in its distribution, reacting to varied anti-cancer drugs.

### 4.4.1 3-D Visualization of TopoIIb Distribution

I visualized the 3-D distribution of the protein using iso-surface reconstructions as described in the methods section. These allow us for the first time to visualize the molecule in-vivo in 3-D (Figure 4.20). As seen in the figure, there were three clearly identifiable kinds of signal, most likely to be the inner dense fibrillar

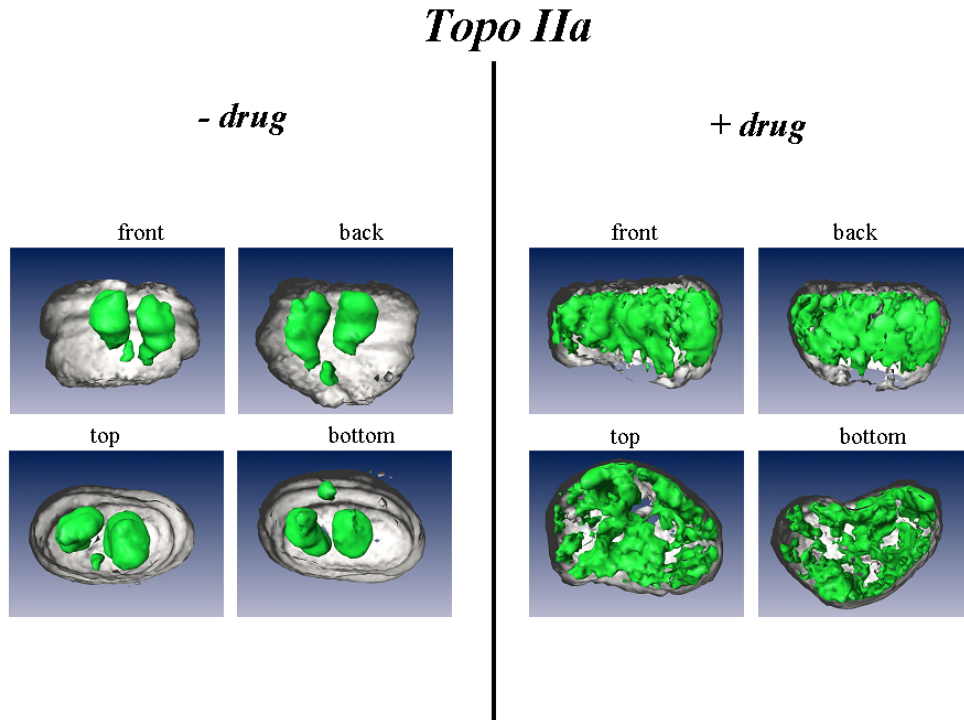


Figure 4.21: *The 3-D distribution of GFP-TopoIIa is disrupted from its familiar pattern of nucleolar concentration to a more nucleoplasmic reticulate distribution, as seen in this panel of the same cell before and after camptothecin treatment, from four perspectives each.*

component (DFC), outer peripheral nucleolar cortex and the nucleoplasmic signal. The visualization in 3-D emphasizes the fact that the signal in the nucleolar cortex, most-likely the granular component (GC), surrounds the central region completely. The changes to this distribution when the cell is treated with camptothecin are drastic and the effect is seen graphically in Figure 4.20 as +drug and -drug. The cells after treatment show an almost reticulate distribution (Figure 4.21). This fits well with the known fact that camptothecin stabilizes the complexing of TopoII to DNA, so the reticulation is probably the fibrous chromatin network.

#### 4.4.2 Model of TopoIIb Distribution

Recent work with FRAP of GFP-TopoIIb has shown the molecule possesses slow (bound) and fast (mobile) fractions, both for the nucleolus and nucleoplasm (166), provided us with a 2-phase model- with a diffusing and binding component each in the nucleoplasm and nucleolus.

Using this information, an initial setting of the 4 compartment model I configured a set of ODEs to represent the distribution of the molecule. The result of the 4 compartment model compared to the 2 compartment model improves the fit



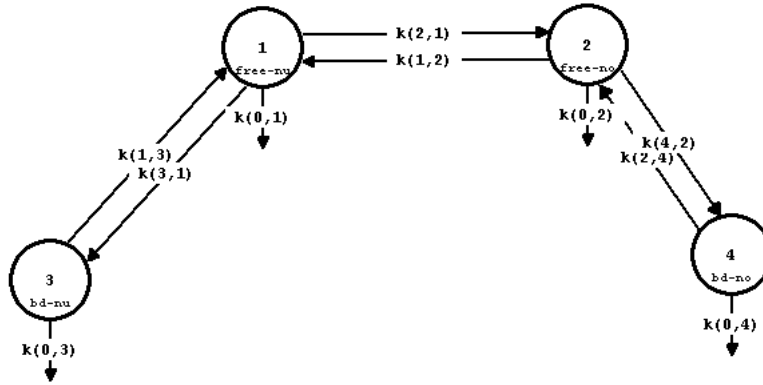


Figure 4.22: The graphic representation of the model of topoisomerase distribution in interphase used to model the recovery of the molecule in FRAP experiments. The compartments, represented by circles are bound (bd-nu) and free (free-bd) nucleoplasmic and bound (bd-no) and free (free-no) nucleolar fractions. The arrows represent flows out of a given compartment.

to FRAP data thus justifying the additional cost in terms of extra parameters, besides also reflecting the mechanisms that govern TopoIIb distribution. The system is open, due to the constant outflow from each compartment. This is representative of photobleaching due to imaging. The four compartments are the four pools that are easily identified, namely the nuclear free and bound pools and the nucleolar free and bound pools.

As an initial step I designed experiments whereby cells with a single nucleolus and stably expressing TopoIIb were measured in FRAP experiments. The FRAP recovery was measured, by collaborators, where alternatively either the nucleolar (Figure 4.23a) or the entire nucleoplasmic signal (Figure 4.23b) was bleached. Using the model a good fit was obtained. The process was repeated for the nucleolus ( $n=3$ ) and nucleoplasm ( $n=2$ ). The flux rates obtained were quantified in molecules per unit time using GFP protein standards.

By inverting the flux rates, and appropriately scaling for volume, I obtained the residence times of the molecules in the various pools. It would appear that the residence per molecule per volume element for free molecules is only an order of magnitude different between the nucleoplasm and nucleolus as shown in Table 4.2. This difference is however  $10^3$  fold in case of the bound fraction (Table 4.2). There must be a marked difference between the medium in which free TopoIIb moves in the nucleolus, consistent with the existent view that the nucleolus is one of the densest structures in a cell (167).

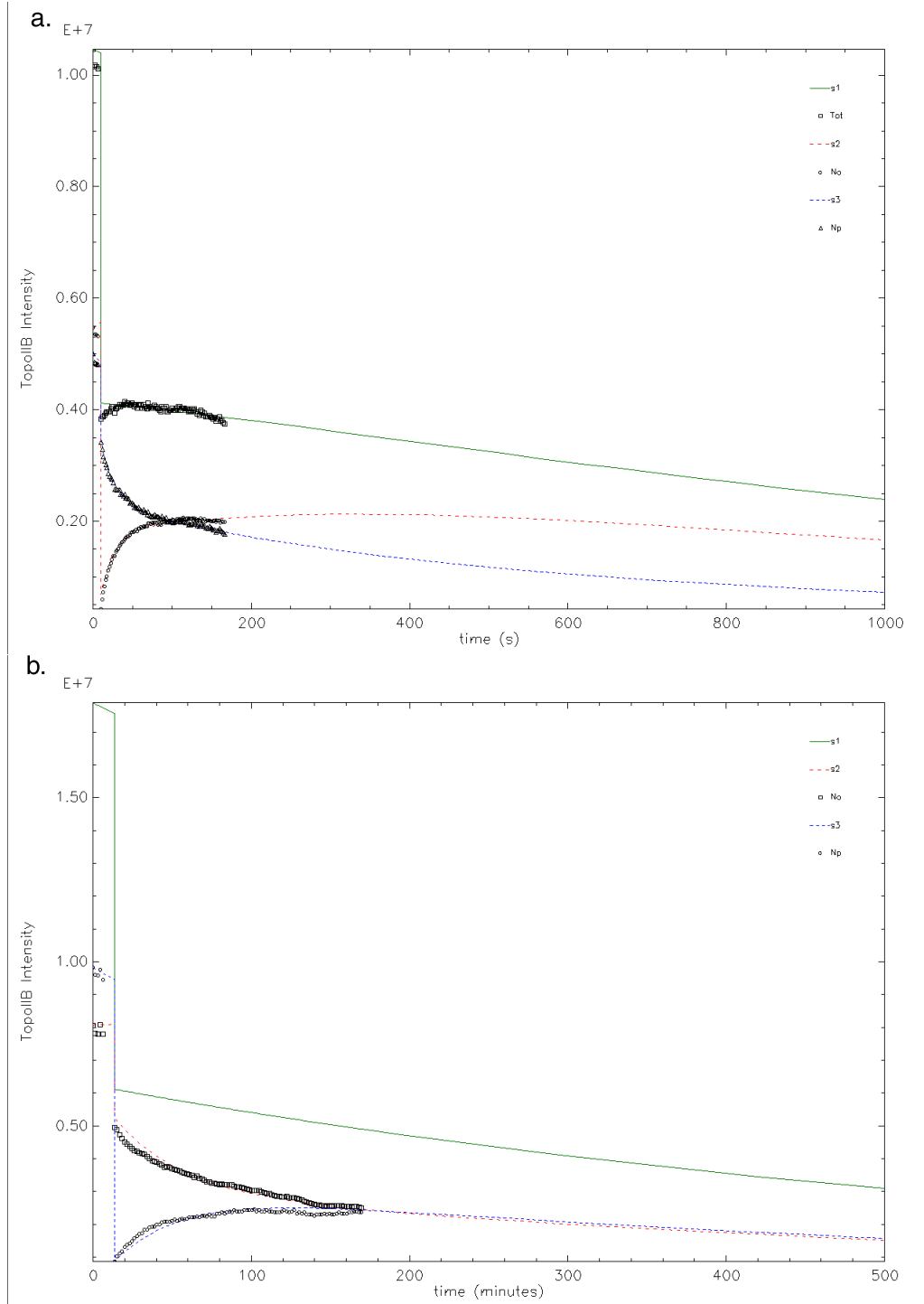


Figure 4.23: The kinetic profiles of recovery in FRAP experiments were fitted using the compartment model of TopoIIβ distribution. graphic representation of the model of topoisomerase distribution in interphase used to model the recovery of the molecule in FRAP experiments. The compartments, represented by circles are bound (bd-nu) and free (free-bd) nucleoplasmic and bound (bd-no) and free (free-no) nucleolar fractions. The arrows represent flows out of a given compartment.

Table 4.2: The fitted flux rate parameters were used to obtain residence times for the Topoisomerase II beta molecule in cells using FRAP experiments with GFP-tagged molecules. The difference in residence times per molecule per  $\mu m^3$  between the bound and free pools of the nucleoplasmic and nucleolar proteins respectively is almost  $10^8$ .

Region of Nucleus	Residence Time [min- $\mu m^3$ /molecule]
Nucleoplasmic free	2.86E+06
Nucleolar free	2.60E+07
Nucleoplasmic bound	3.03E+04
Nucleolar bound	2.86E+07

#### 4.4.3 Testing the TopoIIb Model

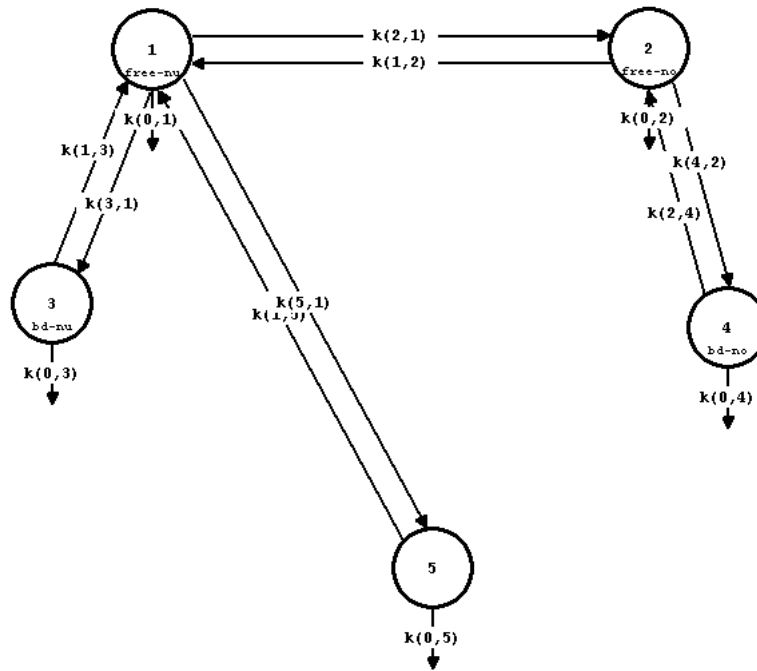


Figure 4.24: The graphic representation of the model of early replication when the nuclear envelope has broken down involves one more compartment, the cytoplasmic. The free nucleoplasmic pool is the only one that directly can empty out into the cytoplasmic reservoir and since there is no barrier between the two compartments, it possesses a maximal rate of exchange.

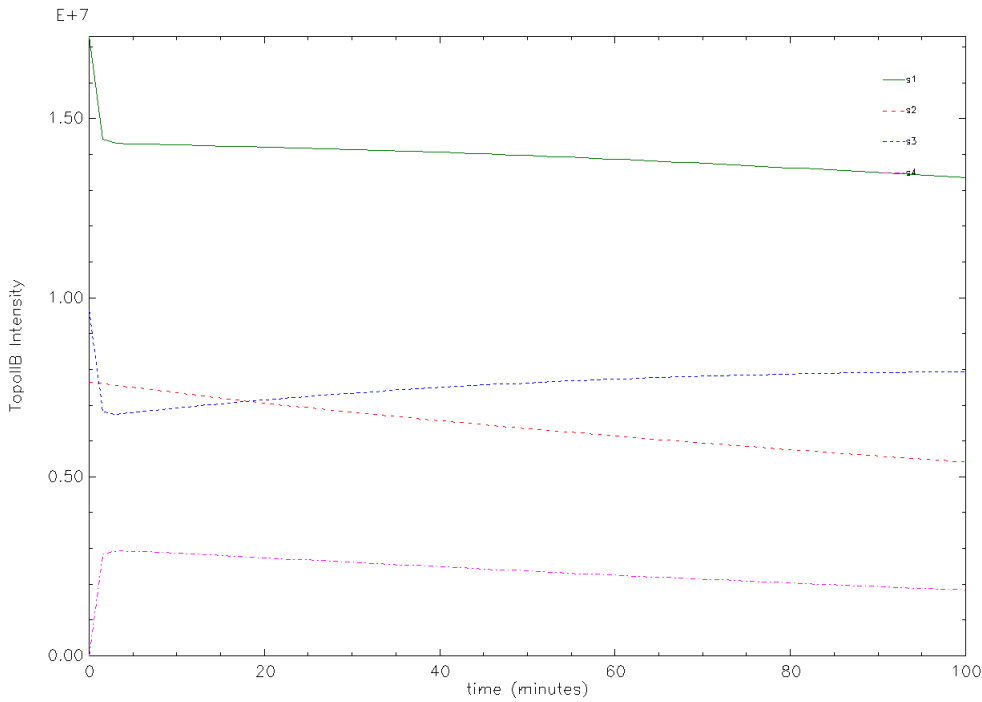


Figure 4.25: The progress of TopoIIb distribution kinetics once the nuclear envelope disappears and a steady state is reached between nucleoplasm (s3), cytoplasm (s4) and nucleolus (s2). The total Topoisomerase signal decreases at a steady rate, indicative of the photo-bleaching due to imaging.

What if experiments are the ultimate power that a model provides. I asked the question of what happens to TopoIIb distribution at the onset of replication. The most important process to occur at early stages of replication is the breakdown of the nuclear envelope. Assuming that the affinity of Topo II beta to the nucleolar and remaining DNA remains constant, I modelled the compartment of the nucleoplasm to adding a further term to our transport equations with a maximal flux rate (Figure (4.24)). The result of the simulation is that the distribution in both the nucleoplasm (s3) and nucleolus (s2) is expected to reduce and that in the cytoplasm rapidly increase and then achieve a steady-state, all in the space of  $\sim 1$ -2 mins (Figure 4.25). The same time scale of rapid loss in the nucleoplasm and rapid rise and steady state in the cytoplasm has been seen in experimental work done earlier (49) in an in vivo study with time-lapse, three-dimensional data sets of living *Drosophila melanogaster* embryos injected with rhodamine-labelled topo II, where localization is temporally regulated and empties out in  $\sim 2$  mins during mitosis. This is clear evidence that my model is consistent and useful for predicting the kinetics of distribution of TopoIIb, in the interchromosomal spaces.

# **Chapter 5**

## **Discussion**

“Why are physicists always having to change the laws? The answer is, first that the laws are not the observations, and second the observations are always inaccurate.”

-Richard Feynman in “The Meaning of it All”

The results of the work presented here are discussed in the following section, especially in the context of the recent work done by many workers over the world. In contrast to earlier work, the findings presented here and concurrently elsewhere (46) demonstrate most proteins in the intra-nuclear space to be extremely dynamic.

## **5.1 Mobility of vimentin nuclear bodies (VNBs)**

I have been able to show here that the *Xenopus* nuclear vimentin is mobile and the bodies can be classed based on the kind of motion they undergo. The mean parameters of size and mobility compare well with those obtained by other workers on *bona fide* nuclear bodies.

### **5.1.1 ATP Independence of VNB Mobility**

The typical test used to examine whether active mechanisms are involved in mobility of a certain structure is to somehow block ATP synthesis, like in transport between compartments (157). In the case of VNBs, depletion of ATP affects only the mean velocities of some particles, and not others. Averages over many cells showed the difference to be within the standard deviation. It might be possible, that the variation might due to cell cycle stage, or minor differences in the physiological state of the cell. However the data for these questions is lacking and this might be an avenue of investigation. However, it would appear to be consistent with known findings for large structures in the nucleus like chromosome territories (42), that were shown to also have a mobility independent of metabolic energy.

### **5.1.2 Rejecting the Compaction Model of VNB Fusion**

During the process of imaging, VNBs can be observed to undergo fusion in the time span of 15-20 min. When I measured both the particle volume as well as the signal intensity of individual VNBs that participate in the process, I found that the mean sum of the post-fusion bodies was the sum of the bodies before fusion. An initial assumption about the motion of the bodies was that it is caused by the thermal diffusive motion of chromosomal territories (CT). Assuming a very crowded environment in the nucleus that VNB-fusion might be the result of CT collisions. This might result in pressure on the bodies (Figure 5.1). Such a model would predict that the volume of the bodies decreased after fusion, while the intensity remained the same, indicating that the post-fusion bodies are denser than the sum of the densities of the pre-fusion bodies. The finding however argues against the model of chang-

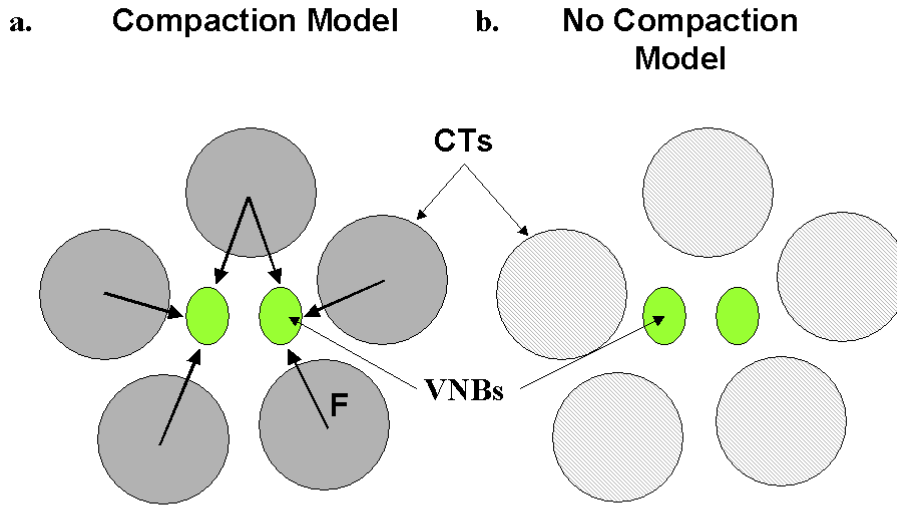


Figure 5.1: The two contrary models for the fusion of VNBs in the nucleus, one predicting the increased density of the body the other, a purely additive process are demonstrated here. CTs are chromosome territories,  $F$  is the force due to the movement and collision of chromosomal territories and VNBs are vimentin nuclear bodies.

ing densities. This suggests that these events are concerned with the nature of the protein under consideration.

### 5.1.3 Size, Velocity and Diffusion Constant

The measured velocities for VNBs had a maximum of  $0.06 \mu\text{m/s}$ . These velocities are of the same order of magnitude as these reported for Cajal Bodies (168), as well as PML bodies (169), but  $\sim 10$  times slower than the ATP dependent PML bodies with velocities of  $0.3 \mu\text{m/s}$  (Table 6.1). These findings indicate that VNBs have similar mobility characteristics and encounter the same kind of obstructions as physiological structures. Therefore, VNBs can be considered as a valuable model system to probe the topology of the interphase nucleus. What is not understood however is whether VNBs localize to any specific position, and if so where and why. In the case of many nuclear bodies like the interchromatin granule cluster (IGC) work done has suggested that there might gene specific nucleation sites after cell division (170) where initial components aggregate and bodies then form around these sites. The other question is also regarding what causes VNB integrity. The first assumption is that it might be homoassociation of unit length filament structures,

which form the bodies (60). However similar temperature conditions in vitro do not produce such body-like patterns. More experimental work is needed to understand the molecular basis of these questions.

#### 5.1.4 High Effective Nuclear Viscosity

The value of the effective diffusion constant,  $D_{eff}$  fitted to the data shows that the effective nuclear viscosity = 17 Poise, making it at least 3 orders of magnitude more viscous than water ( $\eta = 0.01$  Poise). Measurements of fluid phase viscosity in the nucleus however provide a value of  $\sim 0.04$  Poise (12). This is a difference however clearly explained by the fact that the two values are measures of different aspects of the nucleus- the effective viscosity is the net viscosity due to the chromatin, binding and other factors, while nuclear fluid phase viscosity excludes these effects, and only estimates the water based nucleoplasm. Effective nuclear viscosity measured for large bodies has been estimated to be 2.8 Poise (164). Besides as shown in Figure 4.4, the value fitted effective viscosity appears to be a form of compromise that attempts to explain the left side of the experimental data (see figure) which is consistent with the Stokes-Einstein model and the right side of the data which appears not to conform to this. This led to a few alternative scenarios that I imagined might cause this and the results of testing these are discussed in the following section.

#### 5.1.5 Possible Sieving Mechanism of the Nuclear Medium

The plot of diffusion constant against the radii of the particles (4.5) from experimental data shows a clear two-phase distribution. The obvious deviation from the SE model curve for certain particle sizes and the high nuclear viscosity indicate a size dependent phenomenon. This phenomenon is also reflected by the fact that individual particles are capable of simple linear diffusion (Figure 4.6a), diffusion with flow (Figure 4.6b) and restricted diffusion (Figure 4.6c). Thus, I assumed that a size-critical phenomenon might be occurring, and went on to fit a mean critical radius,  $\mu 0.282 \mu m$ . These results indicate that the nuclear medium is not a well mixed compartment, but shows properties that are size-specific. It is tempting to speculate that the interchromosomal domain (ICD) compartment acts as a scale specific sieve. Similar phenomena have been reported in DNA solutions in vitro (171) and were attributed to effects of microviscosity. At present, the exact nature of this hypothetical sieving mechanism remains unclear. Also statistical treatment of the critical diffusion model appears to attribute the difference to random differences, using the F-test. The reason for such a model to be insignificant might lie in the fact that outliers are caused by cell culture conditions or local binding, aspects that would need investigation by fresh experiments.



### 5.1.6 Anomalous Diffusion in the ICD

A comparison between the diffusion model and experimental data indicates that the process of movement of the VNBs corresponds to anomalous diffusion. Although a subset of VNBs do show simple diffusion, there are those that indicate directed (Figure 4.6b) or restricted diffusion (Figure 4.6c). The ensemble average therefore indicates anomaly. Movement of large complexes in the ICD are heterogeneous involving restriction, diffusion and vectorial flow as has also recently shown for Cajal bodies in living mammalian cells (165). The high effective viscosity and the anomaly coefficient of the mean square displacements indicate a high degree of coralling due to either restriction to diffusion or a high binding affinity to components of the nucleus, as suggested in the case of Inter Chromatin Granule Compartment (IGC) (13). The model of nuclear architecture that is based on highly dynamic interactions between small molecules without any real mobility differences between nuclear regions (172, 173), appears to be valid for small molecules rather than larger structures. Diffusion still remains the main process for mobility in the nucleus (46), but it appears that inhomogeneity of the nucleus does cause deviations from ideal diffusive behaviour for large particles.

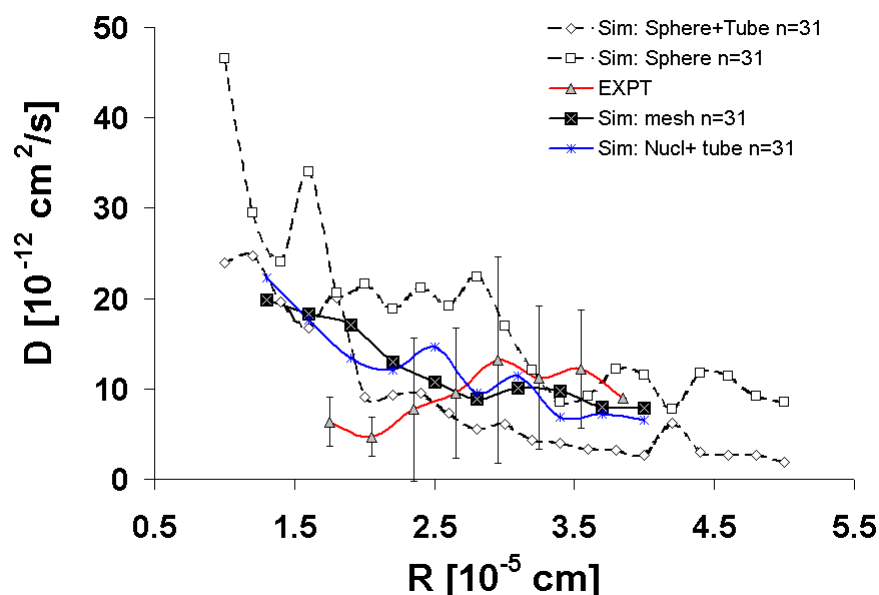


Figure 5.2: A combination of obstacles was tested beyond those that were suggested by previous findings about the ICD channel like space. These were all conducted at a very high effective viscosity ( $\eta = 31$  Poise) and include combinations of tubes, spheres and a single mesh unit.

## 5.2 Simulated Obstacles to Intra-Nuclear Diffusion

To test whether the measurements of anomalous diffusion might be due to a channel-like network in the nucleus, I performed simulations with the measured sizes of nuclear bodies and placed restrictions around them to test whether they might affect their mobility. The ICD compartment space has been shown in experiments of polymerizing *Xenopus* nuclear vimentin (38) to be a reticulate channel-like network. The simulation of a channel restriction appears to show that this does not however have any effect on the diffusion of the bodies (4.12). The advantage of the Monte Carlo method is that it introduces the random variability which we expect from biological systems, especially considering the unknown factors. This might lead to the assumption that the cause of the anomaly, especially in a range of particle sizes might be due to other shapes of obstacles. In the simulated nucleus therefore I put this assumption to test by observing diffusion of VNB sized spheres within the nuclear boundary with additional obstructions such as a surrounding sphere (Sim:Sphere), a channel with a sphere (Sim:Sphere+Tube), a network of channels with one single junction (Sim:mesh) and a single channel within the nucleus (Sim:Nucl+tube) (as seen in Figure 5.2). This figure combined with the F-max test presented in Section 4.1.4, provide convincing evidence that the deviation from ideal diffusion must have other causes. The possible causes then are random as suggested by the F-max test, and due to the sample size, or due to experimental effects that we cannot measure in the in vivo situation inside the nucleus. The sieving observed in the past in intra-nuclear spaces has been with injected dextran molecules (12), where molecules beyond a size simply remain immobile. To establish the cause of the aberrant motion of the VNBs it might be necessary to vary the size of the structures over a larger range and also experimentally dissect any binding interactions as well as the biochemical nature of the VNBs.

## 5.3 Spatial Variations in Intra-Nuclear Diffusion

The study of diffusion of nuclear YFP inside the nucleus was motivated by a model that chromatin dense and less dense regions cause deviations from diffusion due to obstruction. The analyses of the FRAP data showed that if any dependence exists it is very small. Simulations of such FRAP experiments that consider not just the time but also spatial dynamic, present a powerful method to access the spatial effects if any of diffusion within inhomogeneous media.

### 5.3.1 Analysis of Experimental Data

The analysis of the results indicates that chromatin density does not seriously affect the diffusion of the marker. This finding is consistent with work with GFP-tagged transcription factor diffusion (46). The approach of comparing FRAP half-times with the abundance of potential obstacles however allows for the first time a systematic approach to the problem. The individual variations in the recovery between cells as seen in Figure 4.15 and its dependence on chromatin density indicates that cell status might eventually decide whether chromatin density will or will not affect mobility. It would be interesting to perform a similar study in cells in different states like quiescent and dividing, as well as transformed and untransformed.

### 5.3.2 Fitting a Diffusion Tensor

Work done in a collaboration with Dietmar Volz, fitted a diffusion tensor to the bleaching recovery data (174). This tensor is an extension of the diffusion constant. It has two components, one in the X-direction ( $D_x$ ) and the other in the Y-direction ( $D_y$ ). Mammalian cell nuclei of the type studied do differ prominently in the X- and Y-dimensions, i.e. anisotropic. So the method used distinguishes between two arbitrary perpendicular directions. The fit error which is the ratio of X- and Y-components of the diffusion tensor, appears to vary with location. Thus it appears to be high at the borders of the nucleus and low in its interior (174). In light of the observation that total fluorescence inside the nucleus and cytoplasm remain more or less constant, this finding is not unexpected. However, it does make a strong case for considering the boundary of the nucleus in work that attempts to estimate the diffusion constant in a FRAP experiment. The optimal method to do this for an arbitrary geometry would be numerically simulate the process in a spatial manner.

### 5.3.3 2-D Simulation

Although the analysis show little influence of chromatin density on diffusion of the chosen nuclear YFP probe, the 2-D simulation of the FRAP experiment allows for a two-fold advantage. On the one hand, it allows the boundary effects to be overcome, as discussed in Section 5.3.2. On the other, it also permits mobility parameters to be fitted to FRAP experiments that are not ideal (175 and Section 4.3.2). The shortcoming of the model as it stands however is that the most common means of achieving inhomogeneity in the nucleus appears to be binding. Thus to be realistic, the 2-D simulation cannot simply simulate diffusion, but needs to necessarily include binding.

## 5.4 Topoisomerase Distribution between Nucleus and Nucleoplasm

The model of topoisomerase distribution inside the nuclear sub-compartments that I have presented (Figure 4.22), summarizes the work done by varied workers in the area.

### 5.4.1 Validation of the Model

To test whether the model is useful I used it to predict the distribution of the molecule in case of nuclear envelope breakdown (Figure 4.25). Fortunately the experiment to test the prediction has already been performed earlier in living *Drosophila melanogaster* embryos (49). The overlap in orders of magnitude of the molecular distribution dynamics, would indicate that the model parameters and structure are valid.

However to be more powerful, the model must involve a ligand that actually binds to the molecule and this needs experimental verification and questions of affinity. Similar work on RNA polymerase II distribution (176) suggests that the local ‘compartments’ and structures seen in the nucleus, are not static assemblies, as commonly held, but dynamic and easily perturbed.

## **Chapter 6**

### **Conclusions and Outlook**

“Knowledge is of no real value if all you can tell me is what happened yesterday. It is necessary to tell what will happen tomorrow if you do something - not only necessary but also fun. Only you must be willing to stick your neck out.”

-Richard Feynman in “The Meaning of it All”

The work presented here has designed and tested three models that predict different aspects of the behaviour of molecules and molecular complexes in the inter chromatin space of the nucleus. The mobility of a large diffusing nuclear body, small diffusing protein and a differentially binding topoisomerase molecule are the systems for which models were arrived at. In the following sections I will dwell in detail on these models, their consequences and work that might be done in future to refine these models.

## **6.1 Nuclear Body Diffusion and Integrity**

According to a recent count, more than 20 different nuclear bodies having been identified (177). Recently the proteome of the nucleolus has also been analyzed (178) and new nuclear bodies discovered like the Paraspeckle (179). Studying the mobility of nuclear bodies has for instance in the case of the IGCs revealed that velocity and budding events correlate with the transcriptional state of neighbouring genes (180). This work adds to understanding the mobility of nuclear bodies as presented in the following sections.

### **6.1.1 Anomalous Diffusion of Nuclear Bodies**

In this study of the mobility of VNBs, I have shown that artificial nuclear body movement is diffusive and driven by thermal energy. The nuclear medium has an effective viscosity of 17 Poise, making it at least 3 orders of magnitude more viscous than water ( $\eta = 0.01$  Poise). Since however a model of critical diffusion must be rejected for explaining aspects of deviation from ideal diffusion, it can only be presumed that binding might play a role. The exact identity of these binding partners can and is being approached by screening for interacting proteins (work in progress in the labs of Harald Herrmann). The three different modes of diffusive motion inside the nucleus, present the nucleus as a medium that at different locations inside it, affects mobility differently. These effects might be to allow unrestricted diffusion, to corral movement in a radius of  $\sim 1 \mu\text{m}$  or to provide a directed velocity of  $\sim 0.003 \mu\text{m/s}$  (Figure 6.1).

It would be interesting as an extension of this, to investigate the structural and probable molecular causes of these different modes of diffusion. This could lead to a correlation of mobility and molecular map of the nucleus. Superimposed on specific location of genes it is hoped might finally solve some of the mystery around the functional role of nuclear bodies (13).

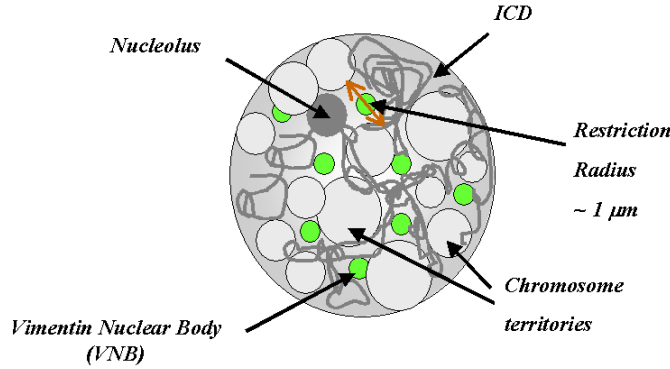


Figure 6.1: The refined interchromosomal domain (ICD) compartment model with VNBs (green dots) is depicted here. Chromosome territories are entirely inaccessible regions for VNBs as reported in [25]. The dense packing of chromatin in the regions where the VNBs are located results in a high effective viscosity.

### 6.1.2 Fusion does not Change VNB Density

Upon fusion of two individual VNBs, both the particle volume as well as the signal intensity sum up, indicating that fusing VNBs do not undergo compaction. This finding rejects the simple mechanical model, of fusion events caused by a force pushing bodies in the inter chromatin space together. It could be speculated that the fusion events are a minimization event of weak electrostatic exclusion by the surrounding nuclear medium, akin to fusion of oil droplets in water.

Understanding the nature of the vimentin accumulations at a biochemical level and what might be driving their compaction would probably better help establish the effects observed and serve also to better understand the forces that maintain nuclear body size.

### 6.1.3 Rules of Nuclear Body Size and Mobility

Nuclear bodies follow certain “rules” of size and mobility as seen in a comparison of the results of this work with that of other workers (Table 6.1). These rules would appear to suggest that nuclear bodies, artificial VNBs, CBs and PML bodies, have a diameter between 0.1 and 1  $\mu\text{m}$ . Their effective diffusion constants ( $D_{eff}$ ) are also between 1 and 4  $\mu\text{m}^2/\text{s}$ .

Table 6.1: The measured values of the diameter, velocity of movement and diffusion constant of different NBs based on work done by other workers are summarized here. Combined with the values for VNBs, they appear to suggest that nuclear bodies might be constrained by something in the ICD space to maintain the size and mobility ranges observed. It suggests that a physical mechanism might be determining nuclear body size and mobility.

Nuclear Body	Particle Diameter [ $\mu\text{m}$ ]	Velocity [ $\mu\text{m/s}$ ]	$D_{eff}$ [ $\mu\text{m}^2/\text{s}$ ]	Reference
PML Bodies	0.2 to 1.4	0.06 to 0.12, max. 0.3	-	169
CBs	<0.2 and 0.4 to 0.7	Max. 0.015	2 (mean)	168, 165
VNBs	0.3 to 0.7	0.01 to 0.06	1.6 to 4.4	181, this work

The striking nature of the rules proposed here is that they are valid for the artificial nuclear body, the VNB as well as for *bona fide* ones such as PML bodies and CBs. This once more points to potential theoretical and experimental work to investigate the mechanism that might regulate nuclear body size, especially with the CBs and PML bodies. A potential experimental approach for example could involve mutant screens of component proteins that knock-out size-control or integrity of the bodies.



## 6.2 Simulating Nuclear Body Motion and Stability

The experimental analysis of Section 6.1 raises the question of what causes diffusion of nuclear bodies to be anomalous. Also the consistency of rules between mobility of artificial and *bona fide* bodies suggests that physical constraints might be responsible. The monte carlo diffusion simulation is a first attempt at testing one of the possible causes *in silico*.

### 6.2.1 ICD Channels do not affect VNB Motion

The ICD channel of dimensions expected from earlier work (38, 154) had been expected to obstruct diffusive mobility. On simulating these in a simple but physically realistic manner, this can be rejected. This is based on results that show variation of  $D_{eff}$  with particle size not being fully explained by the model (Figure 4.12), or even by an empirical model (Figure 4.5). The effect observed appears to be due to random chance. Also the very high effective viscosity and high anomaly coefficient, might then be explained by binding of some of the bodies to nuclear components.

Experimental evidence has been accumulating recently from RNA molecules (11) and transcription factors (46) that shows that diffusion is effective enough a mechanism to bring molecules to the desired location in reasonable time. This has been shown in other organelles like the ER as well as Golgi (14). So it is consistent with this that the nuclear body motion and its deviation from standard diffusion do not depend on obstructions to diffusion. (14). So it is consistent with this that the nuclear body motion and its deviation from standard diffusion do not depend on obstructions to diffusion.

In future it might be interesting to modify the simulation to include binding to structures like chromosome territories, or other nuclear bodies and examine if these cause some of the anomaly observed.

### 6.2.2 Formation and Stability

A wider question of how nuclear bodies form might eventually lead to a clearer idea of both their function as well as better understanding their mobility. The simulation tool presented here could be used in future work to simulate the reassembly of nuclear bodies, including molecular interactions between the components. Recent work with IGC re-assembly after cell division suggests that the components disperse into the cell and sequentially reassemble in daughter nuclei (170). The model would borrow aspects from work in other fields and treat the process as a self-organizing adaptive biosystem as has been done with patterns in tumour growth (182).

### 6.2.3 Energy Dependent Mobility

Recent work presented measurements of a subset of nuclear bodies the mobility of which was reduced tenfold by depleting metabolic energy as in the case of PML bodies (169) and mRNP complexes (183). Conversely Cajal body mobility has been shown to increase after ATP depletion. In the case of the work presented here with VNBs in contrast, no dependence on metabolic energy could be observed. This might provide a clue to the mechanism, since the VNBs might lack the molecular machinery to be affected in its mobility by ATP depletion. When such changes in motion have been seen in case of PML bodies and CBs, they affect only a small percentage of the bodies. The means by which these differences might arise is still unclear. Although myosin I (184) as well as actin monomers have been localized in the nucleus, no obvious actin-myosin motor-fibre complexes have been seen like in the cytoplasm. Therefore some hypothetical models have been proposed (185, 13). Explicitly modelling the process might allow some of the hypotheses to be tested and throw up new ones.

### 6.2.4 Mechanisms of Regulated Mobility

The mobility of the nuclear body compartments has seen a flood of recent studies. In a study by Eils et. al. (180) the velocity and budding events of the IGC or speckles was shown to correlate to transcriptional state. Recent studies examining chromosome mobility dependent on the cell cycle stage (186) and proximity to nuclear compartments on specific chromosomes (187) have confirmed the view of regulated mobility.

All these phenomena might have possible scenarios explaining them and the simulation tool presented here could be modified with appropriate experimental data about interactions, to generate testable hypotheses about nuclear body integrity and mobility.

## 6.3 Spatial Influences on Nuclear Protein Diffusion

The work with VNBs has shown that different locations in the nuclei appear to affect mobility of nuclear bodies differently. Therefore simplifying the system further, the effect of chromatin density on the diffusion of a small inert marker protein was tested.

### 6.3.1 Chromatin Effects on YFP Mobility

From the results it is clear that variations in chromatin density do not affect the mobility of small diffusing molecules like an inert nuclear YFP. This indicates a model of the nucleus, for the size scale of such a small molecule (hydrodynamic radius  $\sim 2nm$ ). The model predicts that there will be no great variation in diffusive mobility within the nuclear medium for molecules in the same size range. This has been suggested, but not explicitly shown in concurrent work measuring FRAP mobility of transcription factors (46), since no chromatin label was used.

### 6.3.2 Spatial Simulations for Discovering Novel Genomic Sites

Although the simulation of an inert nuclear YFP does not tell us much about the inhomogeneity of the nucleus, it does provide a platform on which to test other molecular systems. To begin with the simulation will need to include binding and as an input also require binding constant values.

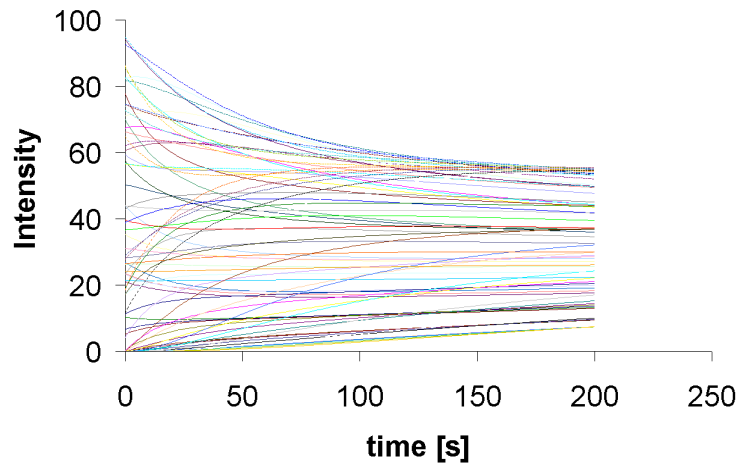


Figure 6.2: *Recovery profiles: The signal of the experimental data for each and every simulated subregion of the cell is displayed here.*

It would then be possible to use such a method to the study of transcription factors that on induction are known to have a very high affinity to specific regions of the genome, as in the case of the glucocorticoid receptor (188). Deviation from the expected model could be due to undiscovered binding sites in the genome. The advantage of the simulation is that every simulated element of the region of the cell under consideration can be quantitatively followed as demonstrated in Figure 6.2.

The need for forward simulations when estimating mobility from FRAP experiments has been demonstrated recently (175). The work presented here provides a framework for building diffusion maps of the cell nucleus, which combined with

spatially distributed maps of the genome will probably help speed up the discovery of gene functions.

## **6.4 Self-Organizing Model of Nuclear Structure- e.g. Topoisomerase**

The visualization and modelling of Topoisomerase II localization demonstrate the principle of simple interaction rules and constant flux, leading to the emergence of self-organizing structure (189).

### **6.4.1 Predictive Model of TopoisomeraseII $\beta$ Distribution**

The distribution of TopoIIb molecules is dynamic as seen in recent work (166) and the model presented here mathematically expresses and fits the data. The power of such a model is demonstrated by correctly predicting the efflux kinetics of the molecule during early cell division (Figure 4.25).

In future the model will be used to test the effect of other perturbations in the distribution of topoIIb like for instance the effect of inhibitors and any deviations between simulation and experiment would be indicative of a need to refine the model.

### **6.4.2 Evidence for Self-Organization in Nuclear Organization**

The distribution of topoisomerase in the inter chromosome space and on chromatin has been thought in the past to be static and even form a manner of scaffold (47). This work shows that such a scaffold need not be invoked in an integrative model, since diffusion and different binding affinities suffice to explain the localization patterns and their dynamics as observed in experiment (166) and the model simulation (this work).

This might be seen to have bearing on the mechanisms that give rise to nuclear architecture, away from a scaffold and rigid compartments, toward a more dynamic one, based on diffusion and interaction.

## **6.5 Outlook**

New techniques of high resolution microscopy such as 4Pi-microscopy (69) and FCS (190) are making ever higher spatial and temporal resolutions available for studying molecular diffusion characteristics. Such studies will help to improve the transport model of molecules. In future studies, additional terms like binding, and maybe even single collision events will be taken into account. These methods might

be employed fruitfully for addressing anomalous diffusion dynamics in the nucleus and help design probes for specific nuclear locations (191).

A parallelization of mobility assays, extending work with fixed cells expressing fluorescent cDNA clones to recognize patterns in localization (192) would widen the understanding of the complex nature of intra-nuclear dynamics and its influence on genetic disease.

To deal with issue of data-volume from live cell microscopy studies, data models are being developed to deal with such multi dimensional data (193). The Open Microscopy Environment (OME) (194), for example aims to create a universal data standard and tools for the analysis and mining of relevant information and even automatic model generation.

The kinetic model presented of topoisomerase distribution is simple and therefore its topology was generated manually. In future work, as more and more complex problems are approached, the topology of the mathematical model will be automatically generated as with the database driven approach for modelling the STAT pathway (195) or structural optimization of metabolic pathway models (196, 197).

The predictive model of topoisomerase localization dynamics presented here (198) combined with recent results with RNA editing enzymes in the nucleolus (199) show that though highly mobile, these proteins are captured at specific site and this suffices to keep the nucleolus functioning . Work on a framework for RNA polymerase assembly by kinetic modelling (176) shows a way in which such emergent order of nuclear components can be built up, using the known aspects of molecular interactions, localization and function.

More recently, the nucleolar proteome has been mapped by mass spectrometry (178), presenting a “parts list” of the nucleolus. It should be possible with the dynamics data as well as qualitative interaction data to investigate the dynamics of localization of proteins in the nucleus, and the nucleolus appears to be a good place to start. Simulation of pattern formation in non-equilibrium systems in biology, using principles of “self-organization” has already been used successfully to the aster formation in microtubules (200, 201, 202). The advantage of the nuclear system is that some of the component models are already available. However the nucleus is turning out to be a very complex organelle, and so the effort to ‘assemble’ a model with many sub-processes might take more time and work. Simulation environments like the Virtual Cell (203 and 204), MCell (205) and model standards like Cell modelling Language (CellML) and Systems Biology Markup Language (SBML) (206) will facilitate easier integration of these models in future.

Therefore this work comes at a time when the combination of live cell microscopy, analysis, modelling and experimental design are beginning to converge. With the mobility of vimentin, the effective diffusion of nuclear YFP and topoi-

somerase distribution, I have been able to show that in these specific cases, self-organization is at work, since the systems are far from equilibrium, and show a flux with a steady state and produce structure. That the system is able to rapidly change distribution on a signal is demonstrated by the rapid diffusion of TopoII into the cytoplasm at the onset of division, as also a reticulate distribution in interphase on drug treatment. This work provides evidence for the hypothesized self-organizing principle determining nuclear structure (189), in this case determining stability and mobility of nuclear bodies in the inter chromatin space.

# Chapter 7

## Abbreviations

2/3-D	2/3 dimensional
AOD	acoustic optical deflector
CB	Cajal body
CCD	charge-coupled device
cDNA	complementary DNA
CFP	cyan fluorescent protein
CLSM	Confocal Laser Scanning Microscopy
DMEM	Dulbecco's modified Eagles Medium
DNA	deoxyribonucleic acid
EAST	enhanced adult sensory threshold
EDTA	ethylenediaminetetraacetic acid
EGFP	enhanced GFP
END	extra-chromosomal nuclear domain
FCS	fluorescence correlation spectroscopy
FISH	fluorescence in situ hybridization
FITC	fluorescein isothio-cynate
FLIM	fluorescence lifetime imaging
FLIP	fluorescence loss in photobleaching
FPR	fluorescence photobleaching recovery
FRAP	fluorescence recovery after photobleaching
FRET	fluorescence resonance energy transfer

GFP	green fluorescent protein
H2B	histone 2-B
ICD	interchromosomal domain
IGC	interchromosomal granule compartment
LSM	laser scanning microscope
mRNA	messenger RNA
MSD	mean square displacement
NA	numerical aperture
NB	nuclear body
NLS	nuclear localization signal
ODE	ordinary differential equation
PBS	phosphate buffered saline
PDE	partial differential equation
PML	promyelocytic leukemia
PMT	photomultiplier tube
RNA	ribonucleic acid
RNP	ribonuclear protein
ROI	region of interest
RSP	reflection short pass
SE	Stokes-Einstein
TF	transcription factor
topo	topoisomerase
VNB	vimentin nuclear body
WFM	wide field microscope
XFP	X (any colour) fluorescent protein
YFP	yellow fluorescent protein



## Appendix A

### Flow Diagram of Monte Carlo Simulation Program

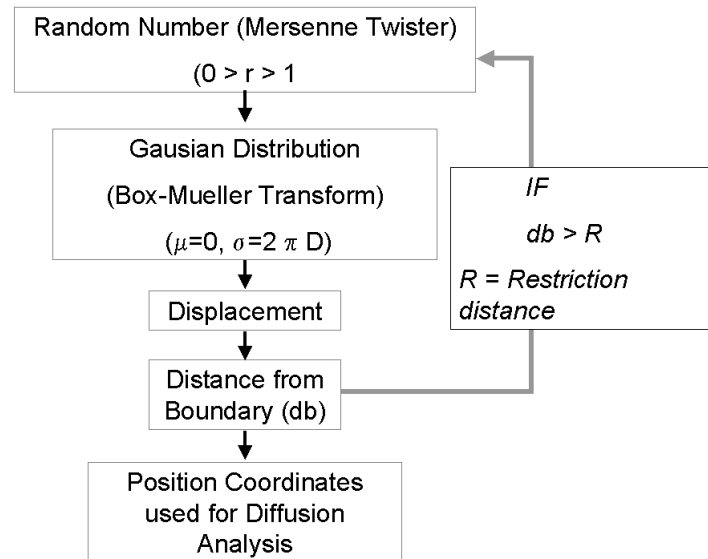


Figure A.1: The simulation of discrete diffusion of particles was implemented in C++ based on the algorithm of Ermak and McCammon (161) and it is schematically represented here. The random number generator (RNG) used was the Mersenne Twister (207), which has passed the so-called “Die-Hard” test and has a the period of  $2^{19937} - 1$ . This RNG can be freely downloaded from the website <http://www.math.keio.ac.jp/matsumoto/emt.html>. For purposes of visualization the OpenInventor libraries ver.2.5.2 (TGS Inc., USA) were used.

## **Appendix B**

### **Text of the Reports published in Genome Biology**

The text of the web-reports on the Genome Biology web-portal that I published (204, 205, 208) are included in the following pages.



## Cell-simulations portal.

The National Resource for Cell Analysis and Modeling  
[<http://www.nrcam.uchc.edu/>]

Maintained by The Center for Biomedical Imaging  
Technology, University of Connecticut Health Center, USA.

---

**Reporter:** Chaitanya Athale

**Report date:** 19 November 2001

*Genome Biology* 2001, **3**(1):reports2002

The electronic version of this article is the complete one and can be found online at  
<http://genomebiology.com/2001/3/1/reports/2002/>

© BioMed Central Ltd (Print ISSN 1465-6906 | Online ISSN 1465-6914)

### Content

The National Resource for Cell Analysis and Modeling (NRCAM) includes virtual cell software for simulating and modeling cell processes and aims to become a portal for modeling in cell biology. Most sites for computational cell biology focus on a single database, a software tool or a data standard, but this one attempts to combine all these aspects. On offer is a mathematical framework for modeling molecular species, biochemical reactions, cellular structures and geometry. The results of simulations can be downloaded as data in comma-delimited ASCII files in zipped form, and the visualization of spatial simulations as animated GIF and QuickTime movie files, also compressed. The site is aimed at intermediate-level users with at least an idea of modeling in biology as well as a clear model that they intend to build and use. A database of binary images assists in generating realistic model geometries. Tutorials and a list of published applications are also available. A simple explanation of model geometry, the use of remote computing and a database and language for the exchange of models place this site among the prominent resources for *in silico* biology. There are links to events such as the first International Symposium on Computational Cell Biology and the International Conference on Systems Biology. Registration is required before the modeling program can be used but there are no registration charges for academic users.

**Navigation**

Navigation is reasonably straightforward and finding the different parts of the site is easy, although there is no dedicated search engine. The links back and forth are not uniform, however: good in some places but absent from others. Customization is possible in the modeling, simulation and image framework. Most pages print as they are seen on-screen, including the figures. No special software, other than a JAVA-enabled browser, is needed to access the site.

---

**Reporter's comments****Timeliness**

The last update at the time of writing was 13 June 2001 with Version 3.0 of Virtual Cell.

**Best feature**

The availability of a modeling platform that frees biologists from having to invest in local computing resources is great. It realizes the vision of remote computing with bare-bones computers logged into central high-performance machines over the internet.

**Worst feature**

At the moment, even small simulations take a very long time to run, without any indication of how long it will take. The response to feedback is poor, having taken over a working week for me

**Wish list**

Better performance from the program and a fitting and optimization module added to the virtual cell software would certainly add to the attractiveness of the resources.

**Related websites**

Tools for similar simulations in cell biology are commercially available for work offline from Berkeley Madonna [<http://www.berkeleymadonna.com>] and the ordinary differential equations (ODE) and partial differential equations (PDE) solvers of MATLAB [<http://www.mathworks.com>]. Image libraries of cells are available at, for example, the Virtual Cell [<http://www.life.uiuc.edu/plantbio/cell/>] for plant cells. Data standards in computational cell biology are available at CellML [<http://www.cellml.org>] and Systems Workbench Development Group [<http://www.cds.caltech.edu/erato/>].

---

**Table of links**

The National Resource for Cell Analysis and Modeling

[<http://www.nrcam.uchc.edu/>]

Berkeley Madonna [<http://www.berkeleymadonna.com>]

MATLAB [<http://www.mathworks.com>]

Virtual Cell [<http://www.life.uiuc.edu/plantbio/cell/>]

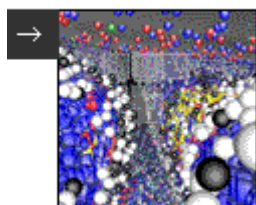
CellML [<http://www.cellml.org>]

Systems Workbench Development Group

[<http://www.cds.caltech.edu/erato/>]

Assumptions made about all sites unless otherwise specified:

The site is free, in English and no registration is required. It is relatively quick to download, can be navigated by an 'intermediate' user, and no problems with connection were found. The site does not stipulate that any particular browser be used and no special software/plugin are required to view the site. There are relatively few gratuitous images and each page has its own URL, allowing it to be bookmarked.



## Monte Carlo cell simulations.

MCell [<http://www.mcell.psc.edu>]

Maintained by Joel R Stiles, Pittsburgh Computing Center, USA, and Thomas M Bartol Jr, The Salk Institute, USA. A MCell mirror site [<http://www.mcell.cnl.salk.edu/>] is available.

---

**Reporter:** Chaitanya Athale

**Report date:** 11 November 2001

*Genome Biology* 2001, **3**(1):reports2001

The electronic version of this article is the complete one and can be found online at <http://genomebiology.com/2001/3/1/reports/2001/>

© BioMed Central Ltd (Print ISSN 1465-6906 | Online ISSN 1465-6914)

### Content

The general Monte Carlo simulator of cellular microphysiology (MCell) on this site is a program that allows three-dimensional dynamic simulations of subcellular architecture and physiology. In addition to an introduction to the modeling of cellular physiology, details of probability and random-event-based methods and complex geometry generation are discussed. The MCell program can be downloaded after registration (free to academic users). The site provides a good introduction to researchers interested in using Monte Carlo Simulations (a random number based simulation method, with the physical process simulated directly by sampling a probability distribution function) to answer questions in cellular physiology and structure, as well as having much to offer for users of the MCell tool. There are links to other simulation tools such as NEURON [<http://neuron.duke.edu>] and GENESIS [<http://www.bbb.caltech.edu/GENESIS/>] and visualization tool sites such as Open Visualization Data Explorer [<http://www.research.ibm.com/dx/>] and POV-Ray [<http://www.povray.org/>]. The minimal nature of the site and the clear introduction to the simulation of microphysiology are its most striking features.

### Navigation

Most parts of the site can be found easily and there are tutorials for its use. There are some ambiguous links, including example images. Once in any of the internal pages, there are no links to other pages, which makes moving around a bit tedious. Browsing is easy but customization is not possible. The site has a lot of large images, and on a low-bandwidth connection this might slow access down. Printing pages is not ideal, as text and images do not fit on standard pages, but text and images can be easily downloaded. The response to feedback is excellent and useful answers were obtained within a working day.

---

### **Reporter's comments**

#### **Timeliness**

There is no mention of when the site was last updated, but the new downloading facility for the program was added in October 2001.

#### **Best feature**

Monte Carlo simulation methods are not widely represented in cell-simulation websites, so the good overview of modeling in cell biology and the relevance of the Monte Carlo approach is welcome.

#### **Worst feature**

A lack of clear links on every page makes navigation difficult.

#### **Wish list**

A hyperlink to each of the beta-test laboratories to see concrete results from applications of MCell would be desirable.

#### **Related websites**

The National Partnership for Advanced Computational Infrastructure (NPACI) [<http://www.npaci.edu/>] is an affiliate that supports efforts to parallelize (modify the program to do many calculations on different processors at the same time to speedup the program) the MCell tool. Related tools for modeling microphysiology are Virtual Cell at the National Resource for Cell Analysis and Modeling [<http://www.nrcam.uchc.edu/>], StochSim [<http://www.zoo.cam.ac.uk/comp-cell/StochSim.html>] for stochastic kinetics, Nanosimulation of the cytoskeleton [<http://pegacat.com/cbetts/phd/index.html>] for simulation of the cytoskeleton, and bio-medical data visualization tools such as Amira [<http://amira.zib.de/>].

---

### **Table of links**

MCell [<http://www.mcell.psc.edu>]

MCell mirror site [<http://www.mcell.cnl.salk.edu/>]

NEURON [<http://neuron.duke.edu>]

GENESIS [<http://www.bbb.caltech.edu/GENESIS/>]

Open Visualization Data Explorer  
[<http://www.research.ibm.com/dx/>]

POV-Ray [<http://www.povray.org/>]

National Partnership for Advanced Computational Infrastructure  
(NPACI) [<http://www.npaci.edu/>]

National Resource for Cell Analysis and Modeling  
[<http://www.nrcam.uchc.edu/>]

StochSim [<http://www.zoo.cam.ac.uk/comp-cell/StochSim.html>]

Nanosimulation of the cytoskeleton  
[<http://pegacat.com/cbetts/phd/index.html>]

Amira [<http://amira.zib.de/>]

Assumptions made about all sites unless otherwise specified:

The site is free, in English and no registration is required. It is relatively quick to download, can be navigated by an 'intermediate' user, and no problems with connection were found. The site does not stipulate that any particular browser be used and no special software/plugin are required to view the site. There are relatively few gratuitous images and each page has its own URL, allowing it to be bookmarked.





## Software for cell simulation

E-Cell simulation environment

[<http://www.bioinformatics.org/e-cell>]

Maintained by Kouichi Takahashi, Laboratory for Bioinformatics, Keio University SFC, Japan.

---

**Reporter:** Chaitanya Athale

**Report date:** 21 January 2002

*Genome Biology* 2002, **3**:reports2011

The electronic version of this article is the complete one and can be found online at <http://genomebiology.com/2002/3/3/reports/2011>

© BioMed Central Ltd (Print ISSN 1465-6906 | Online ISSN 1465-6914)

### Content

The E-CELL simulation environment site is dedicated to the software tool E-CELL, which simulates biochemical interactions in cells in order to understand regulation at the level of a whole cell or organelle. The primary focus of the site is software engineering of the E-CELL environment, unlike many other cell-simulation sites that focus more on biological applications, such as understanding metabolism, signaling, growth and development. The site offers developers the source code of versions 1.x and 2.x of E-CELL (3.x is currently in development), and a comprehensive collaborative platform courtesy of Bioinformatics.Org, which is a not-for-profit academia-based virtual lab that facilitates open-source software development and the exchange of bioinformatics research. Users can download the program in Linux or Windows formats, and an HTML or postscript users manual is also available. The pages discussing the latest news on E-CELL version 3.x, which is still in development, are the most interesting for developers, since they point to the vision for a 'community standard platform for at least 10-15 years'. For the users of the tool, the E-CELL project homepage will prove more useful, since it discusses modeling issues.

### Navigation

Access was good at all times tested, and searching and browsing is not problematic. The site is mainly organized into three modules (for the developer, user and general audience), and each module has a clear but different structure. As the design of the modules differs, moving within a module is convenient, but once one has crossed over from one to another, getting back can be inconvenient. The section devoted to the E-CELL development and user forums is full of dynamic sections where comments can be directly added to the online material. Other parts of the user forums are also convenient to search because of the use of the MoinMoin-based script with features like indices based on title, words and recent change, full search facilities and page views showing deletions and additions. The literature on the site can be downloaded in HTML and postscript formats. E-CELL software versions 1.x and 2.x are available for download under a General Public License (GPL), with source code as well as the model descriptions.

---

### **Reporter's comments**

#### **Timeliness**

The site was last updated on 11 November 2001.

#### **Best feature**

The multitude of features on offer for collaboration and exchanges between and within the developer and user communities is by far the best aspect of the site.

#### **Worst feature**

A lack of discussion about results obtained with the stable E-CELL version (version 1.x ) is the biggest deficiency.

#### **Wish list**

Discussions about results obtained with E-CELL and a list of related and similar sites.

#### **Related websites**

The older E-CELL site [<http://www.e-cell.org>] hosts a user manual, literature, models, a user mailing-list and information about Masaru Tomita's group, who created E-CELL. This site has links to the lab in which the E-CELL project started - the Bioinformatics Laboratory at Keio University [<http://www.bioinfo.sfc.keio.ac.jp/>] - and the Institute for Advanced Biosciences, Keio University

[<http://www.ttck.keio.ac.jp/IAB/>], where further work on the project, including the application of E-CELL to optimal industrial-microbe design, is planned. Tools similar to E-CELL are also available at the websites for GEPASI [<http://www.gepasi.org/>], a biochemical network simulator, and GENESIS [<http://genesis.bbb.caltech.edu/GENESIS/genesis.html>], a tool for simulating neural genetic and physiological networks on both the single-cell and systems scale.

---

#### **Table of links**

E-Cell simulation environment

[<http://www.bioinformatics.org/e-cell>]

Bioinformatics.Org [<http://bioinformatics.org>]

MoinMoin-based script [<http://moin.sourceforge.net/>]

The older E-CELL site [<http://www.e-cell.org/>]

Bioinformatics Laboratory at Keio University

[<http://www.bioinfo.sfc.keio.ac.jp/>]

Institute for Advanced Biosciences, Keio University

[<http://www.ttck.keio.ac.jp/IAB/>]

GEPASI [<http://www.gepasi.org/>]

GENESIS

[<http://genesis.bbb.caltech.edu/GENESIS/genesis.html>]

Assumptions made about all sites unless otherwise specified:

The site is free, in English and no registration is required. It is relatively quick to download, can be navigated by an 'intermediate' user, and no problems with connection were found. The site does not stipulate that any particular browser be used and no special software/plugin-ins are required to view the site. There are relatively few gratuitous images and each page has its own URL, allowing it to be bookmarked.

# List of Figures

2.1	Hierarchical organization of chromatin from DNA to chromosomes	13
2.2	Scale of a typical nucleus . . . . .	15
2.3	The principle of confocal microscopy . . . . .	23
2.4	Schematic view of a confocal microscopy setup . . . . .	34
2.5	The spectra of GFP and its variants . . . . .	35
2.6	Image processing workflow . . . . .	36
2.7	the principle of FRAP and FLIP and values to be extracted . . . . .	37
3.1	Example of preprocessing microscopy images . . . . .	54
3.2	Schematic view of MSD calculation . . . . .	56
3.3	The three typical modes of diffusion . . . . .	57
3.4	Simple compartment model . . . . .	59
3.5	Spatial discretization in a 2-D diffusion simulation . . . . .	60
4.1	3-D distribution of VNBs . . . . .	63
4.2	Movement of sample VNBs over time appears random . . . . .	64
4.3	Frequency distribution of VNB velocity, size and diffusion constants and the effect of ATP depletion . . . . .	65
4.4	Variation of D with VNB size and comparison to the SE model . . . . .	66
4.5	Different models of D vs VNB size compared . . . . .	68
4.6	MSDs of individual VNBs show three modes of diffusion and on an average anomalous diffusion . . . . .	69
4.7	Volume and intensity evolution of VNBs during fusion . . . . .	70
4.8	More fusion data . . . . .	71
4.9	Channel-like vimentin polymers spatially restricted in the nucleus . . . . .	72
4.10	Dimensions of the nuclear channels . . . . .	72
4.11	Simulation of diffusion inside a nucleus visualized . . . . .	73
4.12	Plot of D vs Particle size: simulation results compared to experimental data . . . . .	74
4.13	Relative intensities of YFP in a FRAP experiment in different regions	76
4.14	Chromatin density vs. half time of FRAP . . . . .	77

4.15	Fitting FRAP half time profiles and their dependence on chromatin density . . . . .	77
4.16	The inhomogeneity of chromatin distribution . . . . .	78
4.17	Line scans in X- and Y-directions in bleach regions of FRAP experiments . . . . .	80
4.18	Prebleach images of cells with labelled H2B and NLS-YFP . . . . .	81
4.19	Results of a 2D diffusion simulation is compared to experimental data	82
4.20	3-D distribution of TopoII . . . . .	83
4.21	3-D distribution of TopoII with and without drug treatment . . . . .	84
4.22	Topolgy of TopoII distribution model . . . . .	85
4.23	Fits of TopoII model to experimental data from FRAP . . . . .	86
4.24	Model to test the effect of early replication on TopoII distribution . .	87
4.25	Simulation result of early replication on TopoII distribution . . . . .	88
5.1	Models of VNB fusion . . . . .	91
5.2	Results of different simulated obstacles to diffusion of nuclear bodies	93
6.1	Refined ICD model . . . . .	99
6.2	2-D simulated FRAP can address each subregion . . . . .	103
A.1	Algorithm used to simulate diffusion in the nucleus by the Monte Carlo method . . . . .	109

# List of Tables

2.1	Time to traverse the nucleus for typical molecules . . . . .	15
2.2	Typical sizes of nuclear structures . . . . .	18
2.3	Fluorescent protein extinction and bleaching time . . . . .	26
3.1	Laser power and wavelengths . . . . .	50
3.2	CFP and YFP excitation and emission maxima . . . . .	50
4.1	Mobile and immobile fractions from FRAP experiments . . . . .	78
4.2	Fitted residence times of TopoII . . . . .	87
6.1	Table showing the mobility of different NBs in a common range . .	100

## References

- [1] W. W. Franke, Matthias jacob schleiden and the definition of the cell nucleus, *Eur J Cell Biol* 47 (2) (1988) 145–56.
- [2] E. S. e. a. Lander, Initial sequencing and analysis of the human genome, *Nature* 409 (6822) (2001) 860–921.
- [3] J. C. e. a. Venter, The sequence of the human genome, *Science* 291 (5507) (2001) 1304–51.
- [4] B. Alberts, D. Bray, J. Lewis, M. Raff, K. Roberts, J. D. Watson, *Molecular Biology of the Cell*, 3rd Edition, New York and London: Garland Publishing, 1994.
- [5] P. J. Horn, C. L. Peterson, Molecular biology. chromatin higher order folding–wrapping up transcription, *Science* 297 (5588) (2002) 1824–7.
- [6] T. Cremer, C. Cremer, T. Schneider, H. Baumann, L. Hens, M. Kirsch-Volders, Analysis of chromosome positions in the interphase nucleus of chinese hamster cells by laser-uv-microirradiation experiments, *Hum Genet* 62 (3) (1982) 201–9, using Smart Source Parsing.
- [7] T. Cremer, C. Cremer, H. Baumann, E. K. Luedtke, K. Sperling, V. Teuber, C. Zorn, Rabl’s model of the interphase chromosome arrangement tested in chinese hamster cells by premature chromosome condensation and laser-uv-microbeam experiments, *Hum Genet* 60 (1) (1982) 46–56, using Smart Source Parsing.
- [8] P. R. Cook, A chromomeric model for nuclear and chromosome structure, *J Cell Sci* 108 (Pt 9) (1995) 2927–35.
- [9] A. Schulz, N. Mucke, J. Langowski, K. Rippe, Scanning force microscopy of escherichia coli rna polymerase.sigma54 holoenzyme complexes with dna in buffer and in air, *J Mol Biol* 283 (4) (1998) 821–36.
- [10] R. M. Zirbel, U. R. Mathieu, A. Kurz, T. Cremer, P. Lichter, Evidence for a nuclear compartment of transcription and splicing located at chromosome domain boundaries, *Chromosome Res* 1 (2) (1993) 93–106.
- [11] J. C. Politz, T. Pederson, Review: movement of mrna from transcription site to nuclear pores, *J Struct Biol* 129 (2-3) (2000) 252–7.
- [12] O. Seksek, J. Biwersi, A. S. Verkman, Translational diffusion of macromolecule-sized solutes in cytoplasm and nucleus, *J Cell Biol* 138 (1) (1997) 131–42.
- [13] T. Pederson, Dynamics and genome-centricity of interchromatin domains in the nucleus, *Nat Cell Biol* 4 (12) (2002) E287–91.

- [14] B. P. Olveczky, A. S. Verkman, Monte carlo analysis of obstructed diffusion in three dimensions: application to molecular diffusion in organelles, *Biophys J* 74 (5) (1998) 2722–30.
- [15] K. Hirschberg, C. M. Miller, J. Ellenberg, J. F. Presley, E. D. Siggia, R. D. Phair, J. Lippincott-Schwartz, Kinetic analysis of secretory protein traffic and characterization of golgi to plasma membrane transport intermediates in living cells, *J Cell Biol* 143 (6) (1998) 1485–503.
- [16] D. Uttenweiler, C. Weber, R. H. Fink, Mathematical modeling and fluorescence imaging to study the  $ca^{2+}$  turnover in skinned muscle fibers, *Biophys J* 74 (4) (1998) 1640–53.
- [17] J. Wagner, Y. X. Li, J. Pearson, J. Keizer, Simulation of the fertilization  $ca^{2+}$  wave in *xenopus laevis* eggs, *Biophys J* 75 (4) (1998) 2088–97.
- [18] A. T. Sumner, The distribution of topoisomerase ii on mammalian chromosomes, *Chromosome Res* 4 (1) (1996) 5–14.
- [19] C. E. Lyon, A. I. Lamond, The nucleolus, *Curr Biol* 10 (9) (2000) R323.
- [20] J. C. Politz, R. A. Tuft, T. Pederson, R. H. Singer, Movement of nuclear poly(a) rna throughout the interchromatin space in living cells, *Curr Biol* 9 (6) (1999) 285–91.
- [21] T. Pederson, Thinking about a nuclear matrix, *J Mol Biol* 277 (2) (1998) 147–59.
- [22] R. D. Shelby, K. M. Hahn, K. F. Sullivan, Dynamic elastic behavior of alpha-satellite dna domains visualized in situ in living human cells, *J Cell Biol* 135 (3) (1996) 545–57.
- [23] M. E. Luderus, B. van Steensel, L. Chong, O. C. Sibon, F. F. Cremers, T. de Lange, Structure, subnuclear distribution, and nuclear matrix association of the mammalian telomeric complex, *J Cell Biol* 135 (4) (1996) 867–81.
- [24] H. B. Sun, H. Yokota, Correlated positioning of homologous chromosomes in daughter fibroblast cells, *Chromosome Res* 7 (8) (1999) 603–10, using Smart Source Parsing.
- [25] H. B. Sun, J. Shen, H. Yokota, Size-dependent positioning of human chromosomes in interphase nuclei, *Biophys J* 79 (1) (2000) 184–90.
- [26] W. A. Bickmore, P. Teague, Influences of chromosome size, gene density and nuclear position on the frequency of constitutional translocations in the human population, *Chromosome Res* 10 (8) (2002) 707–15.
- [27] A. J. Varshavsky, S. A. Nedospasov, V. V. Schmatchenko, V. V. Bakayev, P. M. Chumackov, G. P. Georgiev, Compact form of sv40 viral minichromosome is



- resistant to nuclease: possible implications for chromatin structure, *Nucleic Acids Res* 4 (10) (1977) 3303–25.
- [28] N. Sadoni, S. Langer, C. Fauth, G. Bernardi, T. Cremer, B. M. Turner, D. Zink, Nuclear organization of mammalian genomes. polar chromosome territories build up functionally distinct higher order compartments, *J Cell Biol* 146 (6) (1999) 1211–26.
- [29] D. Zink, H. Bornfleth, A. Visser, C. Cremer, T. Cremer, Organization of early and late replicating dna in human chromosome territories, *Exp Cell Res* 247 (1) (1999) 176–88.
- [30] T. Cremer, A. Kurz, R. Zirbel, S. Dietzel, B. Rinke, E. Schroeck, M. R. Speicher, U. Mathieu, A. Jauch, P. Emmerich, H. Scherthan, T. Ried, C. Cremer, P. Lichter, Role of chromosome territories in the functional compartmentalization of the cell nucleus, *Cold Spring Harbour Symposia on Quantitative Biology* LVIII (1993) 777–792.
- [31] T. Cremer, C. Cremer, Chromosome territories, nuclear architecture and gene regulation in mammalian cells, *Nat Rev Genet* 2 (4) (2001) 292–301.
- [32] A. E. Visser, R. Eils, A. Jauch, G. Little, P. J. Bakker, T. Cremer, J. A. Aten, Spatial distributions of early and late replicating chromatin in interphase chromosome territories, *Exp Cell Res* 243 (2) (1998) 398–407.
- [33] A. E. Visser, J. A. Aten, Chromosomes as well as chromosomal subdomains constitute distinct units in interphase nuclei, *J Cell Sci* 112 (Pt 19) (1999) 3353–60.
- [34] C. Zorn, C. Cremer, T. Cremer, J. Zimmer, Unscheduled dna synthesis after partial uv irradiation of the cell nucleus. distribution in interphase and metaphase, *Exp Cell Res* 124 (1) (1979) 111–9.
- [35] H. Herrmann, P. Lichter, New ways to look at the interchromosomal-domain compartment, *Protoplasma* 209 (Issue 3-4) (1999) 157–165.
- [36] N. L. Mahy, P. E. Perry, W. A. Bickmore, Gene density and transcription influence the localization of chromatin outside of chromosome territories detectable by fish, *J Cell Biol* 159 (5) (2002) 753–63.
- [37] G. Zimowska, J. P. Aris, M. R. Paddy, A drosophila tpr protein homolog is localized both in the extrachromosomal channel network and to nuclear pore complexes, *J Cell Sci* 110 (Pt 8) (1997) 927–44.
- [38] J. M. Bridger, H. Herrmann, C. Munkel, P. Lichter, Identification of an interchromosomal compartment by polymerization of nuclear-targeted vimentin, *J Cell Sci* 111 (Pt 9) (1998) 1241–53.

- 
- [39] M. Wasser, W. Chia, The east protein of drosophila controls an expandable nuclear endoskeleton, *Nat Cell Biol* 2 (5) (2000) 268–75.
- [40] H. C. Berg, *Random Walks in Biology*, Princeton Univ Press, Princeton, 1993.
- [41] J. R. Abney, B. Cutler, M. L. Fillbach, D. Axelrod, B. A. Scalettar, Chromatin dynamics in interphase nuclei and its implications for nuclear structure, *J Cell Biol* 137 (7) (1997) 1459–68.
- [42] W. F. Marshall, A. Straight, J. F. Marko, J. Swedlow, A. Dernburg, A. Belmont, A. W. Murray, D. A. Agard, J. W. Sedat, Interphase chromosomes undergo constrained diffusional motion in living cells, *Curr Biol* 7 (12) (1997) 930–9.
- [43] D. L. Spector, Macromolecular domains within the cell nucleus, *Annu Rev Cell Biol* 9 (1993) 265–315, using Smart Source Parsing.
- [44] D. L. Spector, Higher order nuclear organization: three-dimensional distribution of small nuclear ribonucleoprotein particles, *Proc Natl Acad Sci U S A* 87 (1) (1990) 147–51.
- [45] R. D. Everett, W. C. Earnshaw, A. F. Pluta, T. Sternsdorf, A. M. Ainsztein, M. Carmena, S. Ruchaud, W. L. Hsu, A. Orr, A dynamic connection between centromeres and nd10 proteins, *J Cell Sci* 112 (Pt 20) (1999) 3443–54.
- [46] R. D. Phair, T. Misteli, High mobility of proteins in the mammalian cell nucleus, *Nature* 404 (6778) (2000) 604–9.
- [47] W. C. Earnshaw, B. Halligan, C. A. Cooke, M. M. Heck, L. F. Liu, Topoisomerase ii is a structural component of mitotic chromosome scaffolds, *J Cell Biol* 100 (5) (1985) 1706–15.
- [48] W. C. Earnshaw, M. M. Heck, Localization of topoisomerase ii in mitotic chromosomes, *J Cell Biol* 100 (5) (1985) 1716–25.
- [49] J. R. Swedlow, J. W. Sedat, D. A. Agard, Multiple chromosomal populations of topoisomerase ii detected in vivo by time-lapse, three-dimensional wide-field microscopy, *Cell* 73 (1) (1993) 97–108.
- [50] A. Monneron, W. Bernhard, Fine structural organization of the interphase nucleus in some mammalian cells, *J Ultrastruct Res* 27 (3) (1969) 266–88.
- [51] D. Zink, T. Cremer, R. Saffrich, R. Fischer, M. F. Trendelenburg, W. Ansorge, E. H. Stelzer, Structure and dynamics of human interphase chromosome territories in vivo, *Hum Genet* 102 (2) (1998) 241–51.
- [52] S. Fakan, E. Puvion, The ultrastructural visualization of nucleolar and extranucleolar rna synthesis and distribution, *Int Rev Cytol* 65 (1980) 255–99, using Smart Source Parsing.
-

- [53] J. G. Gall, Cajal bodies: the first 100 years, *Annu Rev Cell Dev Biol* 16 (2000) 273–300, using Smart Source Parsing.
- [54] J. S. Clegg, Properties and metabolism of the aqueous cytoplasm and its boundaries, *Am J Physiol* 246 (2 Pt 2) (1984) R133–51.
- [55] A. M. Mastro, A. D. Keith, Diffusion in the aqueous compartment, *J Cell Biol* 99 (1 Pt 2) (1984) 180s–187s.
- [56] K. R. Porter, The cytomatrix: a short history of its study, *J Cell Biol* 99 (1 Pt 2) (1984) 3s–12s.
- [57] K. Luby-Phelps, Physical properties of cytoplasm, *Curr Opin Cell Biol* 6 (1) (1994) 3–9.
- [58] I. Lang, M. Scholz, R. Peters, Molecular mobility and nucleocytoplasmic flux in hepatoma cells, *J Cell Biol* 102 (4) (1986) 1183–90.
- [59] G. L. Lukacs, P. Haggie, O. Seksek, D. Lechardeur, N. Freedman, A. S. Verkman, Size-dependent dna mobility in cytoplasm and nucleus, *J Biol Chem* 275 (3) (2000) 1625–9.
- [60] M. Reichenzeller, A. Burzlaff, P. Lichter, H. Herrmann, In vivo observation of a nuclear channel-like system: evidence for a distinct interchromosomal domain compartment in interphase cells, *J Struct Biol* 129 (2-3) (2000) 175–85.
- [61] S. M. Gasser, T. Laroche, J. Falquet, E. Boy de la Tour, U. K. Laemmli, Metaphase chromosome structure. involvement of topoisomerase ii, *J Mol Biol* 188 (4) (1986) 613–29.
- [62] M. Berrios, N. Osheroff, P. A. Fisher, In situ localization of dna topoisomerase ii, a major polypeptide component of the drosophila nuclear matrix fraction, *Proc Natl Acad Sci U S A* 82 (12) (1985) 4142–6.
- [63] T. Hirano, T. J. Mitchison, Topoisomerase ii does not play a scaffolding role in the organization of mitotic chromosomes assembled in xenopus egg extracts, *J Cell Biol* 120 (3) (1993) 601–12.
- [64] C. A. Austin, K. L. Marsh, Eukaryotic dna topoisomerase ii beta, *Bioessays* 20 (3) (1998) 215–26.
- [65] Y. Hiraoka, J. W. Sedat, D. A. Agard, The use of a charge-coupled device for quantitative optical microscopy of biological structures, *Science* 238 (4823) (1987) 36–41.
- [66] J. R. Swedlow, K. Hu, P. D. Andrews, D. S. Roos, J. M. Murray, Measuring tubulin content in toxoplasma gondii: a comparison of laser- scanning confocal and wide-field fluorescence microscopy, *Proc Natl Acad Sci U S A* 99 (4) (2002) 2014–9.

- 
- [67] C. Xu, W. Zipfel, J. B. Shear, R. M. Williams, W. W. Webb, Multiphoton fluorescence excitation: new spectral windows for biological nonlinear microscopy, *Proc Natl Acad Sci U S A* 93 (20) (1996) 10763–8.
- [68] T. A. Klar, S. Jakobs, M. Dyba, A. Egner, S. W. Hell, Fluorescence microscopy with diffraction resolution barrier broken by stimulated emission, *Proc Natl Acad Sci U S A* 97 (15) (2000) 8206–10.
- [69] M. Nagorni, S. W. Hell, 4pi-confocal microscopy provides three-dimensional images of the microtubule network with 100- to 150-nm resolution, *J Struct Biol* 123 (3) (1998) 236–47.
- [70] B. Bailey, D. L. Farkas, D. L. Taylor, F. Lanni, Enhancement of axial resolution in fluorescence microscopy by standing-wave excitation, *Nature* 366 (6450) (1993) 44–8.
- [71] M. G. Gustafsson, D. A. Agard, J. W. Sedat, I5m: 3d widefield light microscopy with better than 100 nm axial resolution, *J Microsc* 195 (Pt 1) (1999) 10–6.
- [72] R. Y. Tsien, A. Waggoner, Fluorophores for confocal microscopy- photophysics and photochemistry, in: J. B. Pawley (Ed.), *Handbook of Biological Confocal Microscopy*, 2nd Edition, Plenum Press, New York, 1995, pp. 267–279.
- [73] M. Chalfie, Y. Tu, G. Euskirchen, W. W. Ward, D. C. Prasher, Green fluorescent protein as a marker for gene expression, *Science* 263 (5148) (1994) 802–5.
- [74] M. Minsky, Memoir on inventing the confocal scanning microscope, *Scanning* 10 (1988) 128–138.
- [75] J. B. Pawley, *Handbook of Biological Confocal Microscopy*, 2nd Edition, Plenum Press, New York, 1995.
- [76] A. B. Cubitt, R. Heim, S. R. Adams, A. E. Boyd, L. A. Gross, R. Y. Tsien, Understanding, improving and using green fluorescent proteins, *Trends Biochem Sci* 20 (11) (1995) 448–55.
- [77] D. C. Prasher, V. K. Eckenrode, W. W. Ward, F. G. Prendergast, M. J. Cormier, Primary structure of the *aequorea victoria* green-fluorescent protein, *Gene* 111 (2) (1992) 229–33.
- [78] D. C. Prasher, Using gfp to see the light, *Trends Genet* 11 (8) (1995) 320–3.
- [79] M. Ormo, A. B. Cubitt, K. Kallio, L. A. Gross, R. Y. Tsien, S. J. Remington, Crystal structure of the *aequorea victoria* green fluorescent protein, *Science* 273 (5280) (1996) 1392–5.
- [80] T. T. Yang, L. Cheng, S. R. Kain, Optimized codon usage and chromophore mutations provide enhanced sensitivity with the green fluorescent protein, *Nucleic Acids Res* 24 (22) (1996) 4592–3.
-

- [81] M. V. Matz, A. F. Fradkov, Y. A. Labas, A. P. Savitsky, A. G. Zaraisky, M. L. Markelov, S. A. Lukyanov, Fluorescent proteins from nonbioluminescent anthozoa species, *Nat Biotechnol* 17 (10) (1999) 969–73.
- [82] G. Patterson, R. N. Day, D. Piston, Fluorescent protein spectra, *J Cell Sci* 114 (Pt 5) (2001) 837–8.
- [83] U. Kubitscheck, O. Kuckmann, T. Kues, R. Peters, Imaging and tracking of single gfp molecules in solution, *Biophys J* 78 (4) (2000) 2170–9.
- [84] J. Ellenberg, J. Lippincott-Schwartz, J. F. Presley, Two-color green fluorescent protein time-lapse imaging, *Biotechniques* 25 (5) (1998) 838–42, 844–6.
- [85] J. White, E. Stelzer, Photobleaching gfp reveals protein dynamics inside live cells, *Trends Cell Biol* 9 (2) (1999) 61–5.
- [86] K. F. Sullivan, R. D. Shelby, Using time-lapse confocal microscopy for analysis of centromere dynamics in human cells, *Methods Cell Biol* 58 (1999) 183–202, using Smart Source Parsing.
- [87] J. Lakowicz, *Principles of Fluorescence Spectroscopy*, Kluwer Academic/Plenum Publishers, New York, 1999.
- [88] R. Pepperkok, A. Squire, S. Geley, P. I. Bastiaens, Simultaneous detection of multiple green fluorescent proteins in live cells by fluorescence lifetime imaging microscopy, *Curr Biol* 9 (5) (1999) 269–72.
- [89] M. Kneen, J. Farinas, Y. Li, A. S. Verkman, Green fluorescent protein as a noninvasive intracellular ph indicator, *Biophys J* 74 (3) (1998) 1591–9.
- [90] L. M. Loew, Voltage-sensitive dyes: measurement of membrane potentials induced by dc and ac electric fields, *Bioelectromagnetics Suppl* (1) (1992) 179–89.
- [91] E. Emmanouilidou, A. G. Teschemacher, A. E. Pouli, L. I. Nicholls, E. P. Seward, G. A. Rutter, Imaging  $ca^{2+}$  concentration changes at the secretory vesicle surface with a recombinant targeted cameleon, *Curr Biol* 9 (16) (1999) 915–8.
- [92] M. Abercrombie, Estimation of nuclear population from microtome sections, *The Anatomical Record* 94 (1946) 239–247.
- [93] R. W. Williams, P. Rakic, Three-dimensional counting: an accurate and direct method to estimate numbers of cells in sectioned material, *J Comp Neurol* 278 (3) (1988) 344–52.
- [94] R. D. Allen, N. S. Allen, Video-enhanced microscopy with a computer frame memory, *J Microsc* 129 (Pt 1) (1983) 3–17.
- [95] S. Inoue, Video image processing greatly enhances contrast, quality, and speed in polarization-based microscopy, *J Cell Biol* 89 (2) (1981) 346–56.

- [96] S. Inoue, Progress in video microscopy, *Cell Motil Cytoskeleton* 10 (1-2) (1988) 13–7.
- [97] H. C. Berg, D. A. Brown, Chemotaxis in *escherichia coli* analysed by three-dimensional tracking, *Nature* 239 (5374) (1972) 500–4.
- [98] G. S. Berns, M. W. Berns, Computer-based tracking of living cells, *Exp Cell Res* 142 (1) (1982) 103–9.
- [99] C. Athale, M. Gebhard, R. Eils, Examining Spatio-Temporal Dynamics in Cell Nuclei by Image Processing Methods, Vol. I of Science, Technology and Education of Microscopy: An Overview, *FORMATEX Microscopy Book Series* (in press), 2002.
- [100] R. Eils, C. Athale, Computational imaging in cell biology, *J Cell Biol* 161 (3).
- [101] W. Tvarusko, M. Bentele, T. Misteli, R. Rudolf, C. Kaether, D. L. Spector, H. H. Gerdes, R. Eils, Time-resolved analysis and visualization of dynamic processes in living cells, *Proc Natl Acad Sci U S A* 96 (14) (1999) 7950–5.
- [102] H. Qian, M. P. Sheetz, E. L. Elson, Single particle tracking. analysis of diffusion and flow in two- dimensional systems, *Biophys J* 60 (4) (1991) 910–21.
- [103] A. Mitiche, P. Bouthemy, Computation and analysis of image motion: a synopsis of current problems and methods, *Int. J. Comp. Vis.* 19 (1) (1996) 29–55.
- [104] B. Jaehne, *Digital Image Processing*, Springer, 2002.
- [105] S. Lavallee, R. Szeliski, Recovering the position and orientation of free-form objects from image contours using 3d distance maps, *T-PAMI* 17 (1995) 195–201.
- [106] D. Terzopoulos, J. Platt, K. Fleischer, Heating and melting deformable models, *The Journal of Visualization and Computer Animation* 2 (2) (1991) 68–73.
- [107] J. B. Maintz, M. A. Viergever, A survey of medical image registration, *Med Image Anal* 2 (1) (1998) 1–36.
- [108] H. Bornfleth, P. Edelmann, D. Zink, T. Cremer, C. Cremer, Quantitative motion analysis of subchromosomal foci in living cells using four-dimensional microscopy, *Biophys J* 77 (5) (1999) 2871–86.
- [109] R. Szeliski, Video mosaics for virtual environments, *IEEE Computer Graphics and Applications* 16 (2) (1996) 22–30.
- [110] K. Arun, T. Huang, S. Blostein, Least square fitting of two 3d point sets, *Transactions of Pattern Analysis and Machine Intelligence* 9 (5) (1987) 698–700.
- [111] K. Rohr, On 3d differential operators for detecting point landmarks, *Image and Vision Computing* 15 (3) (1997) 219–233.



- [112] N. White, Visualization systems for multidimensional clsm images, in: J. B. Pawley (Ed.), *Handbook of Biological Confocal Microscopy*, 2nd Edition, Plenum Press, New York, 1995, pp. 211–254.
- [113] K. Konig, P. T. So, W. W. Mantulin, B. J. Tromberg, E. Gratton, Two-photon excited lifetime imaging of autofluorescence in cells during uva and nir photostress, *J Microsc* 183 (Pt 3) (1996) 197–204.
- [114] C. Thomas, P. DeVries, J. Hardin, J. White, Four-dimensional imaging: computer visualization of 3d movements in living specimens, *Science* 273 (5275) (1996) 603–7.
- [115] H. Chen, J. R. Swedlow, M. Grote, J. W. Sedat, D. A. Agard, *Handbook of biological confocal microscopy*, in: J. B. Pawley (Ed.), *Handbook of Biological Confocal Microscopy*, 2nd Edition, Plenum Press, 1995, pp. 197–209.
- [116] S. J. Wright, V. E. Centonze, S. A. Stricker, P. J. DeVries, S. W. Paddock, G. Schatten, Introduction to confocal microscopy and three-dimensional reconstruction, *Methods Cell Biol* 38 (1993) 1–45, using Smart Source Parsing.
- [117] H. E. Cline, W. E. Lorensen, S. Ludke, C. R. Crawford, B. C. Teeter, Two algorithms for the three-dimensional reconstruction of tomograms, *Med Phys* 15 (3) (1988) 320–7.
- [118] R. Eils, S. Dietzel, E. Bertin, E. Schrock, M. R. Speicher, T. Ried, M. Robert-Nicoud, C. Cremer, T. Cremer, Three-dimensional reconstruction of painted human interphase chromosomes: active and inactive x chromosome territories have similar volumes but differ in shape and surface structure, *J Cell Biol* 135 (6 Pt 1) (1996) 1427–40.
- [119] M. Gebhard, R. Eils, J. Mattes, Segmentation of 3d objects using nurbs surfaces for quantification of surface and volume dynamics, in: *Proceedings of the International Conference on Diagnostic Imaging and Analysis (ICDIA 2002)*, Shanghai, China, 2002, pp. 125–130.
- [120] D. Gerlich, J. Beaudouin, M. Gebhard, J. Ellenberg, R. Eils, Four-dimensional imaging and quantitative reconstruction to analyse complex spatiotemporal processes in live cells, *Nat Cell Biol* 3 (9) (2001) 852–5.
- [121] D. Axelrod, D. E. Koppel, J. Schlessinger, E. Elson, W. W. Webb, Mobility measurement by analysis of fluorescence photobleaching recovery kinetics, *Biophys J* 16 (9) (1976) 1055–69.
- [122] M. Edidin, Y. Zagayansky, T. J. Lardner, Measurement of membrane protein lateral diffusion in single cells, *Science* 191 (4226) (1976) 466–8.

- [123] R. Peters, J. Peters, K. H. Tews, W. Bahr, A microfluorimetric study of translational diffusion in erythrocyte membranes, *Biochim Biophys Acta* 367 (3) (1974) 282–94.
- [124] B. Barisas, M. Leuther, Fluorescence photobleaching recovery measurement of protein absolute diffusion constants, *Biophysical Chemistry* 10 (2) (1977) 221–229.
- [125] J. Yguerabide, J. A. Schmidt, E. E. Yguerabide, Lateral mobility in membranes as detected by fluorescence recovery after photobleaching, *Biophys J* 40 (1) (1982) 69–75.
- [126] E. J. van Zoelen, L. G. Tertoolen, S. W. de Laat, Simple computer method for evaluation of lateral diffusion coefficients from fluorescence photobleaching recovery kinetics, *Biophys J* 42 (1) (1983) 103–8.
- [127] D. M. Soumpasis, Theoretical analysis of fluorescence photobleaching recovery experiments, *Biophys J* 41 (1) (1983) 95–7.
- [128] U. Kubitscheck, P. Wedekind, R. Peters, Lateral diffusion measurement at high spatial resolution by scanning microphotolysis in a confocal microscope, *Biophys J* 67 (3) (1994) 948–56.
- [129] R. Swaminathan, C. P. Hoang, A. S. Verkman, Photobleaching recovery and anisotropy decay of green fluorescent protein gfp-s65t in solution and cells: cytoplasmic viscosity probed by green fluorescent protein translational and rotational diffusion, *Biophys J* 72 (4) (1997) 1900–7.
- [130] A. Partikian, B. Olveczky, R. Swaminathan, Y. Li, A. S. Verkman, Rapid diffusion of green fluorescent protein in the mitochondrial matrix, *J Cell Biol* 140 (4) (1998) 821–9.
- [131] N. Gershenfeld, *The Nature of Mathematical Modeling*, Cambridge University Press, Cambridge, 1999.
- [132] J. Crank, *The Mathematics of Diffusion*, 2nd Edition, Oxford University Press, Oxford, 1975.
- [133] M. J. Saxton, Lateral diffusion in a mixture of mobile and immobile particles. a monte carlo study, *Biophys J* 58 (5) (1990) 1303–6.
- [134] M. J. Saxton, Lateral diffusion in an archipelago. dependence on tracer size, *Biophys J* 64 (4) (1993) 1053–62.
- [135] M. J. Saxton, Lateral diffusion in an archipelago. single-particle diffusion, *Biophys J* 64 (6) (1993) 1766–80.
- [136] M. J. Saxton, Anomalous diffusion due to obstacles: a monte carlo study, *Biophys J* 66 (2 Pt 1) (1994) 394–401.



- [137] M. J. Saxton, Single-particle tracking: models of directed transport, *Biophys J* 67 (5) (1994) 2110–9.
- [138] M. J. Saxton, Anomalous diffusion due to binding: a monte carlo study, *Biophys J* 70 (3) (1996) 1250–62.
- [139] T. J. Feder, I. Brust-Mascher, J. P. Slattery, B. Baird, W. W. Webb, Constrained diffusion or immobile fraction on cell surfaces: a new interpretation, *Biophys J* 70 (6) (1996) 2767–73.
- [140] G. J. Schutz, H. Schindler, T. Schmidt, Single-molecule microscopy on model membranes reveals anomalous diffusion, *Biophys J* 73 (2) (1997) 1073–80.
- [141] G. W. Gordon, B. Chazotte, X. F. Wang, B. Herman, Analysis of simulated and experimental fluorescence recovery after photobleaching. data for two diffusing components, *Biophys J* 68 (3) (1995) 766–78.
- [142] J. F. Nagle, Long tail kinetics in biophysics?, *Biophys J* 63 (2) (1992) 366–70.
- [143] F. P. Coelho, W. L. Vaz, E. Melo, Phase topology and percolation in two-component lipid bilayers: a monte carlo approach, *Biophys J* 72 (4) (1997) 1501–11.
- [144] N. Periasamy, A. S. Verkman, Analysis of fluorophore diffusion by continuous distributions of diffusion coefficients: application to photobleaching measurements of multicomponent and anomalous diffusion, *Biophys J* 75 (1) (1998) 557–67.
- [145] P. Atkins, J. de Paula, *Physical Chemistry*, 7th Edition, Oxford Univ. Press, Oxford, 2001.
- [146] J. A. Jacquez, *Compartmental Analysis in Biology and Medicine*, Elsevier, Amsterdam, 1972.
- [147] L. Segel, *Modeling Dynamic Phenomena in Molecular and Cellular Biology*, Cambridge University Press, Cambridge, 1984.
- [148] J. Bartol, T. M., B. R. Land, E. E. Salpeter, M. M. Salpeter, Monte carlo simulation of miniature endplate current generation in the vertebrate neuromuscular junction, *Biophys J* 59 (6) (1991) 1290–307.
- [149] M. J. Saxton, Lateral diffusion and aggregation. a monte carlo study, *Biophys J* 61 (1) (1992) 119–28.
- [150] L. Von Bertalanffy, *General System Theory*, George Braziller Inc., New York, 1968.
- [151] H. Kitano, Computational systems biology, *Nature* 420 (6912) (2002) 206–10.
- [152] K. K. Hedberg, L. B. Chen, Absence of intermediate filaments in a human adrenal cortex carcinoma- derived cell line, *Exp Cell Res* 163 (2) (1986) 509–17.

- [153] J. Ellenberg, J. Lippincott-Schwartz, Dynamics and mobility of nuclear envelope proteins in interphase and mitotic cells revealed by green fluorescent protein chimeras, *Methods* 19 (3) (1999) 362–72.
- [154] M. Reichenzeller, Strukturelle und dynamische analyse des interchromosomalen domänen-kompartiments, Biological, University of Heidelberg (2002).
- [155] A. Guiochon-Mantel, P. Lescop, S. Christin-Maitre, H. Loosfelt, M. Perrot-Appanat, E. Milgrom, Nucleocytoplasmic shuttling of the progesterone receptor, *Embo J* 10 (12) (1991) 3851–9.
- [156] W. D. Richardson, A. D. Mills, S. M. Dilworth, R. A. Laskey, C. Dingwall, Nuclear protein migration involves two steps: rapid binding at the nuclear envelope followed by slower translocation through nuclear pores, *Cell* 52 (5) (1988) 655–64.
- [157] E. D. Schwoebel, T. H. Ho, M. S. Moore, The mechanism of inhibition of ran-dependent nuclear transport by cellular atp depletion, *J Cell Biol* 157 (6) (2002) 963–74.
- [158] D. L. Stenoien, M. Mielke, M. A. Mancini, Intranuclear ataxin1 inclusions contain both fast- and slow-exchanging components, *Nat Cell Biol* 4 (10) (2002) 806–10.
- [159] M. Black, G. Sapiro, D. Marimont, D. Heeger, Robust anisotropic diffusion, *IEEE Trans. on Image Processing* 7 (3) (1998) 421–432.
- [160] L. Kubinova, J. Janacek, F. Guilak, Z. Opatrny, Comparison of several digital and stereological methods for estimating surface area and volume of cells studied by confocal microscopy, *Cytometry* 36 (2) (1999) 85–95.
- [161] D. Ermak, J. McCammon, Brownian dynamics with hydrodynamic interactions., *J. Chem. Phys.* 69 (1978) 1352–1360.
- [162] G. W. Snedecor, W. G. Cochran, *Statistical Methods*, eighth edition Edition, Iowa State University Press, 1989.
- [163] S. P. Alexander, C. L. Rieder, Chromosome motion during attachment to the vertebrate spindle: initial saltatory-like behavior of chromosomes and quantitative analysis of force production by nascent kinetochore fibers, *J Cell Biol* 113 (4) (1991) 805–15.
- [164] W. F. Marshall, J. F. Marko, D. A. Agard, J. W. Sedat, Chromosome elasticity and mitotic polar ejection force measured in living drosophila embryos by four-dimensional microscopy-based motion analysis, *Curr Biol* 11 (8) (2001) 569–78.

- 
- [165] M. Platani, I. Goldberg, A. I. Lamond, J. R. Swedlow, Cajal body dynamics and association with chromatin are atp-dependent, *Nat Cell Biol* 4 (7) (2002) 502–8.
- [166] M. O. Christensen, M. K. Larsen, H. U. Barthelmes, R. Hock, C. L. Andersen, E. Kjeldsen, B. R. Knudsen, O. Westergaard, F. Boege, C. Mielke, Dynamics of human dna topoisomerases  $\alpha$  and  $\beta$  in living cells, *J Cell Biol* 157 (1) (2002) 31–44.
- [167] M. Carmo-Fonseca, L. Mendes-Soares, I. Campos, To be or not to be in the nucleolus, *Nat Cell Biol* 2 (6) (2000) E107–12.
- [168] M. Platani, I. Goldberg, J. R. Swedlow, A. I. Lamond, In vivo analysis of cajal body movement, separation, and joining in live human cells, *J Cell Biol* 151 (7) (2000) 1561–74.
- [169] M. Muratani, D. Gerlich, S. M. Janicki, M. Gebhard, R. Eils, D. L. Spector, Metabolic-energy-dependent movement of pml bodies within the mammalian cell nucleus, *Nat Cell Biol* 4 (2) (2002) 106–10.
- [170] K. V. Prasanth, P. A. Sacco-Bubulya, S. G. Prasanth, D. L. Spector, Sequential entry of components of gene expression machinery into daughter nuclei, *Mol Biol Cell* 14 (3) (2003) 1043–57.
- [171] N. Busch, T. Kim, V. Bloomfield, Tracer diffusion of proteins in dna solutions. 2. green fluorescent protein in crowded dna solutions, *Macromolecules* 33 (16) (2000) 5932–5937.
- [172] M. Dundr, T. Misteli, Functional architecture in the cell nucleus, *Biochem J* 356 (Pt 2) (2001) 297–310.
- [173] J. Roix, T. Misteli, Genomes, proteomes, and dynamic networks in the cell nucleus, *Histochem Cell Biol* 118 (2) (2002) 105–16.
- [174] D. Volz, M. Eigel, C. Athale, P. Bastian, H. Herrmann, R. Eils, Spatial modeling and simulation of diffusion in nuclei of living cells, *Biocomplexity* submitted.
- [175] E. D. Siggia, J. Lippincott-Schwartz, S. Bekiranov, Diffusion in inhomogeneous media: theory and simulations applied to whole cell photobleach recovery, *Biophys J* 79 (4) (2000) 1761–70.
- [176] M. Dundr, U. Hoffmann-Rohrer, Q. Hu, I. Grummt, L. I. Rothblum, R. D. Phair, T. Misteli, A kinetic framework for a mammalian rna polymerase in vivo, *Science* 298 (5598) (2002) 1623–6.
- [177] D. L. Spector, Nuclear domains, *J Cell Sci* 114 (Pt 16) (2001) 2891–3.
-

- 
- [178] J. S. Andersen, C. E. Lyon, A. H. Fox, A. K. Leung, Y. W. Lam, H. Steen, M. Mann, A. I. Lamond, Directed proteomic analysis of the human nucleolus, *Curr Biol* 12 (1) (2002) 1–11.
- [179] A. H. Fox, Y. W. Lam, A. K. Leung, C. E. Lyon, J. Andersen, M. Mann, A. I. Lamond, Paraspeckles: a novel nuclear domain, *Curr Biol* 12 (1) (2002) 13–25.
- [180] R. Eils, D. Gerlich, W. Tvarusko, D. L. Spector, T. Misteli, Quantitative imaging of pre-mrna splicing factors in living cells, *Mol Biol Cell* 11 (2) (2000) 413–8.
- [181] C. Athale, M. Reichenzeller, P. Lichter, H. Herrmann, R. Eils, Principles of mobility of nuclear bodies in the interchromosomal domain revealed by nuclear targeted vimentin, *Exp. Cell Res.* submitted.
- [182] T. S. Deisboeck, M. E. Berens, A. R. Kansal, S. Torquato, A. O. Stemmer-Rachamimov, E. A. Chiocca, Pattern of self-organization in tumour systems: complex growth dynamics in a novel brain tumour spheroid model, *Cell Prolif* 34 (2) (2001) 115–34.
- [183] A. Calapez, H. M. Pereira, A. Calado, J. Braga, J. Rino, C. Carvalho, J. P. Tavanetz, E. Wahle, A. C. Rosa, M. Carmo-Fonseca, The intranuclear mobility of messenger rna binding proteins is atp dependent and temperature sensitive, *J Cell Biol* 159 (5) (2002) 795–805.
- [184] G. Nowak, L. Pestic-Dragovich, P. Hozak, A. Philimonenko, C. Simerly, G. Schatten, P. de Lanerolle, Evidence for the presence of myosin i in the nucleus, *J Biol Chem* 272 (27) (1997) 17176–81.
- [185] T. Pederson, Protein mobility within the nucleus—what are the right moves?, *Cell* 104 (5) (2001) 635–8.
- [186] P. Heun, T. Laroche, K. Shimada, P. Furrer, S. M. Gasser, Chromosome dynamics in the yeast interphase nucleus, *Science* 294 (5549) (2001) 2181–6.
- [187] J. R. Chubb, S. Boyle, P. Perry, W. A. Bickmore, Chromatin motion is constrained by association with nuclear compartments in human cells, *Curr Biol* 12 (6) (2002) 439–45.
- [188] J. G. McNally, W. G. Muller, D. Walker, R. Wolford, G. L. Hager, The glucocorticoid receptor: rapid exchange with regulatory sites in living cells, *Science* 287 (5456) (2000) 1262–5.
- [189] T. Misteli, The concept of self-organization in cellular architecture, *J Cell Biol* 155 (2) (2001) 181–5.
- [190] M. A. Medina, P. Schuille, Fluorescence correlation spectroscopy for the detection and study of single molecules in biology, *Bioessays* 24 (8) (2002) 758–64.
-

- 
- [191] T. P. O'Brien, C. J. Bult, C. Cremer, M. Grunze, B. B. Knowles, J. Langowski, J. McNally, T. Pederson, J. C. Politz, A. Pombo, G. Schmahl, J. P. Spatz, R. Van Driel, Genome function and nuclear architecture: From gene expression to nanoscience, *Genome Res* 12 (2003) 12, using Smart Source Parsing May.
- [192] M. V. Boland, R. F. Murphy, A neural network classifier capable of recognizing the patterns of all major subcellular structures in fluorescence microscope images of hela cells, *Bioinformatics* 17 (12) (2001) 1213–23.
- [193] P. D. Andrews, I. S. Harper, J. R. Swedlow, To 5d and beyond: quantitative fluorescence microscopy in the postgenomic era, *Traffic* 3 (1) (2002) 29–36.
- [194] J. R. Swedlow, I. Goldberg, E. Brauner, P. K. Sorger, Informatics and quantitative analysis in biological imaging, *Science* 300 (5616) (2003) 100–2.
- [195] I. Swameye, T. G. Muller, J. Timmer, O. Sandra, U. Klingmuller, Identification of nucleocytoplasmic cycling as a remote sensor in cellular signaling by databased modeling, *Proc Natl Acad Sci U S A* 100 (3) (2003) 1028–33.
- [196] O. Ebenhoh, R. Heinrich, Stoichiometric design of metabolic networks: multifunctionality, clusters, optimization, weak and strong robustness, *Bull Math Biol* 65 (2) (2003) 323–57.
- [197] E. Klipp, R. Heinrich, H. G. Holzhutter, Prediction of temporal gene expression. metabolic optimization by re- distribution of enzyme activities, *Eur J Biochem* 269 (22) (2002) 5406–13.
- [198] C. Athale, M. Christensen, R. Eils, F. Boege, C. Mielke, Predicting sub nuclear distribution dynamics of topoisomerase ii beta by kinetic modeling (2003).
- [199] J. M. Desterro, L. P. Keegan, M. Lafarga, M. T. Berciano, M. O'Connell, M. Carmo-Fonseca, Dynamic association of rna-editing enzymes with the nucleolus, *J Cell Sci* 116 (Pt 9) (2003) 1805–1818.
- [200] F. Nedelec, Computer simulations reveal motor properties generating stable antiparallel microtubule interactions, *J Cell Biol* 158 (6) (2002) 1005–15.
- [201] F. Nedelec, T. Surrey, E. Karsenti, Self-organisation and forces in the microtubule cytoskeleton, *Curr Opin Cell Biol* 15 (1) (2003) 118–24.
- [202] F. J. Nedelec, T. Surrey, A. C. Maggs, S. Leibler, Self-organization of microtubules and motors, *Nature* 389 (6648) (1997) 305–8.
- [203] J. Schaff, C. C. Fink, B. Slepchenko, J. H. Carson, L. M. Loew, A general computational framework for modeling cellular structure and function, *Biophys J* 73 (3) (1997) 1135–46.
- [204] C. Athale, Cell-simulations portal, *Genome Biology* 3 (1) (2001) reports2002.
-

- [205] C. Athale, Monte carlo cell simulations, *Genome Biology* 3 (1) (2001) reports2001.
- [206] M. e. Hucka, The systems biology markup language (sbml): a medium for representation and exchange of biochemical network models, *Bioinformatics* 19 (4) (2003) 524–31.
- [207] M. Matsumoto, T. Nishimura, Mersenne twister: A 623-dimensionally equidistributed uniform pseudorandom number generator, *ACM Trans. on Modeling and Computer Simulation* 8 (1) (1998) 3–30.
- [208] C. Athale, Software for cell simulation, *Genome Biology* 3 (3) (2002) reports2011.